Title

Elucidating the photonic and electronic interactions of cesium lead halide perovskite nanocrystals for advancing photonic devices

ISBN

9798293825844

Author

Parsons, Lindsey Ellen

Publication Date

2025-09-09

Peer reviewed|Thesis/dissertation

UNIVERSITY OF CALIFORNIA

Los Angeles

Elucidating the photonic and electronic interactions of cesium lead halide perovskite nanocrystals for advancing photonic devices

A dissertation submitted in partial satisfaction of the requirements for the degree Doctor of Philosophy in Chemical Engineering

by

Lindsey Ellen Parsons

2025

ABSTRACT OF THE DISSERTATION

Elucidating the photonic and electronic interactions

of cesium lead halide perovskite nanocrystals

for advancing photonic devices

by

Lindsey Ellen Parsons

Doctor of Philosophy in Chemical Engineering

University of California, Los Angeles, 2025

Professor Carissa Nicole Eisler, Chair

Our global energy demands are ever-growing due to technological innovations such as the implementation of artificial intelligence in our everyday computing or the surge in quantum information technologies. Likewise, the realization of advanced, high-efficiency energy sources and energy utilization is preceded by developments at the device- and material-level that harness previously unexplored physical (chemical, electronic, photonic) control. Herein, I detail my investigation into angular photon management strategies and the fundamental physics and chemistry of cesium lead halide perovskite nanocrystals ($CsPbX_3$ (X=halide)) (LHP). The emergence of this class of nanomaterials has already set in motion advances in solar energy technologies, light emitting diodes, and photonic qubits enabled by its exceptional photoluminescence tunability, near-unity quantum yield, defect tolerance, and unusually tunable excitonic response.

I explore the response of the out-of-plane transition dipole in $CsPbX_3$ nanocrystals to local electronic environment. The labile nature of the crystal allows us to induce an average orientation of excitonic transitions ranging from 40±1°to 47±1° from the surface via substrate modification in a morphologically isotropic nanocrystal thin film (theoretically 35.3° orientation). Further, I discuss the directed self-assembly of confined LHP nanocrystals into ensembles with tunable orientational ordering via liquid-air interfacial assembly and the resultant dipole orientations for face-to-face versus edge-to-edge assembly (46±2° and 28±2°, respectively). Additionally, my simulation of a demultiplexing luminophore-embedded photovoltaic module points to power conversion efficiencies of up to 31.7% (surpassing the record Si cell efficiency of 27.4%) while maintaining competitive device economics by use of a photonic luminescent solar concentrator (LSC) and motivates the implementation of anisotropic emitters.

By evolving nanoscale chemical and physical control as elaborated here, we can improve a suite of photonic technologies like sensing, solar, communication, quantum information, lighting, and integrated circuits. Application of new physical insights paired with rational device design will be key to addressing the current global energy climate.

The dissertation of Lindsey Ellen Parsons is approved.

Jane Pei-Chen Chang

Panagiotis D. Christofides

Aaswath Pattabhi Raman

Carissa Nicole Eisler, Committee Chair

University of California, Los Angeles

2025

TABLE OF CONTENTS

I. INTRODUCTION 1

a. Light directionality and optical device efficiency 1

b. Semiconductor nanocrystals 2

c. Luminophores, directional light emission, and transition dipole moment 5

d. Key metrology: Back Focal Plane Fluorescence Microscopy 6

e. Overview of the dissertation 11

II. PHOTONIC LUMINESCENT SOLAR CONCENTRATOR DESIGN FOR HIGH EFFICIENCY, LOW COST MULTIJUNCTION PHOTOVOLTAICS 14

a. Luminescent solar concentrators for cost competitive, high efficiency solar cells 15

b. Overview of the photonic LSC module 20

c. Simulation of the photonic LSC module 22

d. Resulting efficiencies for photonic LSC module 26

e. Expanding the model to anisotropic emitters 33

f. Ray tracing model for photonic LSCs 35

g. Conclusions and outlook 37

III. TUNABLE ANGULAR LIGHT EMISSION OF LEAD HALIDE PEROVSKITE NANOCRYSTAL THIN FILMS VIA SOLUTION-PROCESSED SUBSTRATE TREATMENT 39

a. Background 40

b. Optimization of ligand-controlled $CsPbBr_3$ perovskite nanocube synthesis for subsequent optical characterizations 43

c. Synthesis and characterization of colloidal perovskite nanocrystals for subsequent optical characterizations 49

d. Fabrication of perovskite nanocrystal thin films 51

e. Quantifying angular light emission 58

f. Conclusions and outlook 65

IV. ORIENTED DIPOLES IN ORDERED ENSEMBLES OF CONFINED LEAD HALIDE PEROVSKITE NANOCRYSTALS 67

a. Background 68

b. $CsPbBr_3$ nanoplate synthesis 69

c. Nanocrystal assembly at the air-liquid interface 70

d. Thin film characterization confirming ordering 81

e. Sensitivity and challenges of assembly 85

f. Resultant oriented dipoles 86

g. Liquid-air interfacial assembly for other morphologies of $CsPbBr_3$ 93
h. Conclusions and outlook 96
V. CONCLUSION 98
APPENDIX A: MATLAB CODE FOR CHAPTER II—PHOTONIC LUMINESCENT SOLAR CONCENTRATOR DESIGN FOR HIGH EFFICIENCY, LOW COST MULTIJUNCTION PHOTOVOLTAICS 100
APPENDIX B: SUPPLEMENTAL INFORMATION FOR CHAPTER III—TUNABLE ANGULAR LIGHT EMISSION OF LEAD HALIDE PEROVSKITE NANOCRYSTAL THIN FILMS VIA SOLUTION-PROCESSED SUBSTRATE TREATMENT 113
APPENDIX C: SUPPLEMENTAL INFORMATION FOR CHAPTER IV—ORIENTED DIPOLES IN ORDERED ENSEMBLES OF CONFINED LEAD HALIDE PEROVSKITE NANOCRYSTALS 122
REFERENCES 128

LIST OF FIGURES

Figure 1.1. 3
Figure 1.2. 4
Figure 1.3. 5
Figure 1.4. 6
Figure 1.5. 8
Figure 1.6. 13
Figure 2.1. 15
Figure 2.2. 17
Figure 2.3. 18
Figure 2.4. 19
Figure 2.5. 21
Figure 2.6. 22
Figure 2.7. 23
Figure 2.8. 24
Figure 2.9. 27
Figure 2.10. 28
Figure 2.11. 29
Figure 2.12. 30
Figure 2.13. 31
Figure 2.14. 32
Figure 2.15. 34
Figure 2.16. 35
Figure 2.17. 36
Figure 2.18. 37
Figure 3.1. 41
Figure 3.2. 44
Figure 3.3. 45
Figure 3.4. 46
Figure 3.5. 48
Figure 3.6. 51
Figure 3.7. 53
Figure 3.8. 54

Figure 3.9. 54
Figure 3.10. 56
Figure 3.11. 57
Figure 3.12. 59
Figure 3.13. 62
Figure 3.14. 65
Figure 4.1. 70
Figure 4.2. 71
Figure 4.3. 73
Figure 4.4. 74
Figure 4.5. 76
Figure 4.6. 78
Figure 4.7. 80
Figure 4.8. 81
Figure 4.9. 82
Figure 4.10. 83
Figure 4.11. 84
Figure 4.12. 85
Figure 4.13. 87
Figure 4.14. 89
Figure 4.15. 90
Figure 4.16. 91
Figure 4.17. 92
Figure 4.18. 94
Figure 4.19. 96
Figure B.1. 115
Figure B.2. 117
Figure B.3. 118
Figure C.1. 124
Figure C.2. 125
Figure C.3. 126

LIST OF TABLES

Table 2.1. 26
Table 3.1. 49
Table 3.2. 58
Table 4.1. 86
Table C.1. 127

ACKNOWLEDGEMENTS

I must first thank my research advisor and doctoral committee chair, Dr. Carissa Eisler, whose research vision, keen memory, intuition, wit, and empathy became the modus operandi for my tenure at UCLA. Learning from you has been a genuine privilege. I would also like to thank Dr. Jane Chang, Dr. Panagiotis Christofides, and Dr. Aaswath Raman for serving on my doctoral committee and providing their expertise and guidance in service of my understanding and for driving me to deliver my best work.

I would also like to acknowledge the funding sources that supported me and the work contained herein: the National Defense Science and Engineering Graduate Fellowship, the UCLA Center for Clean Technology Fellowship, and the National Science Foundation Faculty Early Career Development Program supporting Dr. Eisler.

UCLA delivered to me a community of colleagues and friends that deserve recognition for their support of my dissertation work and of me personally. I am grateful to my lab mates and my students who motivated and recentered me throughout this program. I would like to thank the staff of the Electron Imaging Center for Nanosystems at CNSI for continuously educating me on electron microscopy, and for their kindness, patience, and encouragement. I am grateful to my UCLA Brewins team who infused my days with camaraderie, creativity, and critical thinking about something other than nanocrystals. Thank you to my friends at UCLA who supported and inspired me and were a font of happiness and humor, Grace Vasiknanonte, Xintong Yuan, Saumya Jain, Cody England, and Mounika Dudala.

I am grateful to have had the opportunity to spend my penultimate summer in graduate school as a graduate intern at the U.S. Naval Research Laboratory. The experience of working amongst these fine scientists decisively advanced my technical skills and savviness, and by extension, my dissertation work. In particular I would like to thank my mentor Dr. Sarah Brittman for her enthusiasm and precision in the work and for ensuring that I had the means to succeed in DC. I would be remiss if I did not also thank Dr. Michael Simpson of the Office of Naval Research. His mentorship was a cornerstone of my graduate school experience, through which I refined my own career ambitions, and his sincere care, investment in my progress, and wonderful and/or astonishing anecdotes were a welcome constant.

I would like to thank my undergraduate institution Auburn University, which equipped me to become the engineer and scientist I am today. I attribute the caliber of my training to an expertly oiled program and to the wise and skillful professors from whom I learned. In particular I thank my undergraduate research advisor Dr. Virginia Davis for welcoming me into the nanoscale world, making it known that she believed in me, and modeling an aspirational research career.

Evidence of my own good fortune is the lifelong support system it has brought me, each and every member of which was required for my success in this program. My highest gratitude goes to Afreen Ali, Susanna and Dylan Daviscourt, Natalie George, Ryan McGill, Sasha Grishchenko, Gabriela Nerhood, and Mark Shannon. The ways you have touched my life extend far beyond this degree.

Finally, to my family, this achievement is ours. Thank you to my grandmother who was with me at every step of every experiment. Thank you to my aunt whose love and support were immensely felt. Thank you to my brother who never flinched at my lowest lows and always found a way to celebrate my highest highs. To all my family, thank you for your enthusiasm and encouragement and for inspiring determination, resourcefulness, and cleverness. Most of all, thank you to my parents, Leslie and Richard Chapman and Greg Parsons and Wendy Reed. Thank you for encouraging me to chase goals that felt out of reach, for promoting balance, for providing advanced life advice, and for being home base. I owe this adventure to the four of you.

Chapter II includes work that is based on Eisler, C. N.; Parsons, L. E.; Nett, Z.; Love, C.; Schwartzberg, A. M.; Alivisatos, A. P. Photonic Luminescent Solar Concentrator Design for High Efficiency, Low Cost Multijunction Photovoltaics. *Frontiers in Photonics* **2022**, *3*. https://doi.org/10.3389/fphot.2022.932913.

Chapter III is a version of Parsons, L.; Russ, B.; Eisler, C. Tunable Angular Light Emission of Lead Halide Perovskite Nanocrystal Thin Films via Solution-Processed Substrate Treatment. *ACS Nanoscience Au* **2025**. https://doi.org/10.1021/acsnanoscienceau.5c00054.

Chapter IV is a version of an unpublished manuscript submitted for publication, Parsons, L.; Grishchenko, A.; Eisler, C. Oriented Dipoles in Ordered Ensembles of Confined Lead Halide Perovskite Nanocrystals. *Submitted*.

VITA

Lindsey Parsons is a PhD candidate in Chemical Engineering at UCLA in the graduating class of 2025. Her dissertation work under Dr. Carissa Eisler focuses on the development of semiconductor nanomaterials and advanced photon management strategies. She is a recipient of the National Defense Science and Engineering Graduate Fellowship and was awarded the NSF Graduate Research Fellowship. She received the Center for Clean Technology Fellowship in 2022. In 2025, she received the UCLA Engineering Achievement Award for Student Welfare, and she was a finalist for the 2024 AIChE Graduate Student Award in Electronic and Photonic Materials. She also received the 2024 NDSEG Fellowship Conference Award for Honorable Mention Poster Presentation in Chemical Engineering.

During her time at UCLA, Parsons served as a graduate teaching assistant for Transport Phenomena I and II and was an instructor for the Bridge Review for Enhancing Engineering Students at the UCLA Center for Excellence in Engineering and Diversity. She was also a graduate intern at the U.S. Naval Research Laboratory in the Electronics Science & Technology Division, where she worked on the synthetic delivery of a novel semiconductor nanocrystal system. Parsons was the president of the Chemical and Biomolecular Engineering Graduate Student Committee from 2023-2024 and a founding member of the UCLA Brewins Graduate Beer Brewing Team.

Parsons earned her Bachelor of Chemical Engineering at Auburn University *summa cum laude*. She worked under Dr. Virginia Davis to understand stability and dispersion characteristics of manganese oxide nanowires. She was a recipient of the Spirit of Auburn Founder's Scholarship and the John W. and Rosemary K. Brown Scholarship.

I. INTRODUCTION

Our ever-growing energy needs in the age of the Internet of Things, now-ubiquitous large language artificial intelligence models, soaring cooling and refrigeration demands, and quantum computing, necessitate rapid developments to the field of optoelectronics. Calls for research attempt to meet this goal: for example, a 2011 program called SunShot established a federally funded research-based effort to eliminate technological barriers to solar energy and reduce the cost of solar below $0.06 per kilowatt hour by 2020, which was met in 2017. By 2030, they aim to reduce the cost of solar below $0.03 per kilowatt hour.[1] Currently, a bill sits before the U.S. Senate Committee on Energy and Natural Resources, the DOE Quantum Leadership Act of 2025, which would expand quantum research funding over the next five years including quantum computational science, quantum sensing, quantum communications, and materials science and engineering.[2] Simultaneous innovation of efficient and renewable energy sources and efficient device technologies is required to relieve the global energy strain.

a. Light directionality and optical device efficiency

Light direction (angle) and emitter quantum yield are determinant to the ultimate efficiency of an optoelectronic device. Improving quantum yield, or the efficiency of converting from an electron to a photon or vice versa, has been a primary focus of study, but with the development of emitters with near-unity quantum yield,[3] photon management emerges as a key limitation to higher efficiency devices. Outcoupling/trapping efficiency is limited by refractive index in bulk materials, but improvements are possible using nanoscale manipulation of light and interfaces.[4–6] For example, in an LED, outcoupling of light should be maximized such that light is directed to the escape cone, or the range of angles where emission is not subject to Total Internal Reflection. However, the maximum efficiency for planar LEDs still lies around 20%.[7,8] In order to surpass this limit, an approach from the nanoscale is required. Nanopatterning or scattering has been identified as one route to improve outcoupling, as well as the use of anisotropic emitters that preferentially direct light into the escape cone.[7–11] Another example of how angle manifests in device efficiency is the solar efficiency gains that are reported by use of a concentrator.[12] By

redirecting and concentrating light beyond one sun, the conversion efficiency of a photovoltaic may be improved (e.g. 29.1% vs 30.8% for GaAs).[12] Additionally, for solar applications that use a flat plane concentrator (Luminescent Solar Concentrator), the optical efficiency of the waveguide dictates what conversion efficiency is possible by limiting the fraction of photons that may be sent to the photovoltaic. Research suggests that the trapping efficiency may be improved by the use of wavelength-selective mirrors, a photonic crystal waveguide, or controlled emitter anisotropy.[5,13,14] Thus, nanoscale control of light directionality will be key to the next generation of optical technologies.

b. Semiconductor nanocrystals

One route to nanoscale light manipulation is semiconductor nanocrystals. Semiconductor nanocrystals are revolutionarily bright emitters due to their enhanced exciton binding energy over bulk materials. Quantum dots, or semiconductor nanocrystals whose sizes are at or below the confinement of an electron (Bohr radius), were the subject of the Nobel Prize in Chemistry in 2023 due to their highly size-tunable color.[15] As such, they are now ubiquitous in applications from LEDs to sensing, medicine, and beyond.[16]

In 2015, Protesescu et al. [17] revolutionized the field of semiconductor nanocrystals by synthesizing nanocrystals of lead halide perovskites by a colloidal hot injection method, which spurred interest in these materials due to their high quantum yield and composition- and size-based color tunability, as well as their relatively facile synthesis compared to other semiconductor nanocrystals (e.g. PbS, CdSe). They are semiconductors with an ABX_3 crystal structure where A is an organic or inorganic cation, B is a metal cation, and X is a halide anion. The octahedral lattice formed by BX_6 can tilt, resulting in a labile crystal nature and cubic, tetragonal, and orthorhombic crystal phases. The A site can incorporate large organic cations up to a certain size, beyond which the A site will confine the crystal to two dimensions, resulting in A_2BX_4 stoichiometry. Figure 1.1 shows composition-based color tunability across the entire visible range delivered by Protesescu et al.[17] and perovskite crystal structure in three dimensions.[18] Since 2015, perovskite nanomaterials of varying compositions (i.e. A = Cs^+, methylammonium (MA^+), formamidinium

(FA^+); B = Pb_2^+, Sn_2^+; X = Cl-, Br-, I-) and morphologies such as nanocubes, nanowires, and 2D nanoplates [17,19–21] have been synthesized in this rapidly expanding research area. In application, they already show promise for lighting,[22] encryption,[23] solar,[24,25] laser,[26] sensing,[27,28] scintillation,[29] and now quantum information technologies[30–32], and the annual number of research publications with the keyword 'perovskite' has more than tripled (Figure 1.2).

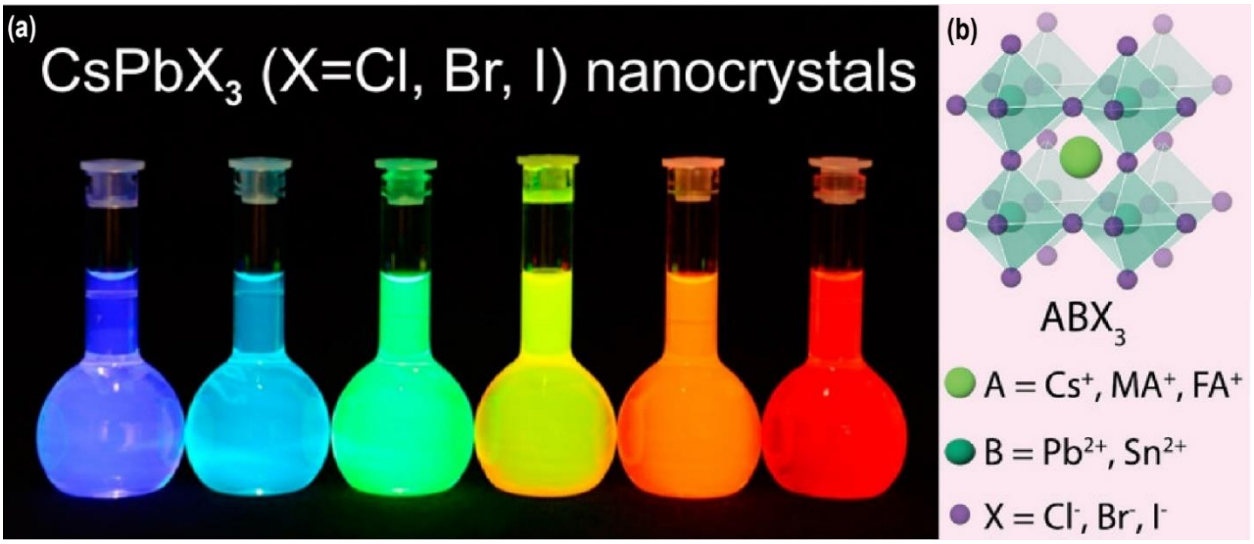

Figure 1.1. (a) Perovskite nanocrystals across the visible spectrum. Adapted from Protesescu et al.[17] (b) Crystal structure of 3D perovskite. Adapted from Sheehan et al.[18]

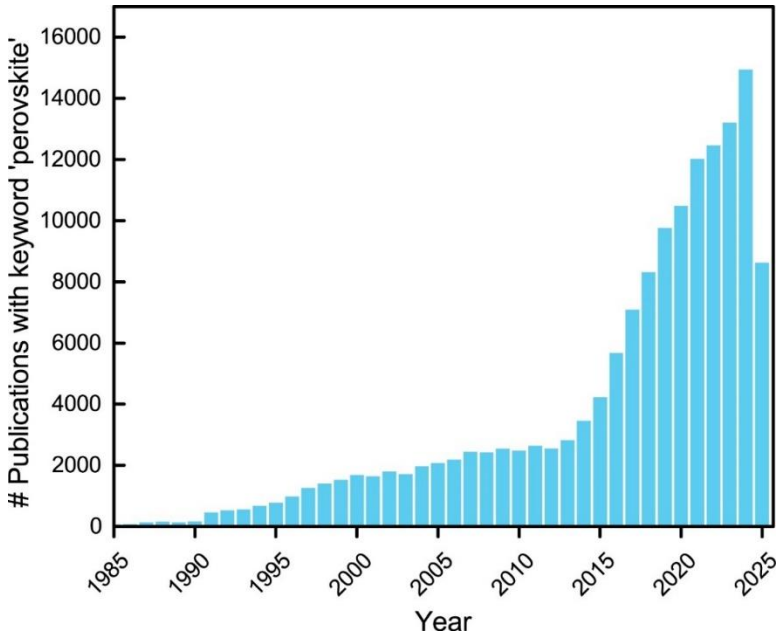

Figure 1.2. Frequency histogram displaying number of publications with the keyword 'perovskite' over time. Data derived from Clarivate Web of Science.[33]

Additionally, inorganic lead halide perovskites ($CsPbX_3$ (X=halide)) (LHP) nanocrystals have exhibited desirable properties such as remarkably high quantum yields,[34–37] quantum coherence and quantum optical properties,[38–41] single photon emission,[42–45] , large exciton binding energies,[18,46–48] and superfluorescence.[32,49–52] Notably, they have exhibited unique electronic tunability,[32,52] demonstrating a response by their electronic dipoles to surface charge redistribution.[22,53,54] This effect is attributed to their labile and ionic crystal nature,[55–57] which also presents a unique challenge in preventing dissolution or degradation of these highly sensitive materials. While efforts have been made towards improved surface functionalization and encapsulation,[57–62] robust and cost-effective implementation strategies remain a challenge. Demonstrating exciting potential to address the grand materials challenges of next generation devices;[63] we are motivated to further study the structure-property relationships and the mechanisms of the unique optical behavior in this young class of materials.

c. Luminophores, directional light emission, and transition dipole moment

The electronic transition dipole moment is used to describe the directional emissive behavior of luminophores. It is a convention which describes the angle between the plane of the surface and the vector of an electronic transition (Figure 1.3). The effective transition dipole moment (TDM) or dipole orientation factor in a thin film of emitters dictates angular light emission (along with the photonic density of states (PDOS) and refractive environment) by the generation of an electric field normal to the vector of the transition.[64]

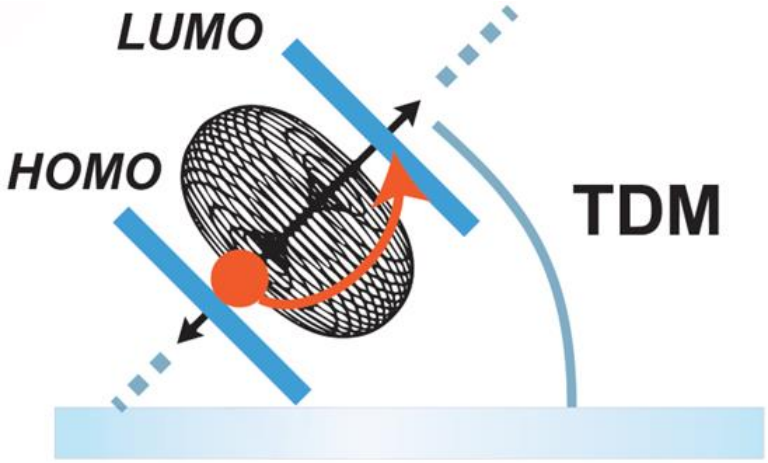

Figure 1.3. Electronic transition dipole moment

Films of traditional emitters of an isotropic shape (such as CdSe quantum dots) have equal dipole contributions along two in-plane and one out-of-plane axes, which corresponds to a TDM of 35.3° (isotropic).[65] Asymmetric confinement can reduce or eliminate dipole contributions along the axis of confinement.[66] The resulting light emission is reshaped at an interface. However, recent work showed that for perovskite nanocrystals, the out-of-plane (vertical) dipole contribution is exaggerated on most substrates for both isotropic (nanocube) and anisotropic (nanoplate) structures.[22,53,54] For example, on glass, the TDM of $CsPbBr_3$ nanocubes is 47°.[53] For the polarized emission cross section which is shown in Figure 1.4, this corresponds to a 7% increase in waveguided emission modes for the same PDOS at an air-glass interface over isotropic emission. On glass, the TDM of $CsPbBr_3$ nanoplates, which are asymmetrically confined in

the out-of-plane direction, is 29°.[22] This corresponds to a 3% decrease in waveguided emission modes for the same PDOS at an air-glass interface as compared to isotropic emission.

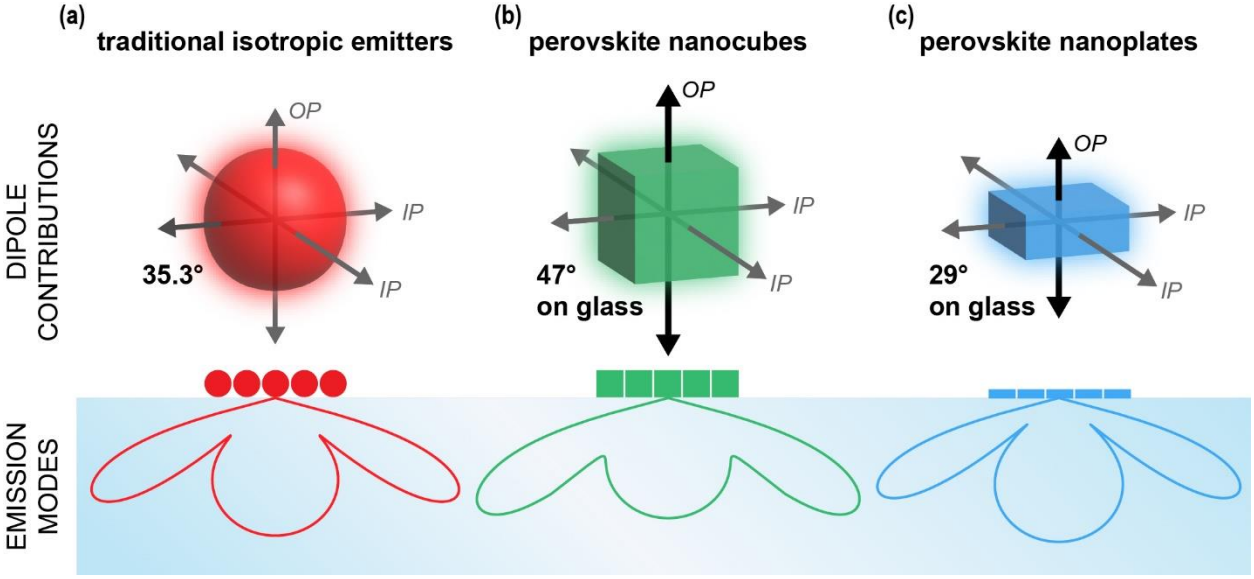

Figure 1.4. Prior Literature. Dipole contributions and emission (which is reshaped at an air-glass interface) for (a) traditional isotropic emitters with equal in-plane (IP) and out-of-plane (OP) dipole contrbutions,[65] (b) perovskite nanocubes with an enhanced OP dipole contribution on glass,[53] and (c) perovskite nanoplates with an enhanced OP dipole contribution on glass given the confinement along the out-of-plane axis.[22]

d. Key metrology: Back Focal Plane Fluorescence Microscopy

Measuring angle-resolved light emission

The electronic characterizations throughout this work rely on an uncommon type of microscopy, Back Focal Plane Fluorescence Microscopy (BFPFM), or Fourier plane imaging, where an achromatic doublet, or Bertrand lens, modifies the emission signal such that 3D angular emission is projected onto a 2D spatial plane (Figure 1.5 (a)). Thus, by changing a microscope focus from the sample plane to the Back Focal Plane within an objective, we can directly image the angular emission of a luminescent sample.[22,53,67] This not only allows us to interrogate the light pathways that would be observed in a device (Chapter II),

but also allows us to determine the alignment of emissive electronic states in our nanocrystal films (Chapters III and IV).

In this work we built an inverted fluorescence microscope, including Back Focal Plane imaging mode, according to the procedure described in Kurvits et al.[68] Thin film samples were excited by 405 nm continuous wave laser, and a wavelength-selective mirror (dichroic beamsplitter) was used to direct the laser beam to the back of a 100x oil immersion objective through which the sample was excited. For spatial imaging, fluorescence from the sample was collected by the objective and filtered by dichroic beamsplitter to minimize laser signal to the detector camera. A tube lens coupled to the objective focused the signal onto a CCD camera for collection.

To transform the setup to Fourier-plane imaging, a Bertrand lens was placed between the beamsplitter and tube lens which changed the focal plane from the real-space sample to the Back Focal Plane within the objective, creating a projection of the 3D angular emission pattern on the camera. [68] A linear polarizer was also added, which is necessary to extract the average angle of electronic transitions from the signal.

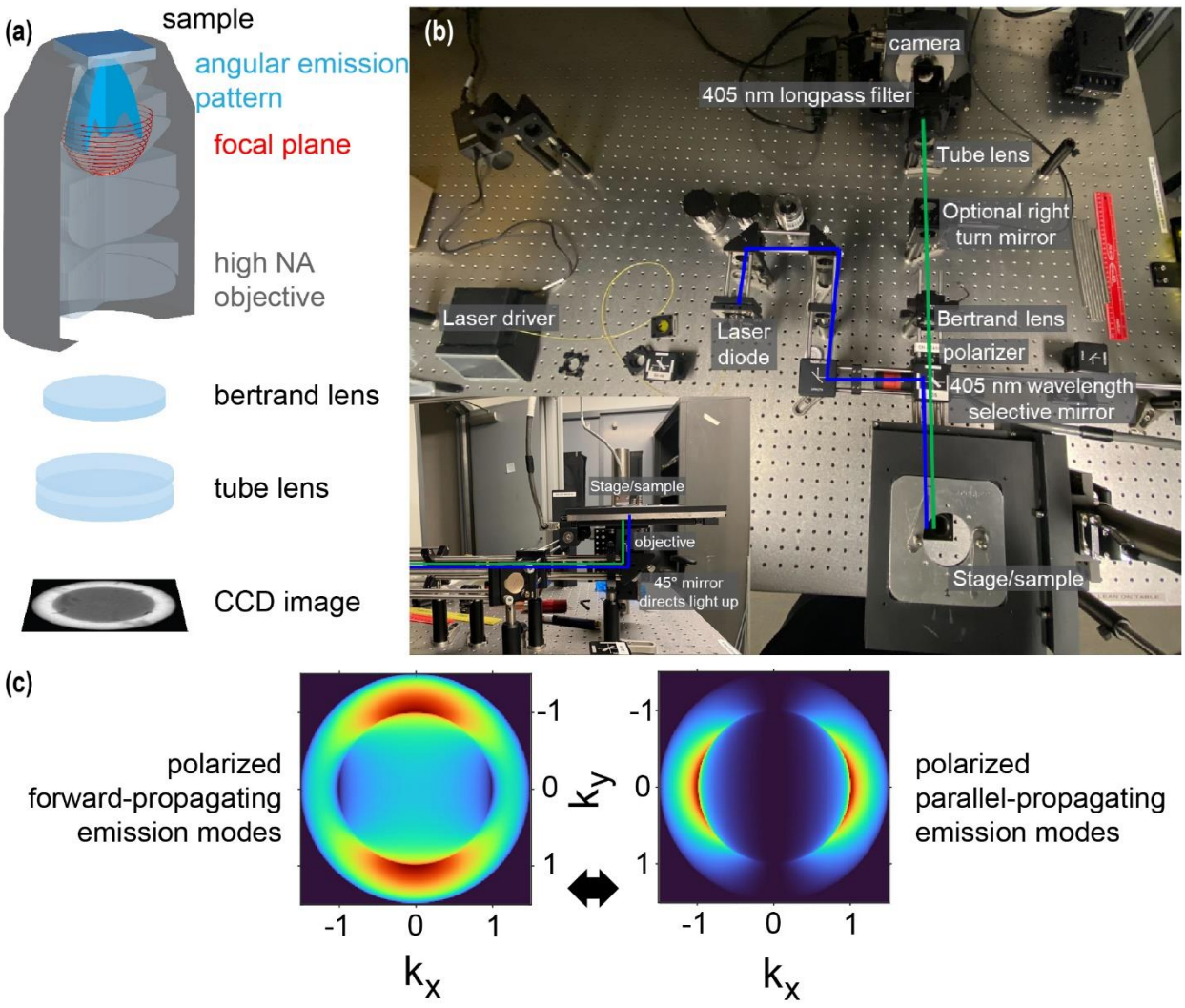

Figure 1.5. (a) Schematic showing the transformation of angular emission into 2D momentum space, or k-space via Bertrand lens. (b) BFPFM imaging setup where thin film samples are excited by laser at 405 nm (*blue*) and resulting emission is magnified 100x, linearly polarized, transformed to momentum space, and detected by CCD. (c) Examples of BFPFM signal for forward-propagating angular emission modes versus parallel-propagating angular emission modes.

Modeling angle-resolved light emission to extract effective transition dipole moment

We define the dipole orientation factor (Θ) as the relative dipole strength (p) of in-plane or parallel dipoles to all dipoles: [69]

$$\Theta = \frac{p_{\parallel}}{p_{\parallel}+p_{\perp}} \tag{1.1}$$

The orientation factor and effective transition dipole moment (TDM) are related by[64]

$$TDM = arccos(\sqrt{\Theta}) \tag{1.2}$$

The angular light emission pattern from dipoles within a thin film of emitters can be described by a three layer model where the top layer (n_1) is air, the middle layer (n_2) is the emissive film, and the bottom layer (n_3) is the glass substrate.[22,66,70,71] The horizontal dipole contribution along x is eliminated by linear polarizer in experiment, which allows us to decouple horizontal and vertical dipole contributions when fitting to experimental data. Polarized light emission intensity projected onto a 2-D collection plane (N_{pol}) as a function of photon momentum vectors along the x- and y-directions (k_x, k_y) is defined as:[67,71]

$$N^{pol}(k_x, k_y) = C\left[\frac{1}{2}\left(\rho_{IP}^{p} + \rho_{IP}^{s}\right)\cos^2(TDM) \ + \rho_{OP}^{p}\sin^2(TDM)\right] \tag{1.3}$$

or, in terms of orientation factor:

$$N^{pol}(k_x, k_y) = C\left[\frac{1}{2}\left(\rho_{IP}^{p} + \rho_{IP}^{s}\right)\Theta \ + \rho_{OP}^{p}(1-\Theta)\right] \tag{1.4}$$

where C is a normalization constant. ρ_{ip}^{s}, ρ_{ip}^{p}, ρ_{op}^{p} are photonic density of states in the *s*- and *p*-polarized, in-plane and out-of-plane directions governed by the thickness, refractive index, and emission wavelength of the emissive layer. Density of states in each direction are given by:

$$\rho_{IP}^{s} = \rho_{y}^{s}(k_x, k_y) = \left(\frac{1}{8\pi k_0^2}\right)\left(\frac{k_0}{k_{z,3}}\right)\left|\frac{t_{32}^{s} e^{\frac{ik_{z,2}D}{2}}(1+r_{21}^{s} e^{ik_{z,2}D})}{1-r_{21}^{s} r_{23}^{s} e^{2ik_{z,2}D}} \frac{k_y}{\sqrt{k_x^2+k_y^2}}\right|^2 \tag{1.5}$$

$$\rho_{IP}^{p} = \rho_{x}^{p}(k_x, k_y) = \left(\frac{1}{8\pi k_0^2}\right)\left(\frac{k_0}{k_{z,3}}\right)\left|\frac{t_{32}^{p} e^{\frac{ik_{z,2}D}{2}}(1-r_{21}^{p} e^{ik_{z,2}D})\frac{k_{z,2}}{n_2 k_0}}{1-r_{21}^{p} r_{23}^{p} e^{2ik_{z,2}D}} \frac{k_x}{\sqrt{k_x^2+k_y^2}}\right|^2 \tag{1.6}$$

$$\rho_{OP}^{p} = \rho_{z}^{s}(k_x, k_y) = \left(\frac{1}{8\pi k_0^2}\right)\left(\frac{k_0}{k_{z,3}}\right)\left|\frac{t_{32}^{p} e^{\frac{ik_{z,2}D}{2}}(1+r_{21}^{p} e^{ik_{z,2}D})\frac{k_x}{n_2 k_0}}{1-r_{21}^{p} r_{23}^{p} e^{2ik_{z,2}D}}\right|^2 \tag{1.7}$$

where

$$k_{z,i} = \sqrt{n_i^2 k_0^2 - \left(k_x^2 + k_y^2\right)} \tag{1.8}$$

$$k_0 = \frac{2\pi}{\lambda} \tag{1.9}$$

λ is the wavelength of the emitted light, n_i is the refractive index of layer i, t_{ij}^{l} and r_{ij}^{l} are the Fresnel transmission and reflection coefficients between layers *i* and *j* for *l*-polarized light, and D is the thickness of the emissive layer. The Fresnel coefficients for s and p polarized light are given by[22,66]

$$t_{ij}^{p} = \frac{2n_i n_j k_{zi}}{n_j^2 k_{zi} + n_i^2 k_{zj}};\ t_{ij}^{s} = \frac{2k_{zi}}{k_{zi}+k_{zj}};\ r_{ij}^{p} = \frac{n_j^2 k_{zi} - n_i^2 k_{zj}}{n_j^2 k_{zi} + n_i^2 k_{zj}};\ r_{ij}^{p} = \frac{k_{zi}-k_{zj}}{k_{zi}+k_{zj}} \tag{1.10}$$

We note that light emission in polar coordinates ($N^{pol}(\theta, \phi)$), where θ is the polar angle and ϕ is the azimuthal angle, is related to light emission in k-space by

$$k_x = k_0 n_3 \, sin\, sin\, (\phi) \;\; sin\, sin\, (\theta)\, ; k_y = k_0 n_3 \, sin\, sin\, (\phi) \;\; cos\, cos\, (\theta) \qquad (1.11)$$

This model for emission signal is compared to our measured BFPFM data, and the effective TDM of best fit is determined by $\chi 2$ minimization according to the procedure described in Russ et al.[72]

e. Overview of the dissertation

Here, I first explore the consequences of angular control in an example device, a luminescent solar concentrator; however, I quickly encounter the limits of efficiency gains afforded by an anisotropic refractive environment. These limits can be addressed by tuning the emission anisotropy of the emitter itself, motivating the bulk of this work. Thus, I move to explore two methods by which angle of light emission can be tuned and aligned in thin films of perovskite nanocrystals.

I expand on the optimized photonic luminescent solar concentrator+InGaP/Si dual junction solar module design proposed by Eisler et al.[73] to maximize conversion efficiency via optimizing device dimensions and luminophore concentration. My model simulates realistic optical losses of the photonic crystal waveguide and predicts module conversion efficiencies over 31% while maintaining cost competitiveness with single junction Si cells on a $/W basis. I expand the model to predict the potential efficiency payoff of incorporating anisotropic emitters. My ray tracing Monte Carlo simulation of an LSC gives design targets for luminophore quantum yield and trapping efficiency needed to reach 100x and 500x effective concentrations using a flat plane concentrator. This makes a case for expanding research efforts to improve waveguide trapping efficiency via anisotropic luminophore emission.

I synthesize cesium lead bromide perovskite nanocubes using in-air methods and report a nanocrystal cleaning procedure to maintain size-tunability observed in synthesis and morphological purity. I characterize the conformality (coverage, roughness) of $CsPbBr_3$ nanocube films on treated substrates and measure their angular emission signal. I induce a change in the effective transition dipole moment, which drives angular light emission along with the photonic density of states and refractive environment, by more

than 15% (47±1° to 40±1°) for films of identical composition and morphology by modulating the work function of the substrate.

I report a protocol for controlled face-to-face and edge-to-edge assembly of $CsPbBr_3$ nanoplates at the liquid-air interface. This control boasts manipulation of the effective transition dipole moment from 46±2°(edge up) to 28±2° (face down) by switching the axis of confinement from in-plane to out-of-plane. Finally, I demonstrate how this assembly method can be applied to other morphologies (nanocubes; nanoplates with aspect ratio >>100 nm) of $CsPbBr_3$ nanomaterials. The work elaborates three approaches working in concert in pursuit of advanced angular photon control (Figure 1.6).

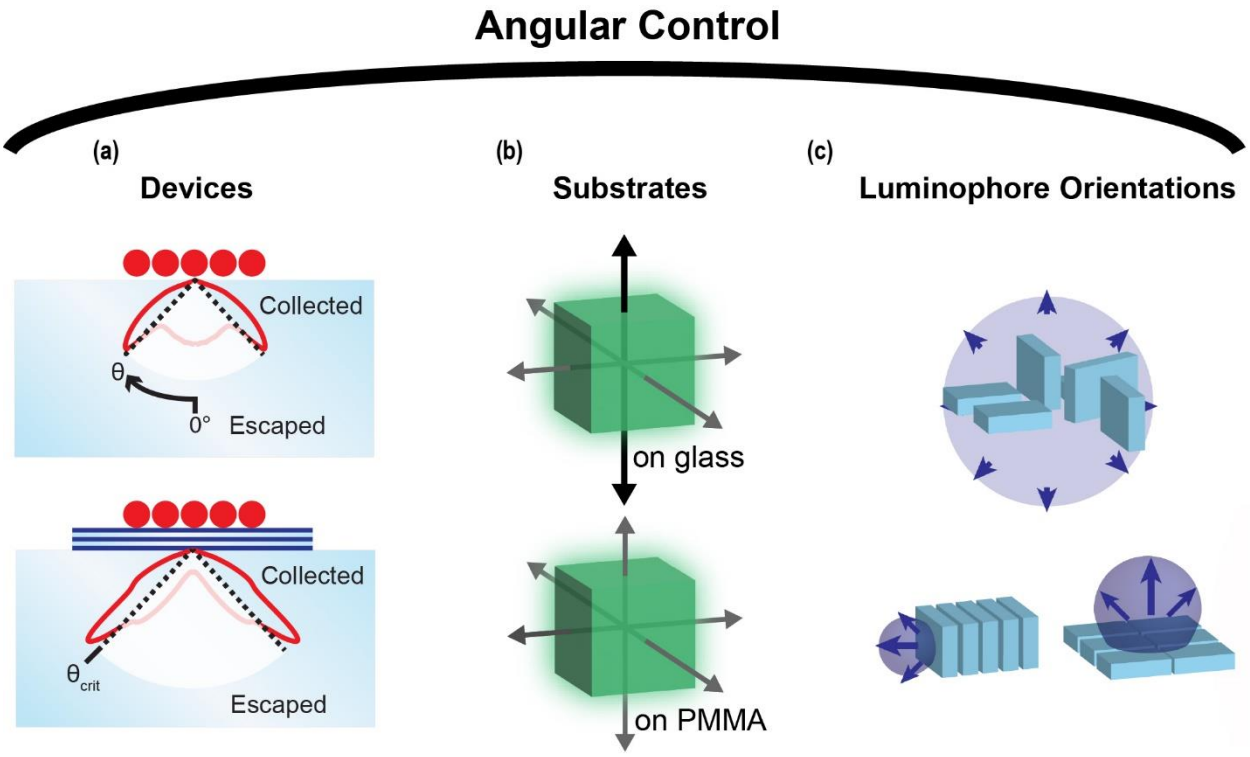

Figure 1.6. Schematic overview of the dissertation. (a) Simulations of a photonic crystal waveguide LSC module suggest efficiencies as high as 31.7% are possible for isotropically emitting luminophores. (b) The characteristically enhanced vertical dipole contribution in perovskite nanocrystals can be modulated by changing the substrate, resulting in an effective transition dipole moment ranging from 47±1° to 40±1° for a film of isotropically shaped nanocrystals. (c) Lightly confined perovskite nanoplates can be directed into edge up or face down assemblies such that the effective transition dipole moment is modulated from 46±2°(edge up) to 28±2° (face down).

II. PHOTONIC LUMINESCENT SOLAR CONCENTRATOR DESIGN FOR HIGH EFFICIENCY, LOW COST MULTIJUNCTION PHOTOVOLTAICS

Abstract

Photovoltaic conversion is most efficient when 1) absorbed photons are close to the bandgap energy of the semiconductor and 2) the difference in the angular spread of light between the source (sun) and converter (solar cell) is minimized. Thus, binning and concentrating the solar spectrum into multiple junctions delivers record efficiencies. A luminescent solar concentrator is a thin, flat, optionally wavelength-selective waveguide that concentrates light by leveraging total internal reflection modes. This device utilizes both color sorting and concentration to maximize efficiency. However, they are historically inefficient due to the compounding nature of their optical losses.

Nanophotonic light management offers a solution to combat these losses by precisely controlling the angle and direction of light to maximize collection to a specific area. This work aimed to show what efficiencies may be possible for an optimized nanophotonic LSC tandem module and to identify the design parameters needed to realize LSCs with competitive concentrations. Here, using modified detailed balance calculations and accounting for losses due to spectral non-selectivity, quantum yield losses, escape losses, and reabsorption losses, we predicted up to 31.7% conversion efficiency for the tandem module proposed herein, with the same $/W cost estimate as a single junction silicon cell. Using a Monte Carlo ray tracing model of an LSC, we showed that for trapping efficiencies of 90% and luminophore quantum yield of 90%, LSC concentrations of 100x may be possible.

a. Luminescent solar concentrators for cost competitive, high efficiency solar cells

A detailed balance gives a fundamental limit on power conversion efficiency of 33.1% for a single junction solar cell.[74] The bandgap of the absorber dictates this limit: all photons below the band gap are not absorbed and all photons above the band gap are not converted efficiently as any excess energy is immediately dissipated as heat.[4] Additionally, there is an entropic loss from the difference of the solid angle of incident sunlight (0.2 deg^2) and the radiative emission of the semiconductor (isotropic), as well as from the quantum efficiency of the absorber. Figure 2.1 shows the cumulative effect of these losses on efficiency. In 2024 the highest reported silicon cell efficiency was 27.4%, and the highest reported GaAs cell efficiency was 29.1%[12]—already approaching the fundamental limit. Thus, to make significant advances in efficiency, we need to move beyond the single junction cell design.

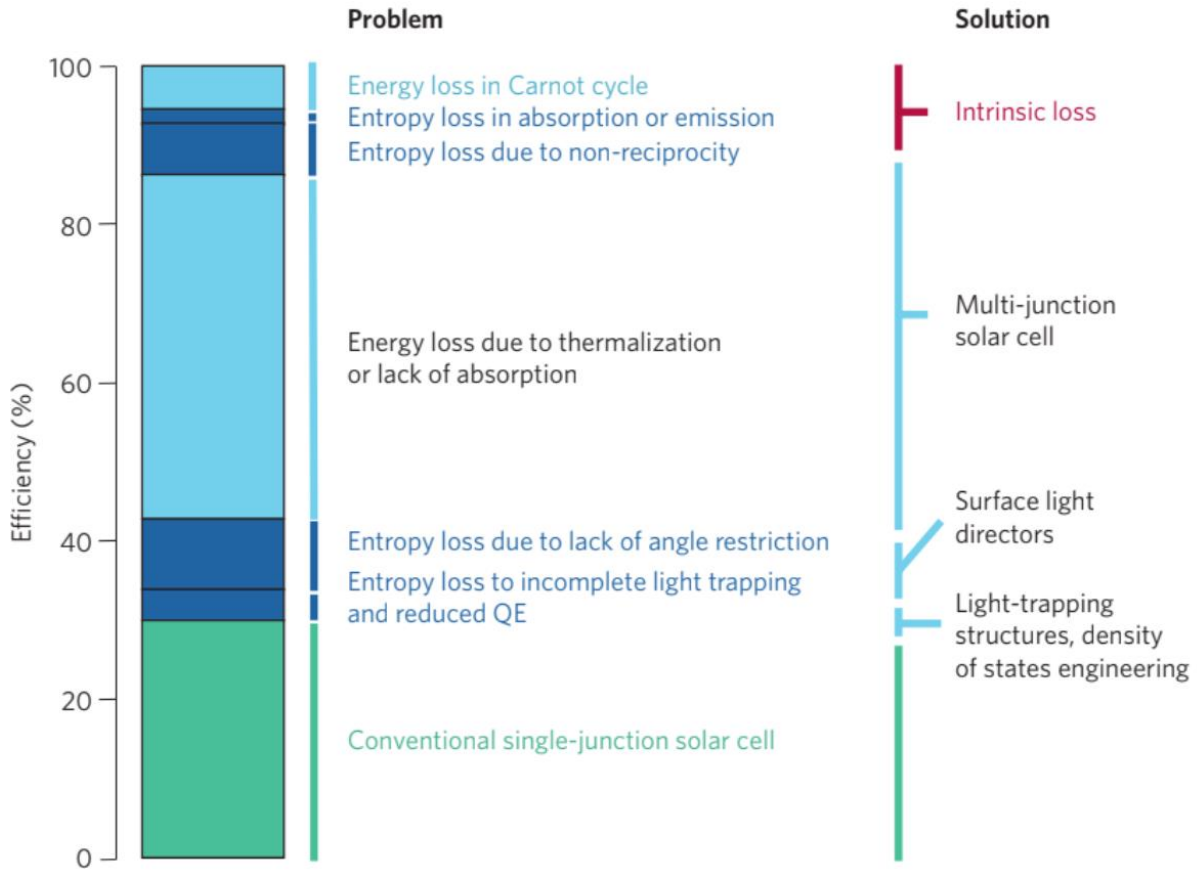

Figure 2.1. Thermodynamic loss mechanisms in a solar cell. Adapted from Polman et al.[4]

Multijunction cells can surpass the Shockley-Quiesser limit by reducing thermal losses that occur when energy is wasted above the bandgap and absorbing light over a broader spectrum. [75] In practice, efficiencies as high as 34.6% are reported using perovskite/Si subcells (2 junctions), and this increases to 38.8% for 5 junctions (without concentration).[12]

Light concentration can also be used to effectively improve conversion, delivering more photons to a smaller area. Additionally, it has the potential to significantly reduce cost by reducing the amount of material. This is particularly necessary for multijunction cells that employ expensive materials such as III-Vs with a manufacturing cost 2 to 3 orders of magnitude higher than silicon.[76,77] The theoretical upper limit of concentration is 46,000x, but solar modules have reported effective concentrations up to 1200x (where effective concentration is the geometric concentration scaled by concentrator efficiency) using optical structures like lenses and reflective troughs.[78,79] Unfortunately, typical concentrating methods are expensive, as these types of optics demand high precision glass and often require large trackers, which limits where they can be used and further increases costs. While efforts have been made toward the fruition of these designs for many years, and they have even been parts of major installations, [80] they remain largely cost prohibitive. Thus, we must find an alternative that allows us to benefit from multiple junctions and concentration that is cost effective and interfaces with current solar infrastructure.

Photonic Luminescent Solar Concentrators (LSCs) concentrate light by downshifting the sunlight and trapping the isotropic photoluminescence signal. In an LSC, incident light is absorbed by a luminophore and emitted at a redder wavelength. By taking advantage of the difference between refractive indices, some wavelengths of incident sunlight and reemitted photoluminescence signal can be totally internally reflected within the substrate (commonly a polymer or SiO_2) and waveguided to the edge of the material, with only a small portion of incident light being lost through the escape cone (angles at which incident light cannot be trapped). This phenomenon results in the geometric concentration of light equal to the geometric ratio of the incident area to the area of the sides of the device, where effective concentrations exceeding 10,000x are theoretically possible. [81] Figure 2.2 illustrates the phenomenon of waveguiding and concentration via LSC.

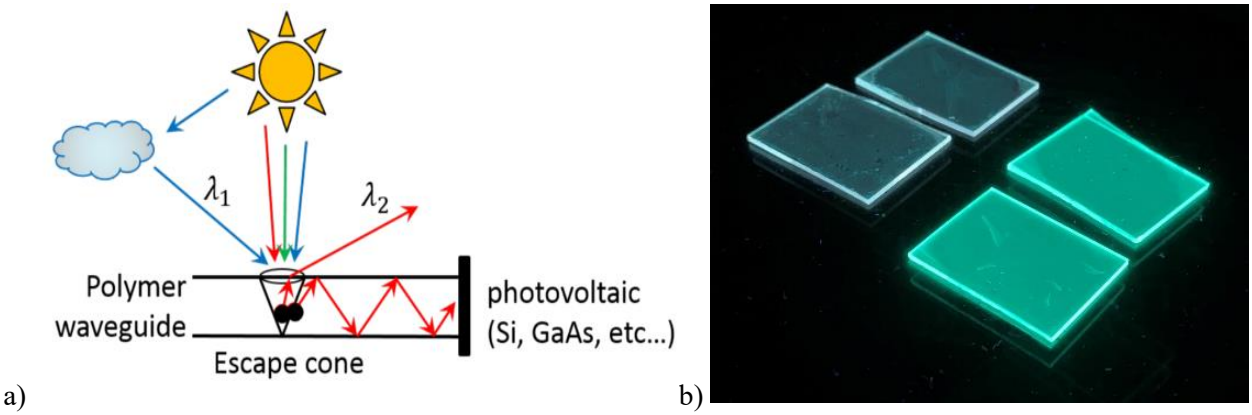

a) b)

Figure 2.2. (a) LSC waveguide diagram adapted from Bronstein et al.[82] (b) Photograph of LSCs we fabricated. Light propagates to the edge and is visibly concentrated.

Within such a device, optical losses mean that the practical performance limits are lower than the thermodynamic maximum. The three main types of optical losses that limit performance are: non-unity quantum yield, photon reabsorption, and escape losses. Quantum yield represents the ratio of photons emitted to photons absorbed. Previous work has been done to combat this loss and pushed quantum yields to near unity. [3,34] Reabsorption, when a photon is absorbed and emitted more than once before exiting the waveguide, may be combatted by increasing the Stokes shift between absorption and emission, tuning the pattern of reflection, or organizing materials in terms of decreasing bandgap to reduce the potential for absorption by a second luminophore after emission.[83–86] Improving quantum yield has been a primary focus of study, but with the development of particles with near-unity quantum yield, light trapping losses or escape losses emerge as the primary limitation to higher efficiency devices. Moreover, Kutayiah et al.[87] asserts that without modifying waveguide modes towards a higher trapping efficiency, an LSC cannot provide efficiency payoff in the case of the upper thermodynamic limit of solar cell efficiency. Thus, as we move towards high efficiency devices, trapping-modified LSCs will be paramount. Figure 2.3 summarizes potential losses within the device.

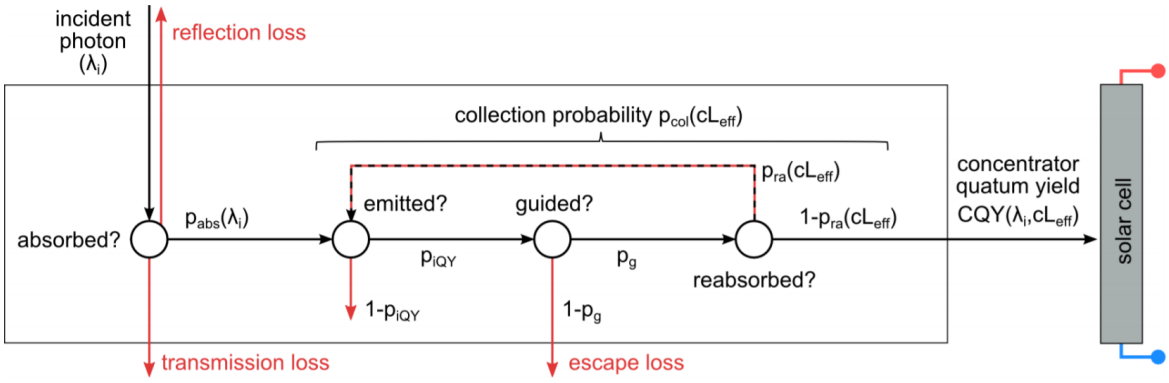

Figure 2.3. Optical loss mechanisms in an LSC. Adapted from Gutmann et al.[88]

One method to reduce escape loss is with an anisotropic refractive environment. Employing this approach, conventional LSC designs reached a concentration factor of 30x when researchers improved the device's quantum yield and introduced light trapping by color-selective mirrors that reflected luminophore fluroescence, reducing escape cone losses.[13] While this 30-fold concentration represents an important stride in luminescent concentrator technology, achieving concentrations approaching those in typical concentrating solar modules (~1000x) becomes increasingly difficult even when using fluorescence trapping mirrors. The mechanism of light trapping requires many reflective events for a photon to reach the edge of the device, and this is only magnified as concentration, and therefore geometric path length, is increased. Adapted from Bronstein's photon transport model,[82] Figure 2.4 (a) shows how even a very high reflectivity of 99% leads to substantially diminished light trapping and an effective concentration below 100x (geometric concentration 500x). Fabricating a reflective filter that maintains >99.999% reflectivity to prevent dramatic LSC optical loss (LSC efficiency) will be prohibitively complicated and expensive to realize.

One factor in the efficiency of a luminophore-embedded LSC is the trapping efficiency. For the mirrored LSC described above, trapping efficiency is govered by both filter reflectivity and number of reflective events for isotropic emission, resulting in rapidly compounding losses. By instead modifying the mode of emission, we can improve trapping efficiency intrinsically. Thus, research has turned towards

investigating anisotropic emission, which can be achieved by directly using luminophores with anisotropic emission tuned to bias emission towards the desired edge of the device.[8,22,53,66,89] This can be achieved via alignment of the emissive transition states in a material, which governs directional light emission (Chapter III and IV). Selecting for particles that can emit in a parallel mode to the LSC, we can reduce both the number of reflective bounces and the photons lost to the escape cone. Figure 2.4 (b) shows how alignment of emission modes towards parallel can improve light trapping within the device.[14]

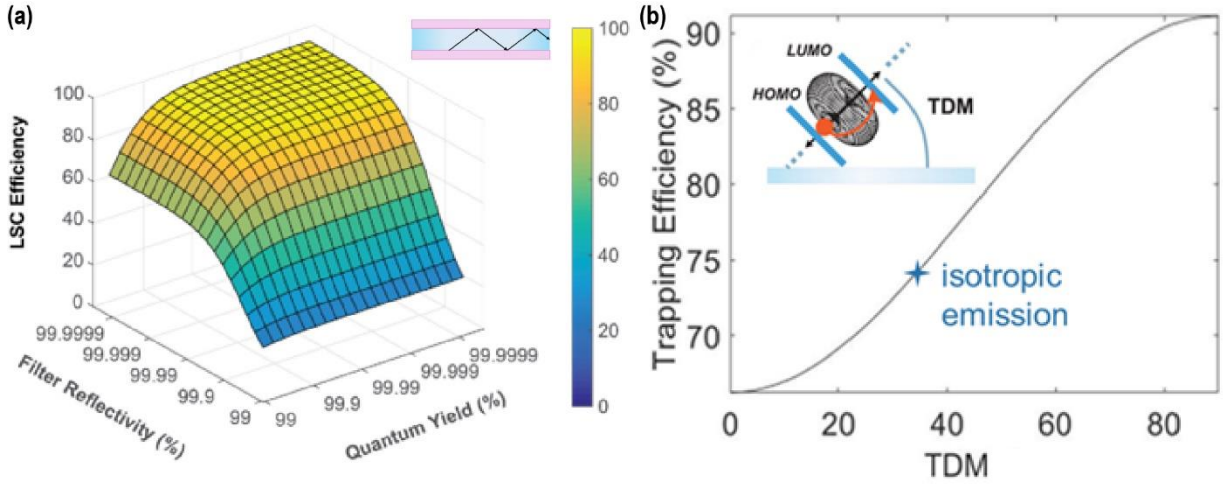

Figure 2.4. (a) LSC/waveguide efficiency of a device with a 500x geometric concentration as a function of absorber quantum yield and filter reflectivity.[82] (b) Light trapping as a function of effective luminophore TDM alignment for $RI_{surroundings}$ =1, $RI_{waveguide}$ = 1.5. Inset shows the angle by which the TDM is defined, which is between the substrate and the vector of the electronic transition [14]

This work shows that power conversion efficiencies of >30% are feasible by pairing alternating refractive index materials embedded with luminescent nanocrystals with photovoltaic cells—this provides an alternative to the typical multijunction cell. Additionally, simulation of an optimized LSC design shows promising results for its performance in an LSC+InGaP-Si module, where the non-traditional concentrating and spectrum splitting facets may yield performance strides beyond that of the standard silicon cell or even other multijunction technology while maintaining cost-competitiveness. We also present a Monte Carlo

simulation of LSC optical efficiency to further define characteristic LSC design principles and present design targets for waveguide and material properties necessary to rival state-of-the-art concentrators (>500x).[79] Combined, this work provides the foundation to model niche applications that require different spectral optimizations such as greenhouse solar,[90–92] building integrated photovoltaics,[93,94] or space-based solar.[95,96]

b. Overview of the photonic LSC module

First, we investigate a specific luminescent solar concentrator tandem design with anisotropic light emission. Tandem solar cell designs with silicon subcells are desirable because they achieve higher efficiencies while leveraging the low cost and overwhelmingly dominant market share of silicon solar cells.[97–99] While these cells can be efficient in practice (36.1%, 2024),[12] tandem cells remain largely cost prohibitive because of the expensive top subcell material. The design investigated here consists of an LSC coupled to an InGaP subcell and an unconcentrated Si subcell underneath, as shown in Figure 2.5. By coupling the top subcell to an LSC, a higher module efficiency can be achieved while minimizing the area coverage of the expensive material (InGaP).

One strategy to achieve anisotropic light emission, and therefore a more efficient luminescent solar concentrator, is by embedding the luminescent material within a nanophotonic structure or photonic crystal. This reshapes the angular light emission strongly into Total Internal Reflection modes by introducing constructive interference caused by periodic interfaces on the order of the wavelength of light.[5 100,101] The investigated design was a 100x (geometric)concentrating LSC that is a one-dimensional photonic crystal, containing alternating layers of high and low refractive index materials. Previous work has identified two pairs of refractive indices of the layers as design cases: $n_{high} = 2.1$ and $n_{low} = 1.5$ (*low contrast*) and $n_{high} = 2.4$ and $n_{low} = 1.5$ (*high contrast*). FDTD simulations of low and high contrast photonic crystals predicted a trapping efficiency of 74% and 89% respectively.[73] The low contrast case corresponds to Si_3N_4 and SiO_2, respectively, and is shown in Figure 2.5. Highly luminescent CdSe/CdS quantum dots are present within the low refractive index layers, and their light emission preferentially couples into high angle modes which

will be more efficiently transported to the InGaP subcell. Experimental and modeling work showed that this design had reduced photoluminescence escape losses and reduced reabsorption losses, which would make it a more efficient LSC when compared to a traditional design. [73] Because this design is a part of a tandem cell, we must also evaluate the practical validity in the context of color management. The device efficiency of the entire tandem cell will depend not only on how well the LSC concentrates and guides visible light to the InGaP subcell, but also on how efficiently it transmits near infrared light to the silicon subcell underneath.

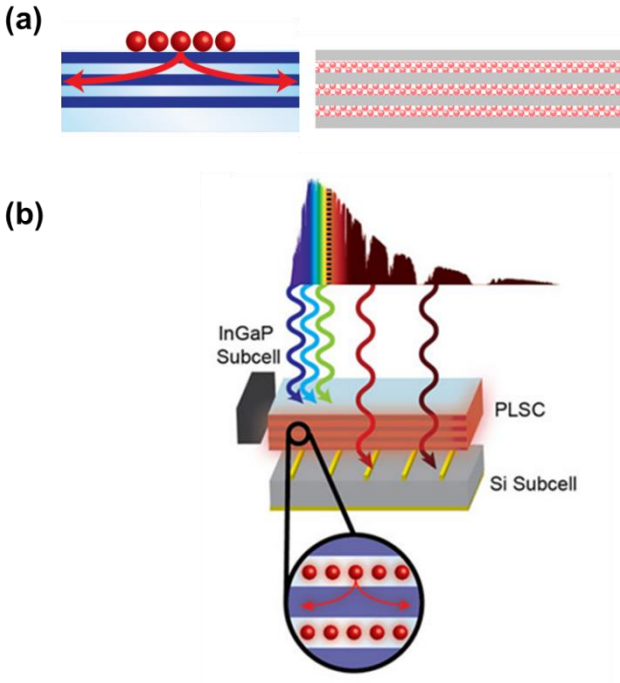

Figure 2.5. Light management and quantum dot schematic. (a) Gray represents Si_3N_4 and red dots represent quantum dots suspended in SiO_2[88] (b) Geometric design schematic of LSC module design where color indicates relative energies (dark red indicates infrared) [73]

We first investigated the design parameters for a generic LSC+InGaP-Si tandem solar cell that would be required to generate a conversion efficiency payoff over Si alone while minimizing the footprint of the InGaP subcell via concentration to maintain cost competitiveness. We used detailed balance calculations for an InGaP-Si tandem design under the AM1.5G Spectrum, which balances the incident and

emitted photon flux to calculate the resultant current generated by the cell. The spectrum was split at the bandgap of InGaP and assigned to a subcell such that constraints of concentration (the geometric ratio between the Si and the InGaP subcell), concentrator efficiency (for photons above the bandgap of InGaP), and the transmission efficiency (of photons below the bandgap of InGaP) could be determined. This design has merit in surpassing conversion efficiencies of the single junction silicon cell at modest concentrator and transmission efficiencies, and in the most optimistic cases could surpass a conversion efficiency of over 40%. Figure 2.6 shows coarse estimates of the sub module efficiencies, and the red dashed lines represent an efficiency of 26.7%, or the highest reported Si cell performance (2021). [102]

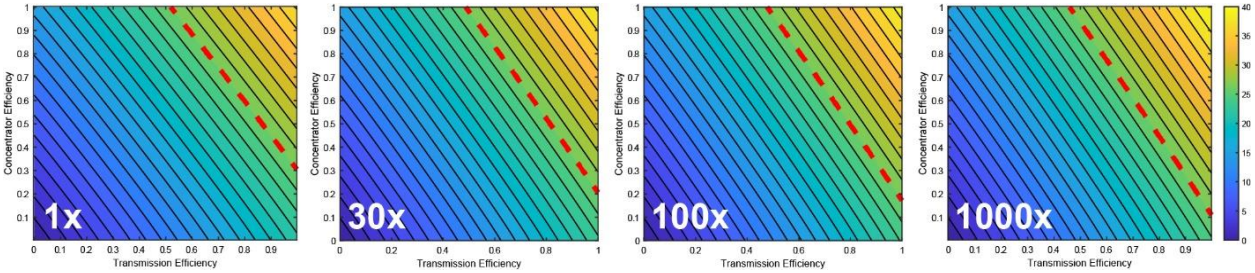

Figure 2.6. Coarse estimation of sub module efficiency for a generic LSC+InGaP-Si tandem solar cell at selected geometric concentrations as a function of concentrator and transmission efficiencies. Dashed line is 26.7% conversion efficiency, which was the highest reported single junction Si cell performance in 2021. [102]

c. Simulation of the photonic LSC module

We then apply this modified detailed balance calculation to optimize the specific design in Figure 2.5. For such a design, where transmission, absorption, and reflection spectra are modeled along with the optical loss mechanisms of quantum yield loss, escape loss, and reabsorption, we hypothesized that thinner waveguide designs would likely prevail. While a thicker waveguide containing more absorbers results in more absorbed photons in the InGaP band, it is susceptible to optical losses inside the waveguide, and delivery of low energy photons to the Si cell suffers due to increased reflection and absorption in the Si band.

In this simulation, light propagation through a stack of alternating layers is modeled using the transfer matrix method. We obtain transmission, absorption, and reflection spectra for stacks of varying numbers of layers and varying optical densities (i.e. varying amounts of CdSe/CdS quantum dots) using the transfer matrix method. These spectra are used to modify the AM1.5G spectra: the resulting transmission through the stack is sent to the Si subcell, the resulting absorption is used to calculate the light that is concentrated and sent to the InGaP subcell, and the resulting reflection is directed back towards the sun and therefore lost. Finally, these modified spectra are input to the modified detailed balance calculation to determine the total efficiency of the LSC+InGaP-Si tandem solar cell. Figure 2.7 provides a flow chart of the simulation procedure.

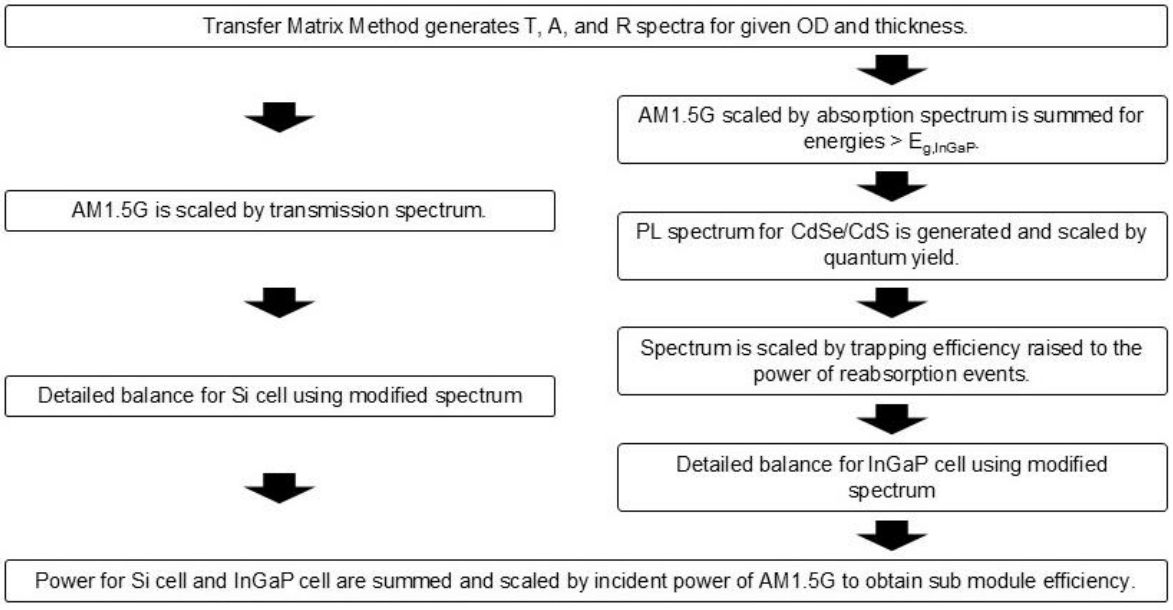

Figure 2.7. Overview of the modified detailed balance simulation for LSC+InGaP-Si tandem solar cell.

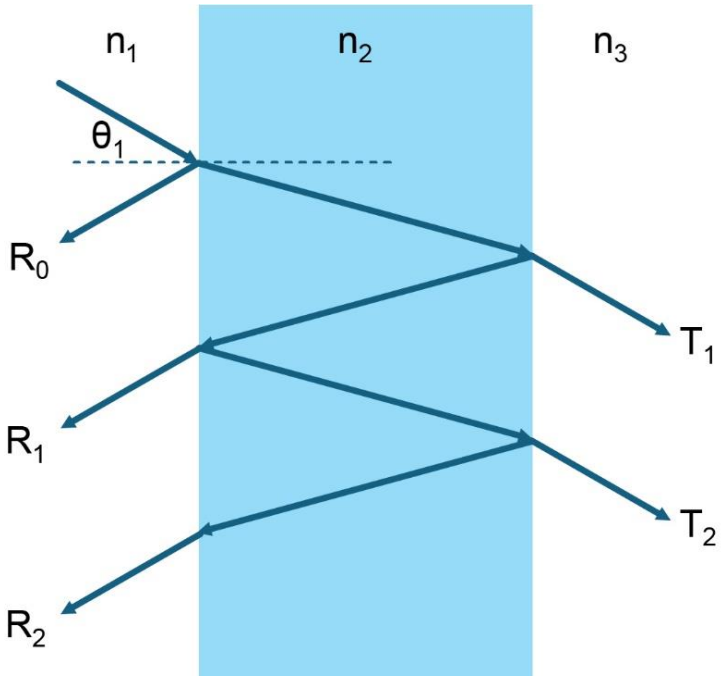

Figure 2.8. Light ray propagation through a single layer

To understand the propagation of light through the LSC, we must account for the refraction that occurs between each individual layer of the stack. We use the transfer matrix method for optics to model light propagation including absorption. A schematic of rays within one individual layer (Figure 2.8) illustrates this phenomenon. Using Fresnel reflections, the transfer matrix method uses the real refractive index n and the imaginary refractive index k, which accounts for absorption within a material. The imaginary refractive index is related to the absorption coefficient by Equation 2.1 and is used in layers where absorbers are present.

$$k = \frac{\alpha\lambda}{4\pi} \tag{2.1}$$

α is the absorption coefficient, and λ is wavelength. For our simulation, absorption data from synthesized CdSe/CdS quantum dots is used to calculate k. Absorption data is scaled such that α is the desired optical density at 450 nm. We executed the transfer matrix method using the open-source optical simulation

software OpenFilters [103], which yielded transmission, absorption, and reflection as a function of wavelength for LSCs of varying layers and absorber optical densities. The transmission-modified AM1.5G photon flux is sent to the Si cell.

The next steps describe the method to determine the photon flux that is sent to the InGaP cell. The absorption-modified photon flux above the bandgap of the CdSe/CdS quantum dots is summed and a normal distribution centered at the bandgap energy of the material is generated. This is then scaled by the quantum yield to account for photons lost in downshifting. Then, trapping and reabsorption losses are applied.

Reabsorption is modeled according to work by Olson [104]: a correlation established by a random walk simulation as a function of the density of absorbers present in the LSC and the average distance light must travel to exit the LSC. The correlation for this system is given by Equation 2.2, where the coefficient α is obtained from their simulation and provided in tabular form as a function of the ratio of distance between absorbers and the radius of the LSC,

$$N = \alpha\left(\frac{r}{l}\right)^2 \tag{2.2}$$

where N is the number of reabsorption events, α is the simulation-resultant coefficient, *r* is the radius of the LSC and *l* is the average step length, obtained from Equation 2.3 below,

$$l = \frac{ln0.5}{\epsilon C} \tag{2.3}$$

where ε is the extinction coefficient and *C* is the concentration of absorbers. Reabsorption and trapping efficiency is applied to scale the modified spectrum incident to the InGaP cell using the relationship given in Equation 2.4.

$$\eta_{trap,new} = \eta_{trap}{}^{N} \tag{2.4}$$

With consideration for non-idealities and practical upper limits, the model discussed here allows us to predict and understand the performance of an LSC-based architecture for tandem solar cell modules. The LSC essentially modifies the spectrum incident to the solar cell. So, using this method to modify the AM1.5G spectrum for different given parameters (number of layers and optical density) we can then perform a detailed balance calculation on each cell component.

We then combine these spectra with literature values for high performance but still realistic solar cells (Table 2.1) into detailed balance calculations (modified from Warmann et al.[105]) to determine the max power output for each subcell of the module, which are assumed to be independent. The total efficiency of the entire module using Equation 2.5,

$$\eta_{sub\ module} = \frac{P_{InGaP}[W/cm^2] + P_{Si}[W/cm^2]}{0.1\ W/cm^2} \tag{2.5}$$

where $\eta_{sub\ module}$ is efficiency and P is the power output of each subcell. Varying different parameters gives an estimate of the ideal optimum to maximize device efficiency, or in other words, balance the collection efficiency of LSC and the transmission of lower energy photons to the Si subcell.

Table 2.1. Values used in modified detailed balance at each junction. [106]

	Si	**InGaP**
E_g (eV)	1.14	1.84
ERE	0.01	0.05
Absorption	0.9649	0.8989

d. Resulting efficiencies for photonic LSC module

For the LSC+InGaP-Si tandem device design presented in Figure 2.5, we varied the number of layers from 4 to 86 (or total LSC thickness from 0.0018 to 0.0745 mm) and the optical density of the CdSe/CdS and quantified the expected resulting efficiency. Figure 2.9 shows an example of simulated

transmission, absorption, and reflection spectra for a waveguide with 6 layers, low contrast device design, and optical density of 1. Note that lower energy photons are transmitted while higher energy photons are absorbed, which will maintain high spectral efficiency, ensuring that high energy photons are directed to the higher bandgap InGaP subcell while low energy photons are transmitted to the lower bandgap Si subcell. Note also that reflected light is lost upon incidence.

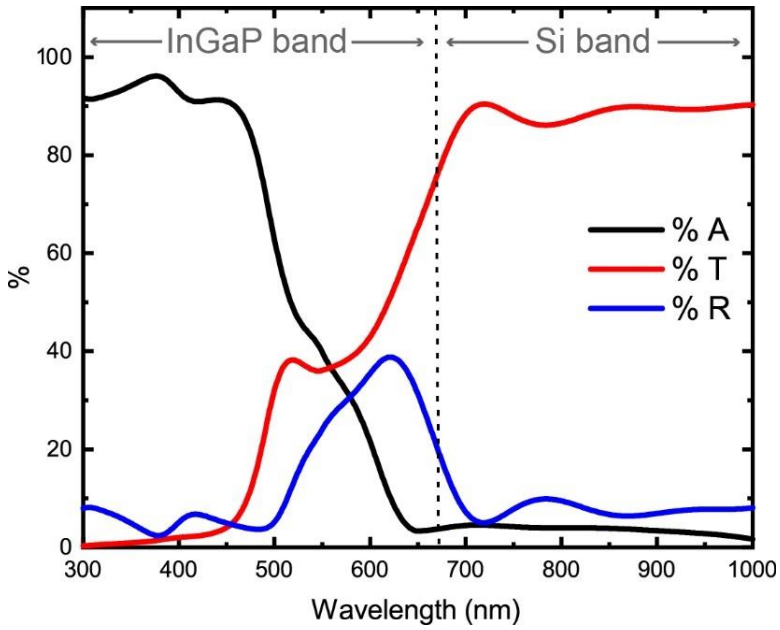

Figure 2.9. Transmission, Absorption, and Reflection spectra for a 6-layer, low contrast device design with an absorber optical density of 1

Figure 2.10 shows the parametric optimization for this design in the absence of optical losses (quantum yield, trapping/escape, reabsorption) in the LSC beyond absorption. Here, we isolate just the nonidealities in using a multilayer stack, resulting in a tradeoff between absorbing high energy light in the LSC while still transmitting NIR light for the Si bottom subcell. For the lower and higher contrast case, thinner devices with an optical density of 3 to 3.5 prevail. For a geometric concentration factor of 100x (i.e. the Si subcell is 100x larger than the InGaP subcell), a maximum efficiency of greater than 37%—surpassing both the record single junction silicon cell and InGaP/GaAs/Si multijunction cell performance[12]—is demonstrated for an optical density of 3 and an LSC thickness of 7.1 μm in the low

contrast case. In other words, this maximum is the result of a tradeoff between losses in spectral efficiency and losses to reflection.

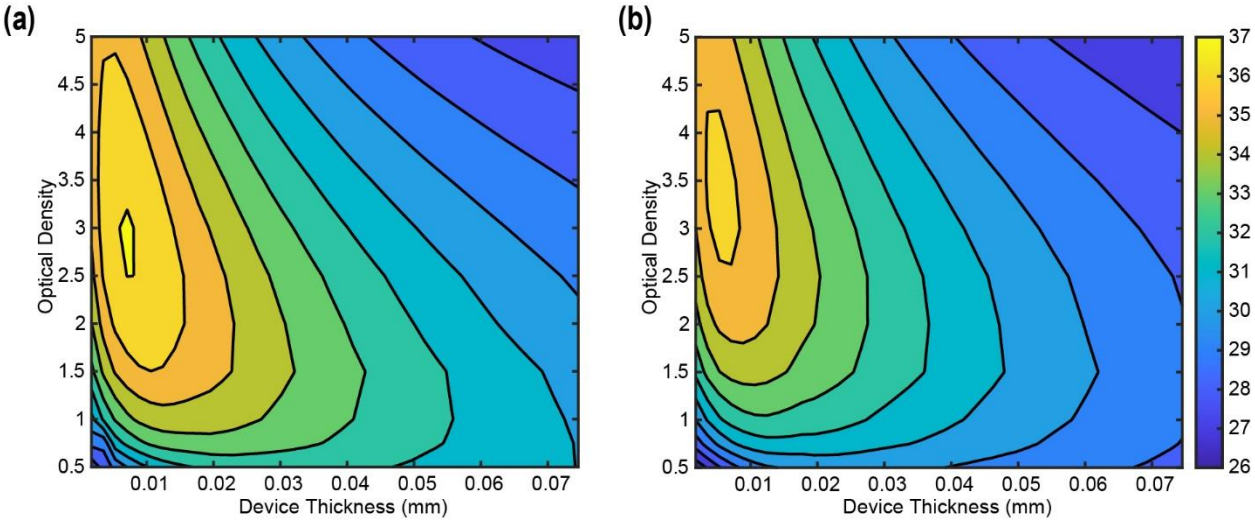

Figure 2.10. Sub module efficiency for a 100x concentrating device with no optical losses where (a) n_{high} = 2.1 and n_{low} = 1.5 and (b) n_{high} = 2.4 and n_{low} = 1.5.

Figure 2.10 represents a highly idealized LSC case. Next, we include realistic optical losses that will result from the LSC. As perovskites and other semiconducting nanoparticles become more ubiquitous and the limits of their performance are pushed higher, we can realize a device in which the quantum yield is near-perfect. Experimental work by Hanifi et al.[3] demonstrates quantum yields of up to 99.6% in CdSe/CdS core/shell nanoparticles. Based on their reporting, our initial model makes a conservative estimate of absorber quantum yield at 98%. When accounting for a less than unity quantum yield in our model, we see a uniform depression of efficiency for all parametric variations because a fraction of all absorbed photons are lost to non-radiative emission. Because the quantum yield does not change the spectral characteristics of the luminophores, the same parameters produce an optimum, where the maximum efficiency is reduced to 36.5%, demonstrated in Figure 2.11.

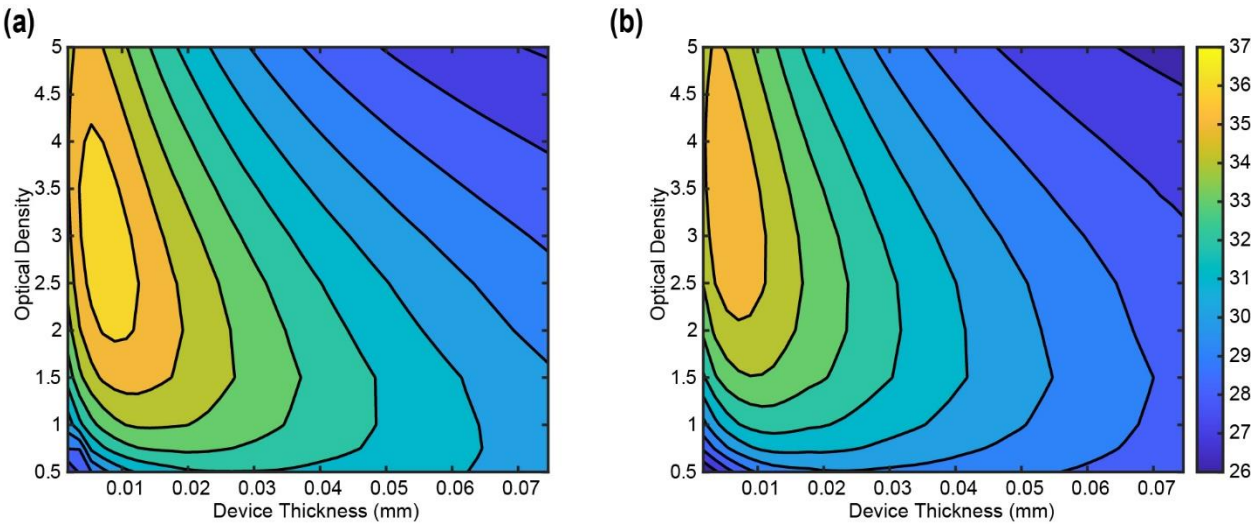

Figure 2.11. Sub module efficiency for 100x device with 0.98 absorber quantum yield where (a) n_{high} = 2.1 and n_{low} = 1.5 and (b) n_{high} = 2.4 and n_{low} = 1.5. No escape or reabsorption losses are yet modeled.

In the simulations for Figure 2.10 and 2.11, which are agnostic of the FDTD modeled trapping efficiency for the high and low contrast design,[73] the low contrast design has prevailed due to decreased reflection losses and improved spectral efficiency. However, accounting for the trapping performance in each design represents another optical loss in which the higher contrast case is expected to prevail, with a trapping efficiency of 89% over 74% for the low contrast case. The result is shown in Figure 2.12.

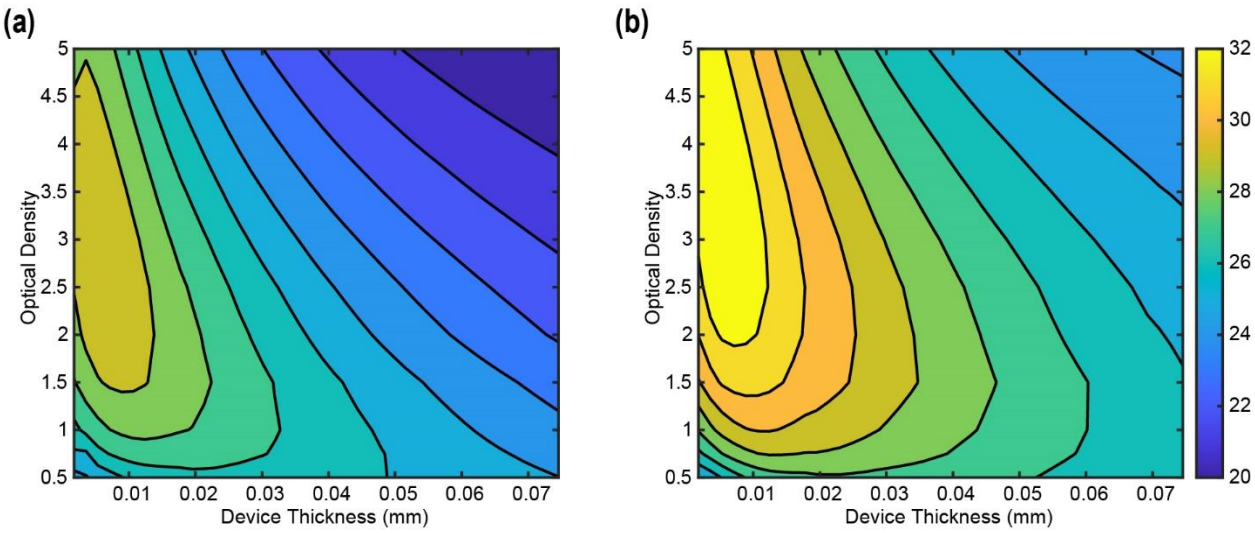

Figure 2.12. Sub module efficiency for 100x device with 0.98 absorber quantum yield where (a) n_{high} = 2.1, n_{low} = 1.5, and η_{trap} = 0.74 and where (b) n_{high} = 2.4, n_{low} = 1.5, and η_{trap} = 0.89. No reabsorption losses are yet modeled. The high contrast case now surpasses the low contrast case due to reduced escape losses. Note that the colormap range is from $\eta_{\text{sub module}}$ = 20% to $\eta_{\text{sub module}}$ = 32%.

Reabsorption is another major loss mechanism for LSCs. Reabsorption is the absorption of a photon by another instance of the same absorber, which risks again quantum yield losses and escape losses as well as further downshifting. Figure 2.13 shows how the number of reabsorption events can vary with thickness, concentration, and optical density. Reabsorption is a function of LSC radius (via geometric concentration and thickness) and absorber optical density. The likelihood of an emitted photon encountering and therefore being reabsorbed by another quantum dot increases as the radius of the LSC increases (and thereby the device thickness in order to maintain the same geometric concentration) and as optical density increases; this is simply because there are more quantum dots to be encountered as a photon propagates.

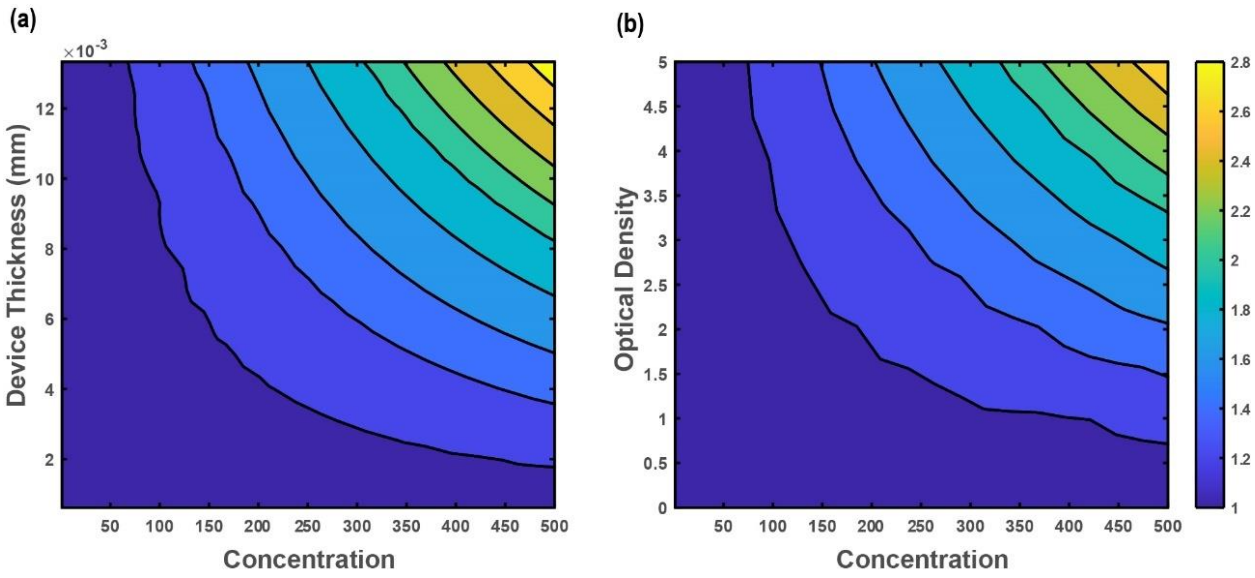

Figure 2.13. Reabsorption events for low contrast LSC (a) with optical density 0.5 and (b) with 8 layers

Figure 2.14. shows the resulting expected efficiency of this LSC+InGaP-Si design including the realistic LSC optical losses (measured quantum yield 98%, reabsorption). For the case in which the high RI was $n_{high} = 2.1$ and the low RI was $n_{low} = 1.5$, our modified detailed balance model predicts a maximum efficiency of 28.1% (Figure 2.14 (a)). For the ideal design case where $n_{high} = 2.4$ and the low RI was $n_{low} = 1.5$, we predicted a maximum efficiency of 31.7% (Figure 2.14 (b)). For a 100x concentration factor, this optimum occurs at an optical density of 3 to 3.5 and at low device thicknesses, which reduce the risk of optical losses and spectral losses due to undesirable reflection and absorption of near infrared light.

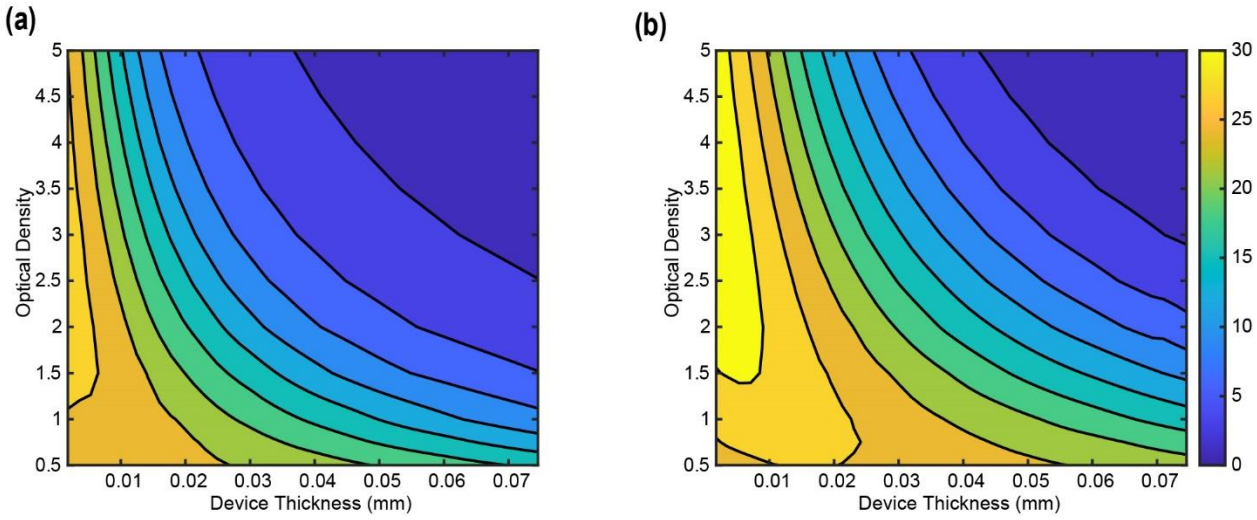

Figure 2.14. Simulated efficiency of the photonic LSC module. Multijunction cell efficiency (contours) is plotted as a function of CdSe/CdS optical density at 450 nm (quantum dot concentration) and photonic LSC thickness (number of layers). The efficiency is plotted for periodic structures (t_{low} = 100 nm, t_{high} = 210 nm) for a. n_{high} = 2.1 (a) and b. n_{high} = 2.4. The low contrast case is capable of >28% efficiency, and the high contrast case is capable of >31% efficiency. Note that the colormap range is from $\eta_{\text{sub module}}$ = 0% to $\eta_{\text{sub module}}$ = 30%.

This maximum is the result of a tradeoff between losses in spectral efficiency and optical losses in the LSC. If the optical density of absorbers is too great, a significant fraction of photons is lost to reflection and reabsorption losses. If the optical density of absorbers is too low, too many high energy photons are transmitted to the Si cell, which results in a diminished spectral efficiency. A similar effect arises for LSC thickness: if the device thickness is too high, undesirable reflection and reabsorption occur. We have demonstrated that a device efficiency of up to 31.7% is possible for our proposed spectrum splitting module. Both designs prove competitive with high performing single junction Si cells, with a maximum reported efficiency of 27.4%,[12] and even approach some dual-junction InGaP/Si cells while being appreciably cheaper by using less of expensive materials such as indium, as well as by the solution-processed nature of the LSC itself.

Preliminary estimates show that this design could be competitive on a $/W basis with the single junction Si cell and could well out-perform a traditional InGaP/Si tandem cell. Literature reports a cost estimate of the InGaP/Si tandem cell as $320/m^2, [77] and a cost estimate of the silicon solar cell is $90/m^2.[107] Cost estimates of comparable LSCs are $5/m^2.[108] Scaling by conversion efficiency and the irradiation of the AM1.5G per area, a preliminary $/W estimate of an InGaP/Si tandem cell is $0.94/W for a conversion efficiency of 34%, and a silicon cell is estimated at $0.35/W for a conversion efficiency of 26%. To estimate cost of our module, the cost of the InGaP subcell is scaled by the geometric ratio of the module, giving a $/W estimate of $0.35/W for 31% conversion efficiency.

e. Expanding the model to anisotropic emitters

An ensemble of CdSe/CdS quantum dots will emit isotroptically. [65] We wanted to expand our model to understand how anisotropic emission of the luminophore—coupled into the already highly anisotropic waveguiding modes of a photonic crystal—could lead to conversion efficiency gains by boosting trapping efficiency in the waveguide [14,109,110]. Figure 2.15 shows that for the low RI contrast architecture studied above, trapping efficiency improvements could boost sub module efficiency more than 6.5% beyond the studied optimum of 28%. Trapping efficiency of 90% could result in a sub module efficiency >31%, and a trapping efficiency of 95% could result in a sub module efficiency >34.5%.

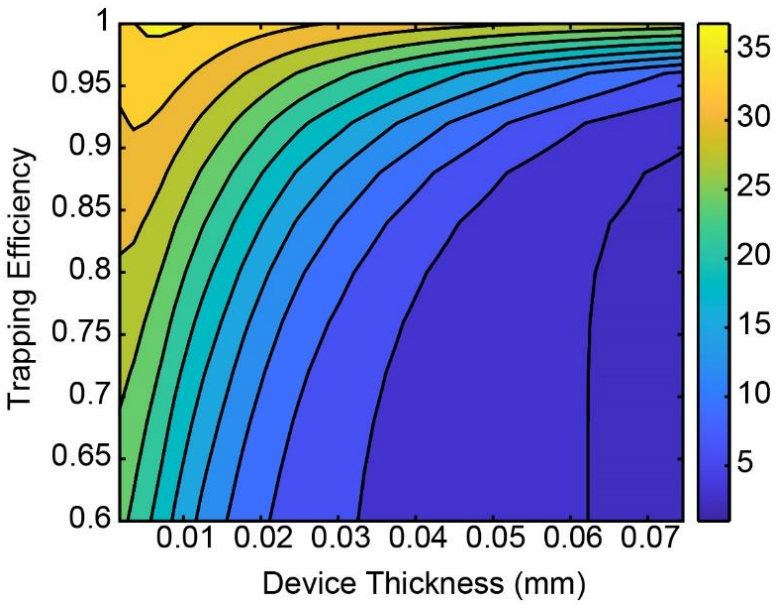

Figure 2.15. Effect of trapping efficiency and device thickness on sub module efficiency for the specific topology of the previous section, where OD = 3, QY = 98%, n_{high} = 2.1, and n_{low} = 1.5

Mulder et al.[14] describes how dye (emitter) alignment, which is described here as the TDM or effective angle of electronic transitions in a material, can improve trapping efficiency. Figure 2.16 shows sub module efficiency design spaces that arise from reported trapping efficiencies in a single layer waveguide[14] corresponding to horizontally aligned emitters (forward-propagating light modes), isotropic emitters, and vertically aligned emitters (parallel-propagating light modes). Note that trapping efficiency improvement is expected for a photonic crystal waveguide over a single layer waveguide.

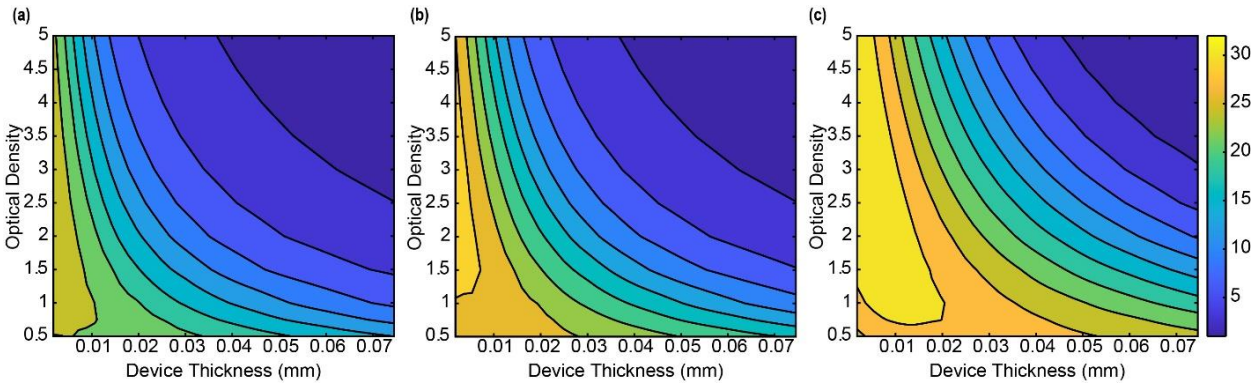

Figure 2.16. Sub module efficiency for a 100x concentrating device for trapping efficiencies equivalent to a. horizontal (n_{trap}=66.2%), b. isotropic (n_{trap}=74.5%), and c. vertical TDM aligment (n_{trap}=91.1%) in an isotropic medium, according to the relationship of emitter alignment and trapping efficiency developed by Mulder et al. [14] Note that an aligned emitter within a stack design can be optimized to show further enhancement of trapping efficiency.

We observe significant improvements to our predicted efficiency (increased sub module efficiency by 7.8% efficiency using vertical over horizontal emitters) when we consider how trapping can be promoted within our device. Vertically-aligned emitters have the potential to magnify the effects of successful light management by the LSC.

f. Ray tracing model for photonic LSCs

We were interested in understanding how other high-performing luminophores might enable concentration gains beyond 100x in waveguiding photonic LSCs. Hence, we leveraged a Monte Carlo ray tracing simulation to model the propagation, absorption, optical losses, and collection of a limited number of photons (10,000) in thin film waveguides.

The model assigns photons to discretized positions across the LSC, as well as an initial direction (up, down, left, right) inside the LSC. To assess the photons at each node at each arbitrary timestep, a probability is randomly generated that dictates whether the photon will move to a neighboring node, be collected by

reaching the edge of the LSC, or be absorbed and potentially lost by quantum yield or escape losses according to the decision tree in Figure 2.17.

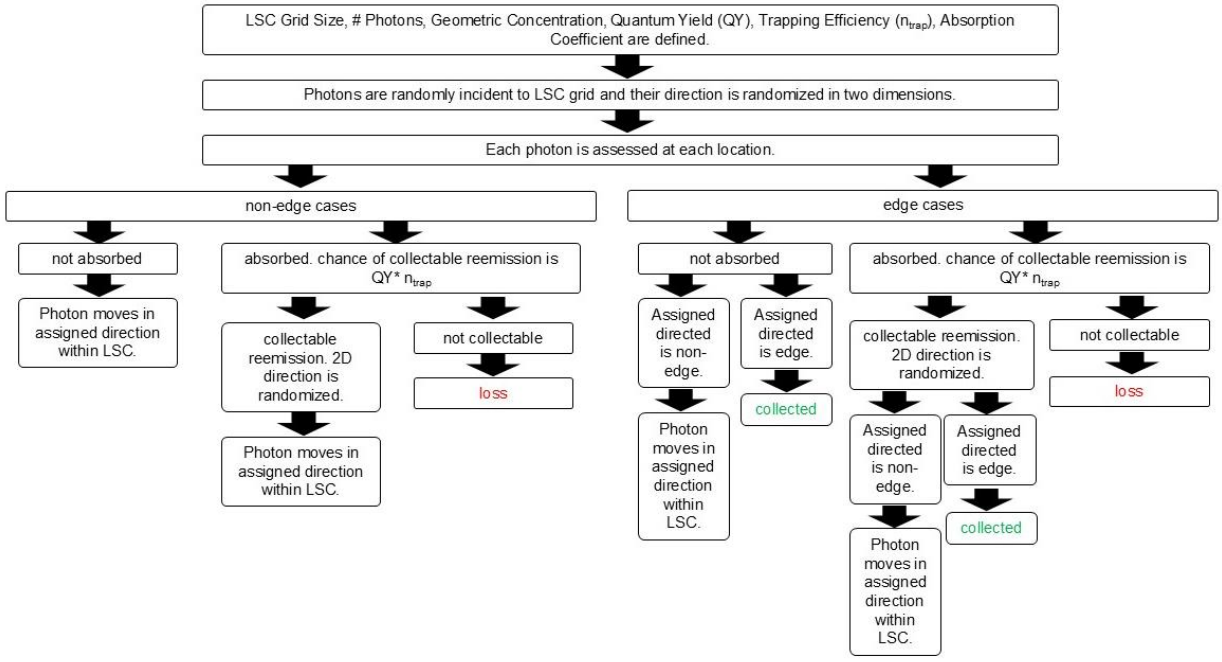

Figure 2.17. Monte Carlo simulation procedure

Once no photons remain inside the LSC (all either lost or collected), we calculate a collection efficiency n_{coll}, which is defined as

$$n_{coll} = \frac{photons\ collected}{incident\ photons} \tag{2.6}$$

Multiplying by geometric concentration gives an effective concentration for the LSC.

We report resulting effective concentrations for a photonic waveguide of varying geometric concentrations, quantum yields, and trapping efficiencies with a fixed luminophore absorption coefficient $\alpha = 0.01$ (Figure 2.18).

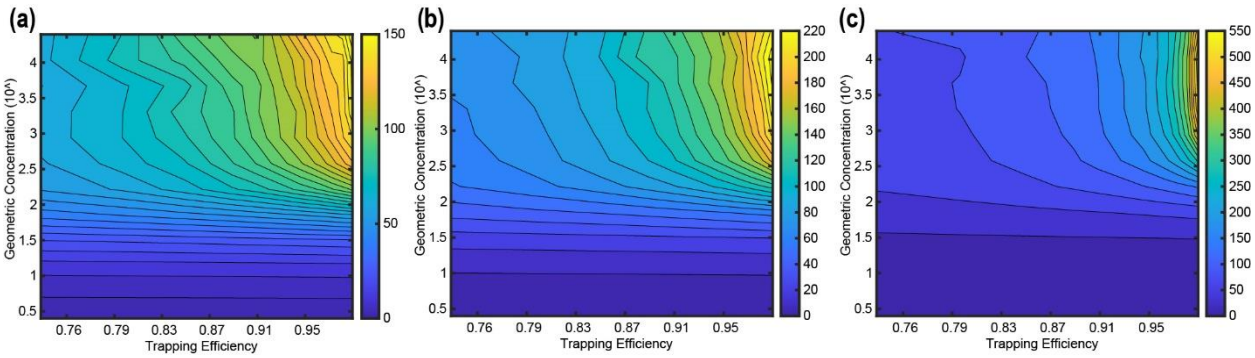

Figure 2.18. Effective concentration factor for a photonic waveguide with luminophore quantum yield of (a) 90% (b) 95% and (c) 99%.

This simulation demonstrates the dramatic loss in effective concentration that occurs for non-unity trapping efficiency and quantum yield, exaggerated further at very high geometric concentrations where losses are compounded. Achieving a concentration of 500x using a luminophore embedded LSC would require >99.9% trapping efficiency even with a >99% luminophore quantum yield. Our results suggest that with a very high performing but realistic[3] luminophore (>90% quantum yield), and excellent yet realistic[13] trapping (90%), a 100x concentration may be obtained. This motivates further studies to engineer improved trapping efficiencies in such devices by advanced mechanisms such as anisotropically emitting luminophores and photonic crystals (Chapters III and IV).

g. Conclusions and outlook

For waveguiding devices, the path towards highly efficient conversion and highly concentrating devices lies in delivering near-perfect trapping efficiency. As we have demonstrated here, these efficiencies can be facilitated by aligned anisotropic luminophores. Semiconductor nanoparticles are an excellent luminophore candidate for solar applications because of their capacity for directivity and color management.

Success of such a device and the success of a new generation of transparent optics is contingent upon consideration for waveguiding properties as well as photonic properties of our absorbers.[111] Such LSC

designs must take advantage of luminophores' (semiconductor nanoparticles) ability to absorb and directionally emit photons. This model motivates the following chapters, which elaborate the fundamental and tunable ability of LHP nanocrystals to selectively emit across a range of angles as a function of dipole orientation factor (Θ=0.78 to Θ=0.47).[112,113] With this control, photon management and spectrum splitting technology is possible.

III. TUNABLE ANGULAR LIGHT EMISSION OF LEAD HALIDE PEROVSKITE NANOCRYSTAL THIN FILMS VIA SOLUTION-PROCESSED SUBSTRATE TREATMENT

Abstract

Lead halide perovskite (LHP) nanocrystals have demonstrated a significant electronic response to their local environment due to their ionic lattice nature. Here, we demonstrated their tunable dipole alignment via solution-processed methods. We synthesized LHP nanocubes and nanoplates in air and characterized them by UV-vis spectrophotometry and Transmission Electron Microscopy. Using Atomic Force Microscopy, UV-vis spectrophotometry, and Back Focal Plane Fluorescence Microscopy, we characterized thin films of nanocubes on untreated glass, nano-roughened glass, and polymer film (polymethyl methacrylate, PMMA), as well as a perovskite nanocubes-nanoplate binary film on etched glass. Most notably, the dipole orientation factor can be modulated from 0.47 to 0.59 (effective transition dipole moment angle from 47° to 40°) by using glass or PMMA, respectively. Understanding the tunable anisotropic transitions in these materials at the nanoscale is required to control light emission into specific modes, which will maximize efficiency in devices like LEDs, photovoltaics, and quantum information technology.

a. Background

The alignment and relative strength of emissive states determines the emission angle of light, characteristic energy transfer, and the ultimate efficiency of any optoelectronic device.[14,66,114] Either films of randomly oriented emitters or of unconfined, isotropic nanoparticles are generally expected to yield an isotropic dipole orientation (Figure 3.1 (a)-(c)).[115] In most cases (i.e. organic dyes, chalcogenide nanoparticles), anisotropic dipole alignment—and therefore more exaggerated directional emission—is achieved through the alignment of confined or anisotropically shaped structures (Figure 3.1 (d)-(e)).[66,116] Recent work showed that the alignment of the electronic dipoles within films of unconfined perovskite nanocubes, which is expected to be isotropic, was tunable via changes to their local nanoscale environment through substrate modifications,[53,54] often showing a more exaggerated vertical dipole component and therefore more oblique light emission. This effect was exaggerated as surface coverage decreased: sparser films (particle assemblies <100 nm) showed even stronger vertical dipole components than their denser counterparts (Figure 3.1 (f)).[53] This trend was also observed in confined perovskite nanoplates, which showed a higher vertical dipole than expected.[22] Studies of this electronic surface effect on perovskite emitters are still limited, and the mechanism of this effect on their unique photophysics is not fully parsed. Further, films with nano-structuring or texturing of the emissive layer are of interest as this has been shown to improve light out-coupling efficiency.[8,117,118] Thus, understanding this interplay of dipole alignment and local environment will be key for maximizing optoelectronic device efficiency and accessing interesting photophysical behavior especially for future devices with ever-decreasing size footprints.[119–121]

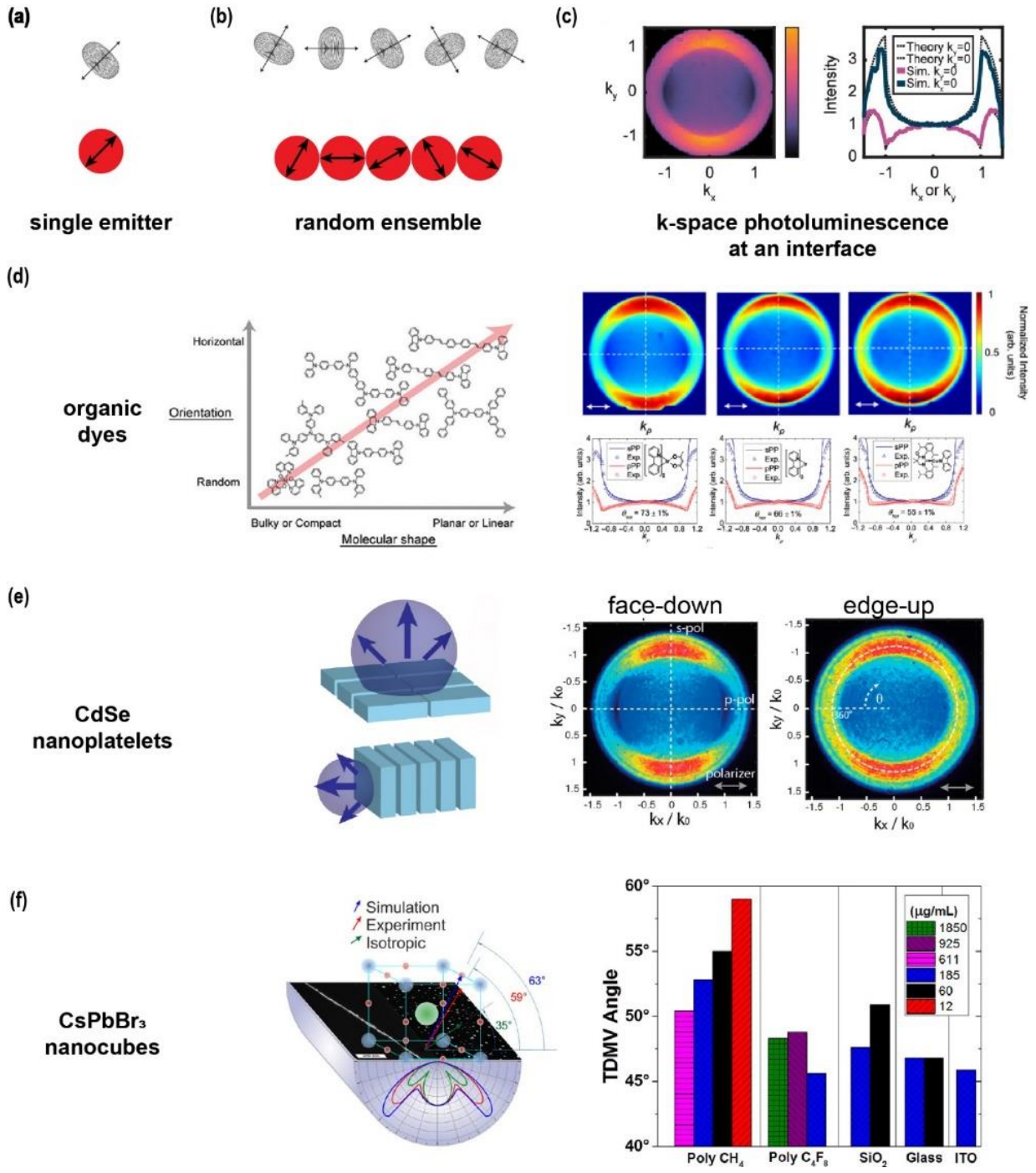

Figure 3.1. Prior Literature. (a) A single emitter shows preferential emission normal to the dipole. (b) A random ensemble shows isotropic emission. (c) Adapted from Russ et al.[72] Isotropic emission from a film of CdSe/ZnS quantum dots on glass. (d) (left) Adapted from Marcato et al.[122] Qualitative description of the result of molecular linearity on effective orientation (alignment) in organic dyes. (right) Adapted from Kim et al.[123] The effect of molecular orientation in organic dyes on k-space (angular) photoluminescence,

where more linear dyes correspond to more in-plane dipole strength. (e) Adapted from Gao et al.[66] Alignment of CdSe nanoplatelets results in all in-plane dipoles (face down) versus equal contributions of in-plane and out-of-plane dipoles (edge up). (f) Adapted from Jurow et al.[53] $CsPbBr_3$ perovskite nanocubes (isotropically shaped) show uniquely enhanced vertical dipole contribution (TDMV) as a function of substrate choice and film coverage.

Herein we quantify the unusual electronic anisotropy that nano-structured films of lead halide perovskite (LHP) nanocubes demonstrate in response to solution-processed substrate treatments. This demanded detailed characterization of nanocube films—to reliably extract the orientation of electronic dipoles from angular photon emission requires quantification of film thickness, quantification of particle packing assembly, and monodispersity. We investigated four substrates: untreated glass (*untreated*), nano-roughened glass (*etched*), insulating polymer film (*polymer-treated*), and perovskite nanoplate pre-deposition (*perovskite-treated*). After depositing films of LHP nanocubes on each film, we quantified their structural and optical properties by UV-vis spectrophotometry, Transmission Electron Microscopy (TEM), Atomic Force Microscopy (AFM), and Back Focal Plane Fluorescence Microscopy (BFPFM). We demonstrated that nano-roughening, which may increase surface interactions, ultimately had the same enhanced vertical dipole response as untreated glass. However, the presence of bluer nanoplates, which introduced energy transfer effects, showed slightly more in-plane dipole alignment, and depositing LHP nanocubes on a polymer substrate yielded near-isotropic dipole orientation even for these sparser films. We achieved a response by the effective transition dipole moment angle, which is determinant to the angular emission of light, thereby accessing advanced photophysical control via a facile benchtop process and expanding the library of materials to which perovskite nanoparticles uniquely respond.[22,53,54]

b. Optimization of ligand-controlled $CsPbBr_3$ perovskite nanocube synthesis for subsequent optical characterizations

Our first aim of the work was to generate morphologically pure, robust LHP nanocubes with narrow size distributions so that we could decouple the unique effect of substrate-induced emission anisotropy in these materials from the effects of particle anisotropy, polydispersity, or aggregation. LHP nanocubes were synthesized via modified ligand-assisted reprecipitation (mLARP) adapted from Brown et al.[124] Generally, cesium carbonate was complexed with octanoic acid to form cesium octanoate. Lead bromide was solubilized in toluene using trioctylphosphine oxide, and either octanoic acid or octyl phosphonic acid was introduced at 0 to 0.6 M concentration, by which the shape and size of the nanocrystals could be tuned. The cesium octanoate was injected in air at room temperature under constant stirring. Typically after 5 minutes, a solution of didecyldimethyl ammonium bromide in toluene was injected to quench the reaction. The colloidal product was cleaned and size-selected via centrifugation before further use. Because our study necessitated bright, uniformly sized particles, we focused on optimizing the size-selection and cleaning procedure as well as ligand selection and ligand concentration that delivered a bright, cubic morphology.

According to Brown et al.,[124] varying the concentration of the regulating ligand (octanoic acid (OctAc) and octylphosphonic acid (OPA)), allows for the tunable growth inhibition of particle size and therefore excitation wavelength. These ions bond to the surface of the nanocrystal during the reaction and give control over particle growth rate with changing surface density. Additionally, ligand ratio provides morphological control through a replacement reaction that occurs between cesium octanoate and octyl phosphonic acid. The use of octylphosphonic acid (OPA) strongly coordinates both the A and B cations, solubilizing $PbBr_2$ in toluene by complexing it with trioctylphosphine oxide (TOPO), and quenching nanocrystal growth using a bulky didecyldimethylammonium bromide (DDAB) ligand for the highly size-controlled formation of $CsPbBr_3$ nanocubes at room temperature. By further increasing the concentration of octylphosphonic acid, more Cs(OPA) is formed as opposed to Cs(OctAc). Due to the hydroxyl group in OPA, this complex hydrogen-bonds with trioctylphosphine oxide (TOPO) and increases ligand binding strength, leading to a reduced nanocrystal diameter and growth towards a truncated octahedron morphology.

$$Cs(OctAc) + OPA \leftrightarrow Cs(OPA) + OctAc \quad (3.1)$$

The reaction scheme is adapted as Figure 3.2 here to better visualize the multi-ligand system used. This stepwise ligand system allows the nucleation and growth phases to be uniquely decoupled by controlling precursor availability throughout the otherwise-rapid reaction. [17,19,125]

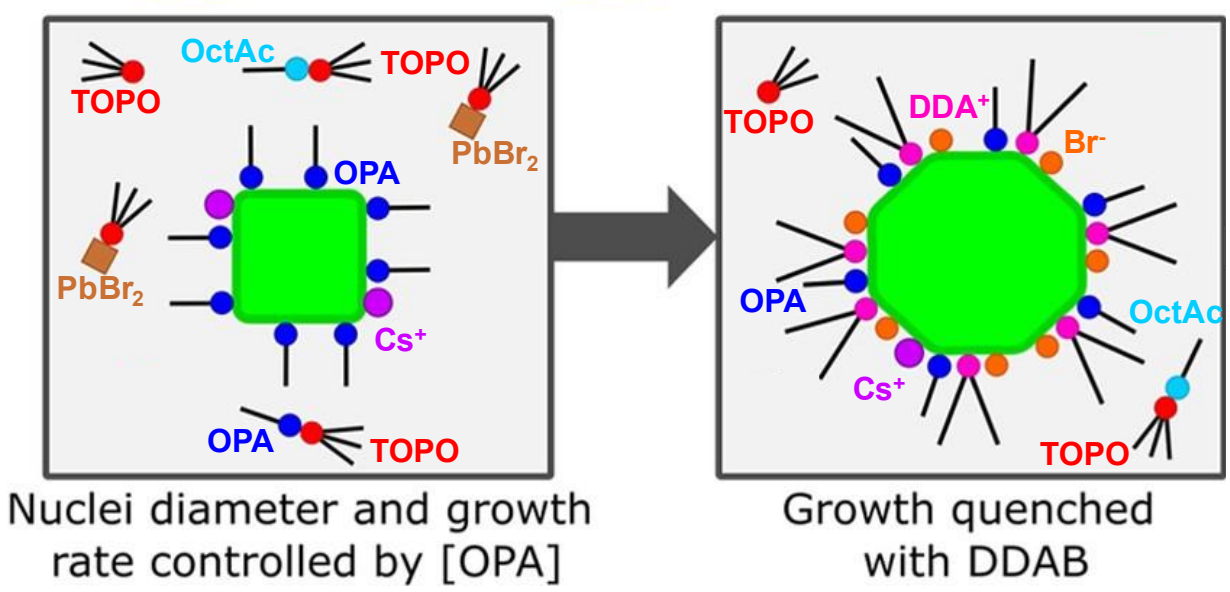

Figure 3.2. Reaction scheme for $CsPbBr_3$ nanocrystals adapted from Brown et al. [124] A system of multiple ligands works together to solubilize precursors (octanoic acid (OctAc), tricotylphosphine oxide (TOPO)), control precursor availability (TOPO, octylphosphonic acid (OPA)), and quench growth (didodecyldimethylammonium bromide (DDAB)) throughout the room temperature synthesis leading to monodisperse nanocrystals at room temperature.

We adapted this scheme for our purposes, employing OctAc/OPA and TOPO to regulate the availability of precursor ions during the reaction; the ability to modulate the growth phase made this an attractive approach. When the reaction was performed without OPA, OctAc concentration could be changed to achieve modest tunability of emission wavelength, which was reflective of nanocrystal size due to confinement effects. After synthesis, the particles were cleaned through a series of washing steps, where

the product was centrifuged in antisolvent (here, ethyl acetate or methyl acetate) and the precipitate was retained, then size selection steps, where the product was centrifuged in a favorable solvent (here, heptane) and the supernatant was retained. The goal of cleaning was to remove any unreacted or excess reagents as well as any aggregates and partially formed particles. However, after performing two cleanings as described by Brown, [124] the photoluminescence (PL) wavelengths of the syntheses converged, resulting in a diminished size tunability from changing ligand concentration (Figure 3.3). For 0 M, the center wavelength redshifts from 520 nm to 523 nm upon cleaning. For 0.3 M, the center wavelength redshifts from 514 nm to 522 nm, and for 0.6 M, the center wavelength redshifts from 511 nm to 520 nm.

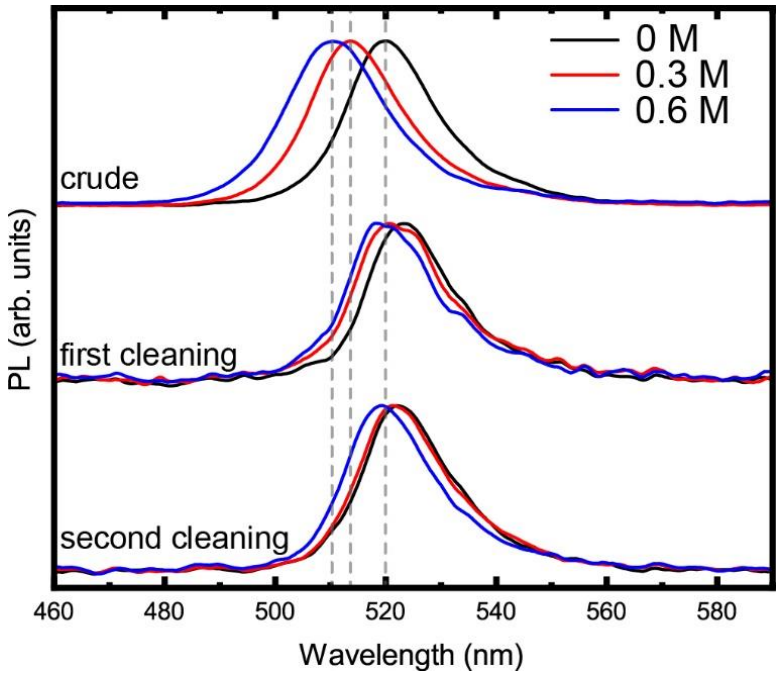

Figure 3.3. PL from $CsPbBr_3$ nanocubes synthesized under 0 M, 0.3 M, and 0.6 M OctAc. Each cleaning consists of a washing step and a size selection step. Both cleanings blur/diminish the ligand-induced size tunability.

To preserve size tunability achieved during synthesis, we modified the nanocrystal cleaning process such that the center wavelength of the emission was maintained in the final product. Since size distribution was controlled by the stepwise ligand system during synthesis, our cleaning attempted to preserve all

particles except large, aggregated particles or partially formed particles of a different morphology, which was observed by Brown et al.[124] We found that by performing one cleaning instead of two, and by carefully selecting the centrifugation time for size selection (30 s to 5 min), we observed preservation of the as-synthesized emission wavelength and no undesired alternative particle morphologies on TEM. Subsequently, one cleaning (antisolvent wash in methyl acetate and 60 second centrifugation in heptane for size selection) was performed. Figure 3.4 gives PL curves for our product at each stage of cleaning, demonstrating preservation of the desired emission wavelength throughout the washing process. For 0.6 M, the center wavelength redshifts only slightly, from 519 nm to 520 nm, and for 0.3 M, the center wavelength at 518 is maintained.

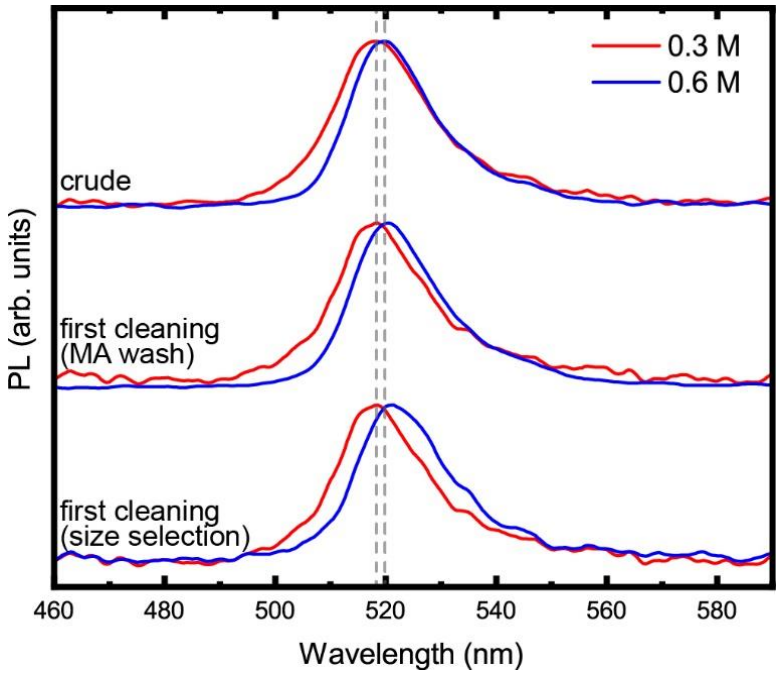

Figure 3.4. PL from $CsPbBr_3$ nanocubes synthesized under 0.3 M and 0.6 M OctAc. For one cleaning step instead of two, and for a 60 second centrifugation for size selection, the as-synthesized emission is maintained.

Finally, Brown et al.[124] reported a consistently higher photoluminescence quantum yield for particles synthesized using OPA as opposed to OctAc. Generally, OctAc led to the formation of cubes and

use of octyl phosphonic acid led to the formation of hexagonal to truncated octahedral particles (based on projection) due to steric effects and binding motif of OPA. For the same molar concentration (0.3 M), the enhanced ligand binding energy of OPA resulted in bluer hexagonal nanoparticles as opposed to OctAc-synthesized nanocubes, with emission at 517 nm versus 524 nm respectively. This difference of shape changed the packing, as shown by TEM, which for subsequent electronic characterizations, would change the effective refractive index and degree of electronic interaction between neighboring particles. Notably, corroborated by Brown, for an OPA concentration of 0.6 M, the nanoparticles maintained a cubic morphology as opposed to the hexagons or truncated octahedrons observed at lower OPA concentrations, and when the reaction time was shortened from 5 minutes to 30 seconds, we obtained small cubes with emission at 503 nm. Figure 3.5 (a)-(b) shows absorbance and photoluminescence of nanocrystals synthesized with octanoic acid, and confirmation of the expected cube morphology from TEM, while Figure 3.5 (c)-(d) shows absorbance and photoluminescence as well as TEM of nanocrystals synthesized with 0.3 M octyl phosphonic acid of hexagonal morphology. Figure 3.5 (e)-(f) shows absorbance and photoluminescence as well as TEM of nanocrystals synthesized with 0.6 M octyl phosphonic acid of cubic morphology (30 second reaction time). Figure 3.5 (e) shows photoluminescence tunability for many concentrations of OPA. The overwhelming trend is that increasing OPA allows us to tune for smaller particles with higher energy photoluminescence (from 524 nm to 511 nm) due to confinement effects. The 0.4 M and 0.2 M synthesis batches were redshifted and did not agree with the trend that increasing ligand concentration blue shifts photoluminescence. This error was attributed to potential contamination during reaction, as each synthesis was performed sequentially from each other.

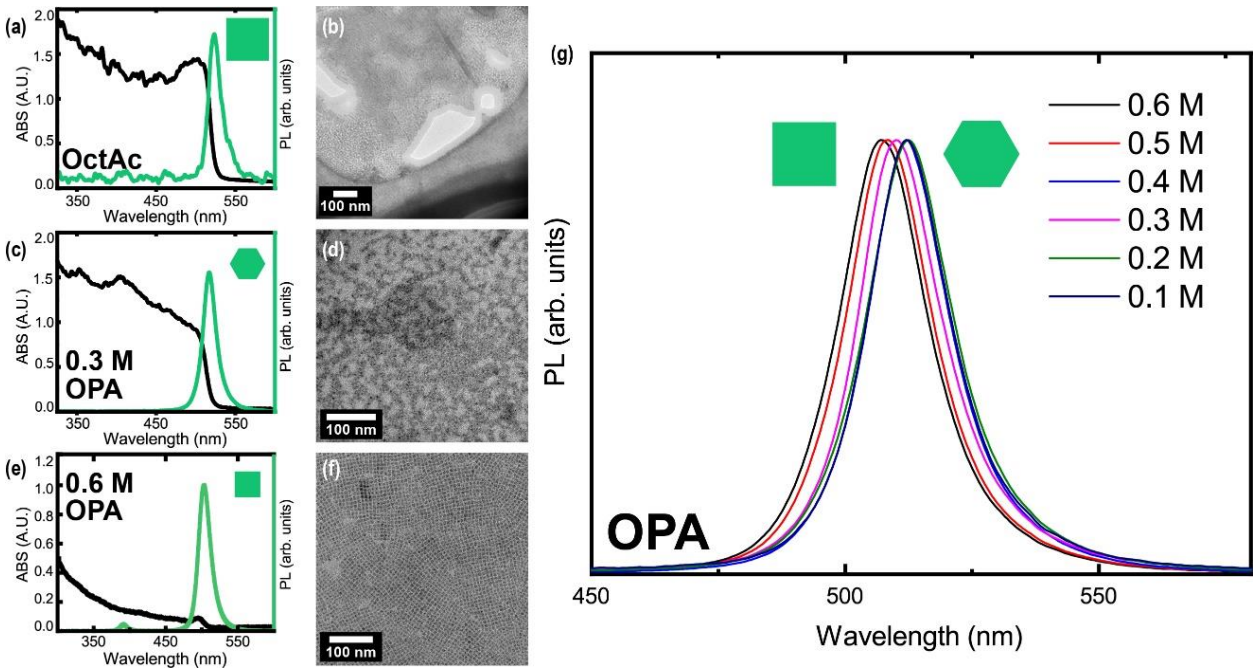

Figure 3.5. Absorbance and PL and TEM for $CsPbBr_3$ (a)-(b) nanocubes synthesized with 0.3 M OctAc. (c)-(d) hexagonal nanoparticles synthesized with 0.3 M OPA. (e)-(f) nanocubes synthesized with 0.6 M OPA for a shortened reaction time of 30 s. (e) PL showing OPA ligand-tunable spectral tunability, corresponding to smaller, bluer particles at high OPA concentrations.

This unique facile synthetic route offers robust $CsPbBr_3$ perovskite nanocrystals of comparable quality to those synthesized using other air-free hot injection methods that are more complex, but which have previously been the most reliable synthetic route to uniform, high quantum yield perovskite nanocrystals.[17,19] In addition to a facile synthesis method, we also achieved confinement-induced photoluminescence tunability of $CsPbBr_3$ nanocrystals by varying the concentration of ligand added—higher ligand concentration resulted in growth inhibition, yielding smaller, bluer particles. We identified a cleaning procedure that maintained PL tunability and selected synthetic parameters with the highest reported PLQY and cubic morphology (Table 3.1), resulting in an air-stable suspension of monodisperse $CsPbBr_3$ nanocubes.

Table 3.1. Recommended synthetic parameters for bright, monodisperse $CsPbBr_3$ nanocubes from Brown's synthesis[124]

	Result
Reaction time	30 s
Primary regulating ligand	0.6 M OPA
Resulting morphology	nanocube (7.4 nm)
Antisolvent wash	1x, 20 minutes at 10,000 rpm (12298 g), methyl acetate
Size selection	1x, 1 minute at 5000 rpm (3354 g)

c. Synthesis and characterization of colloidal perovskite nanocrystals for subsequent optical characterizations

Synthetic optimization of LHP nanocubes delivered the following procedure for robust, monodisperse particles suitable for fundamental electronic characterization studies using a modified ligand-assisted reprecipitation approach under ambient conditions.[124] In short, cesium carbonate was complexed with octanoic acid to form cesium octanoate and then injected into a lead bromide-octyl phosphonic acid precursor in air at room temperature under constant stirring. After 30 seconds, a solution of didecyldimethyl ammonium bromide in toluene was injected to quench the reaction. The colloidal product was cleaned and size-selected before further use according to the result of Chapter III.b. Optimization of ligand-controlled $CsPbBr_3$ perovskite nanocube synthesis for subsequent optical characterizations.

Since the confined nanoplates in this study would not be characterized for their fundamental electronics and instead simply provided an energetically-distinct environment in which to study LHP nanocubes, a facile synthesis of confined LHP nanoplates was adapted from Pan et al. without modification. [125] In short, via microemulsion approach, cesium bromide dissolved in hydrobromic acid was injected into a lead bromide solution in hexane containing N,N-dimethylformamide and an oleylamine-oleic acid ligand pair. Immediately upon injection the reaction was quenched by a small addition of ethanol. The crude

product was centrifuged and plate-containing supernatant was retained as product without further treatment. Further details of LHP nanoplate and nanocube synthesis are provided in Appendix B.

UV-vis spectrophotometry was used to characterize the absorbance and relative photoluminescence spectra of colloidal nanoparticles in solution (Figure 3.6 (a), (b)) and the relative photoluminescence of thin film samples (Figure 3.6 (c)). The deposition process for thin films is described in the following section. For nanocubes in suspension, the absorbance spectra showed a characteristic exciton peak at 495 nm and the photoluminescence spectra showed a narrow emission peak at 503 nm with a full width-half maximum (FWHM) of 20 nm. Nanoplates in suspension showed a blueshifted absorption exciton peak (450 nm) and emission peak (462 nm), indicating confinement. The nanoplate photoluminescence also had a larger red tail, indicating that some nanoplates fused into larger, thicker flakes.[126,127]

TEM was used to characterize the size and morphology of the nanocubes and nanoplates. Nanocubes were estimated to be around 7.4 nm in length. Nanoplates were estimated to be around 9.5 nm laterally and the larger flakes of fused particles were 100s of nm laterally. The small nanoplates are estimated to be 3 monolayers thick based on the emission wavelength.[19] Both populations of nanoplates had sufficiently blueshifted emission that could be distinguished and optically filtered from the nanocubes being studied.

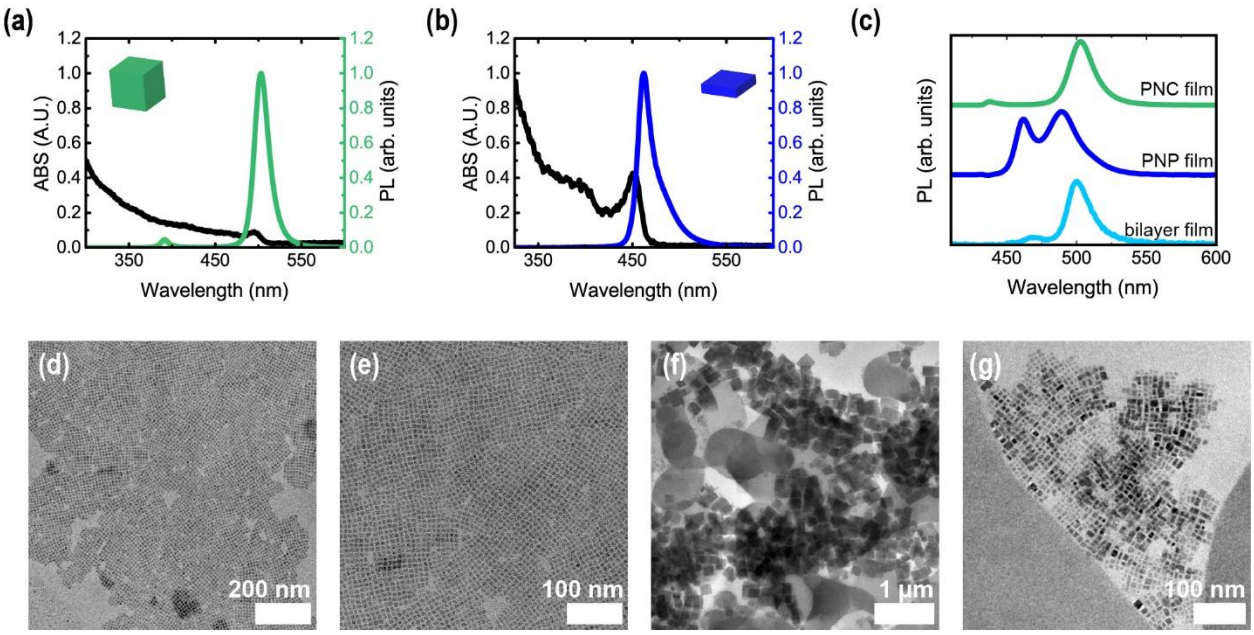

Figure 3.6. Absorbance and normalized relative photoluminescence spectra for colloidal suspension of (a) $CsPbBr_3$ nanocubes with emission at 503 nm and (b) $CsPbBr_3$ nanoplates with emission at 462 nm. (c) Relative photoluminescence spectra for thin films of $CsPbBr_3$ nanocubes (503 nm), nanoplates (462 nm and 489 nm due to plate fusing), and a bilayer of nanocubes and nanoplates (469 nm and 500 nm). The peak at 438 nm is a spectral artifact from the excitation light source. (d)-(e) Transmission electron micrographs of nanocubes (estimated length 7.4 nm) assembled in a monolayer. (f)-(g) Transmission electron micrographs of larger (100s nm long) fused populations and smaller (estimated length 9.5 nm, 3 monolayers thick) of nanoplates used as a spectrally-distinct emitter.

d. Fabrication of perovskite nanocrystal thin films

Thin films of LHP nanocubes were deposited by spin coating as-synthesized nanocube suspensions onto different substrates, creating four distinct environments: untreated borosilicate glass (*untreated*), nano-roughened borosilicate glass (*etched*), insulating polymer (*polymer-treated*), and a nanoplate pre-deposition (*perovskite-treated*). Untreated borosilicate glass was used to compare the behavior of $CsPbBr_3$ nanocubes to prior studies.[22,53] A caustic etch of potassium hydroxide in ethanol (pH 11-12) was used to treat the borosilicate glass and understand how roughening might also exaggerate electronic substrate interaction by

increasing surface area. We also investigated the use of an insulating polymer layer as the substrate. An approximately 40 nm-thick film of poly(methyl methacrylate) (PMMA) was deposited via spin coating. PMMA has a similar refractive index to borosilicate glass (1.49 vs. 1.51, respectively) and thus should only alter the local electronic environment and not the optical environment, allowing for a direct comparison between the glass and PMMA substrates. Finally, to elicit how Förster Resonant Energy Transfer (FRET) or more complex exciton transport schemes affected dipole orientation,[128,129] perovskite nanoplates were deposited via spin coating before depositing nanocubes to create a binary film. Because these nanoplates had the same composition as the nanocubes ($CsPbBr_3$) and the emitting layer thickness is much smaller than the wavelength of light, any changes in the photoluminescence spectra and angular emission resulted from the interactions from high energy (nanoplates) to low energy (nanocubes) components and not from optical or chemical changes (e.g. halide diffusion of mixed samples[130]).

There was no significant shift in the photoluminescence when the nanocrystals were deposited into thin films. Thin films of nanocubes alone showed an emission peak at 503 nm and thin films of the nanoplates alone showed an emission peak of 462 nm (Figure 3.6 (c)). However, the nanoplate film also showed a significant secondary PL peak at 489 nm (Figure 3.6 (c)), which was attributed to the fusing of plates. Finally, the perovskite-treated sample (binary population) showed two distinct emission peaks at 469 nm and at 500 nm, which aligned well with the peaks from the nanoplate and nanocube colloidal suspensions, respectively. For total relative PL, the nanocube signal intensity was more than five times greater than the nanoplate signal intensity. From this we concluded that the less intense nanoplate signal could be sufficiently cut out using a longpass filter, allowing us to isolate and study the angular signal of the nanocubes only.

We characterized the conformality and thickness of nanocube films on each substrate and substrate roughness using Atomic Force Microscopy (AFM). To determine the thickness of the nanocube layer from the three conditions where nanocubes were not on top of nanoplates, the image was plane-leveled, row-aligned, and masked via height threshold to isolate the islands of nanocubes from the background. Masks are shown in Figure 3.7. The average height of the masked region was subtracted from the average height

of the background. The same was done for the perovskite-treated samples, shown in Figure 3.8. While the two species are indistinguishable using AFM, both populations were resolved using both large-area relative photoluminescence (Figure 3.6 (c)) and spatial photoluminescence at 100x magnification (Figure 3.9).

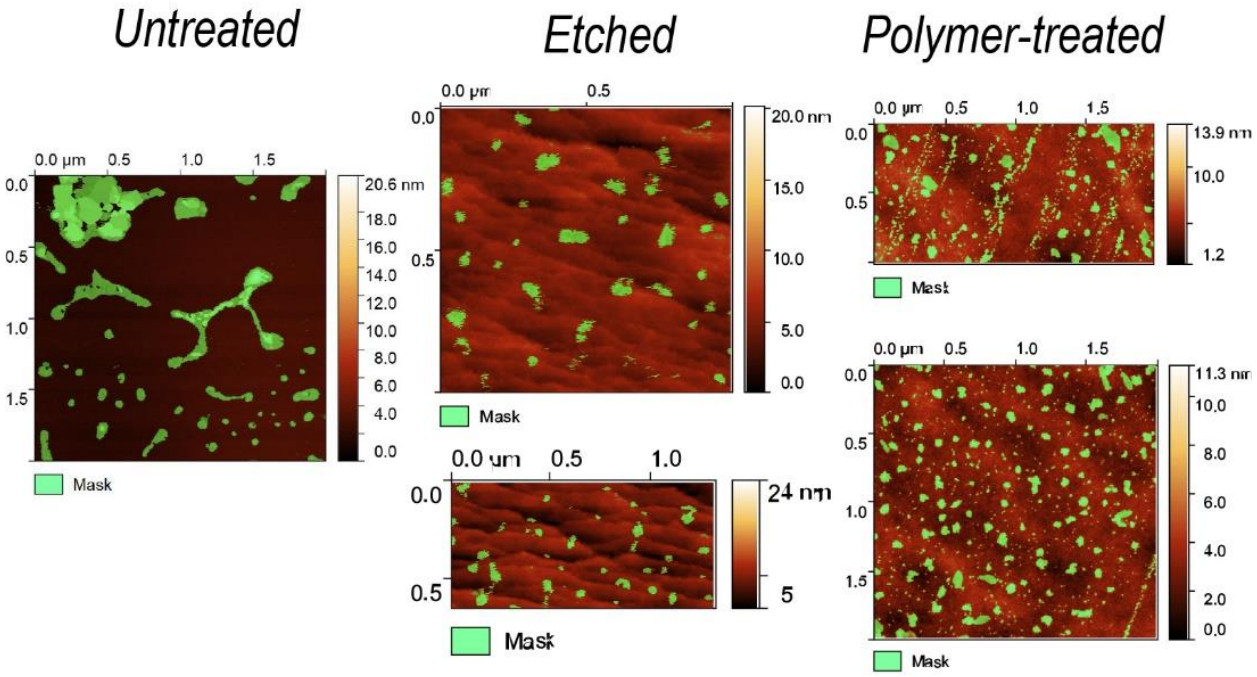

Figure 3.7. AFM images with height mask denoted in green from which an average thickness of 6.0 nm was extracted.

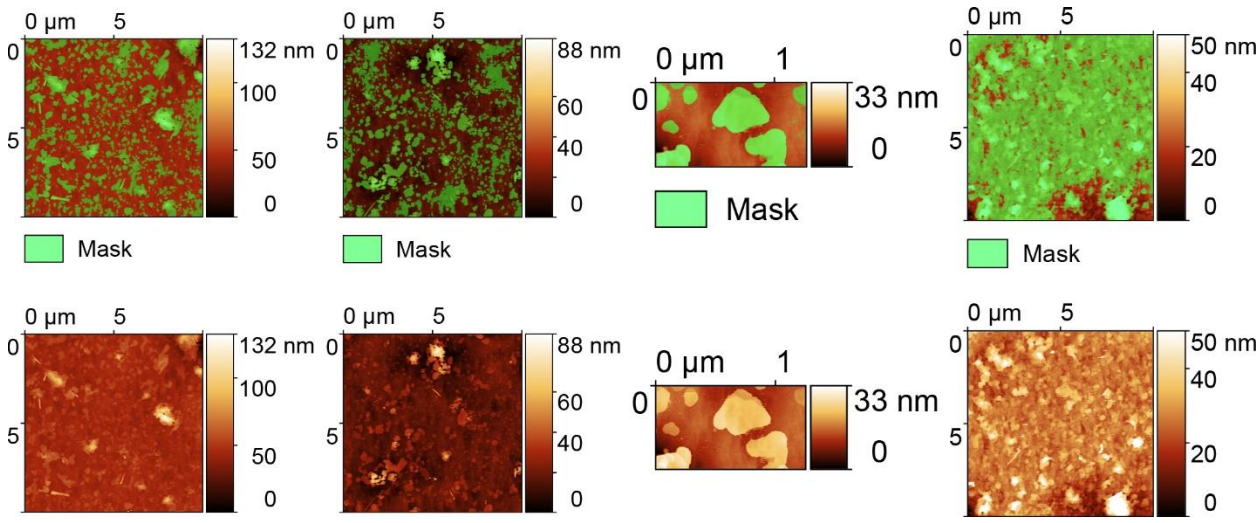

Figure 3.8. AFM image of perovskite-treated sample from which an average thickness of 10.3 nm was extracted.

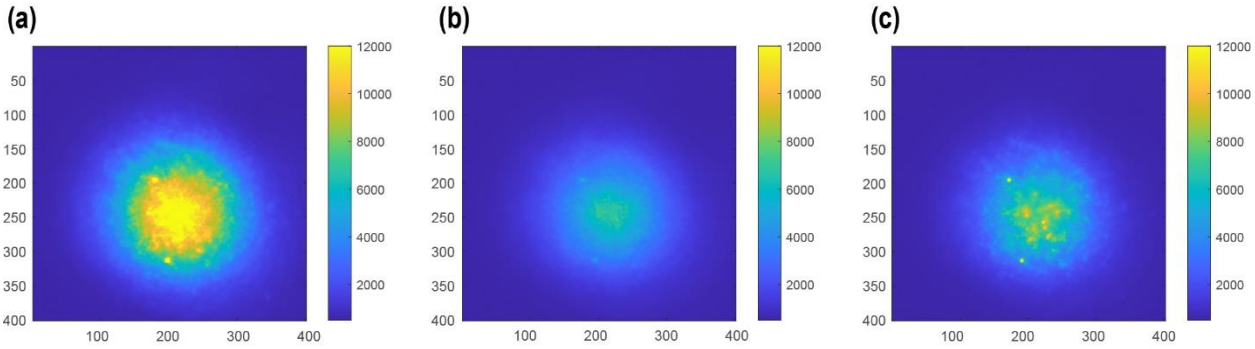

Figure 3.9. Using widefield excitation at 405 nm, a. total PL signal from perovskite-treated film b. PL signal from nanocubes (emission 500-503 nm) isolated using a 500 nm longpass filter c. PL signal from nanoplates (emission 462-489 nm) isolated using a 500 nm shortpass filter

Figure 3.10 shows the thickness variation over a representative area (2x2 µm) as well as a representative thickness profile of the nanocubes on each substrate. Reported fractional nanocrystal coverage was approximated using 10x10 µm AFM images from each sample condition and background RMS roughness was approximated using 10x10 µm AFM images of the substrate conditions alone (Figure 3.11 and Table 3.2). Perovskite-treated substrates were treated with a heptane rinse to simulate any rinsing

effects that occur during nanocube deposition. For all nanocube-only cases, the nanocube island thickness thickness was estimated to be 4-8 nm (average 6.0 nm) which agreed reasonably well with the particle size of 7.4 nm estimated from TEM. The nanocubes-only substrates showed similar total coverage of monolayer groupings or "islands" of nanocrystals but islands of nanocubes were larger and more irregular across the untreated wafer (Figure 3.10 (a)) as opposed to films on etched or polymer-treated wafers (Figure 3.10 (b), (c)). The perovskite-treated sample formed slightly thicker islands on average (10.3 nm). Additionally, we confirmed that the etched substrate had a larger roughness than the untreated substrate (Root Mean Square roughness of 3.50 nm and 0.76 nm, respectively). The polymer-treated substrate had an RMS roughness of 1.56 nm (Figure 3.11). The nanocube-nanoplate binary film shows a higher total coverage of nanocrystals than the other three substrates, around 34% versus around 15% for cubes only samples.

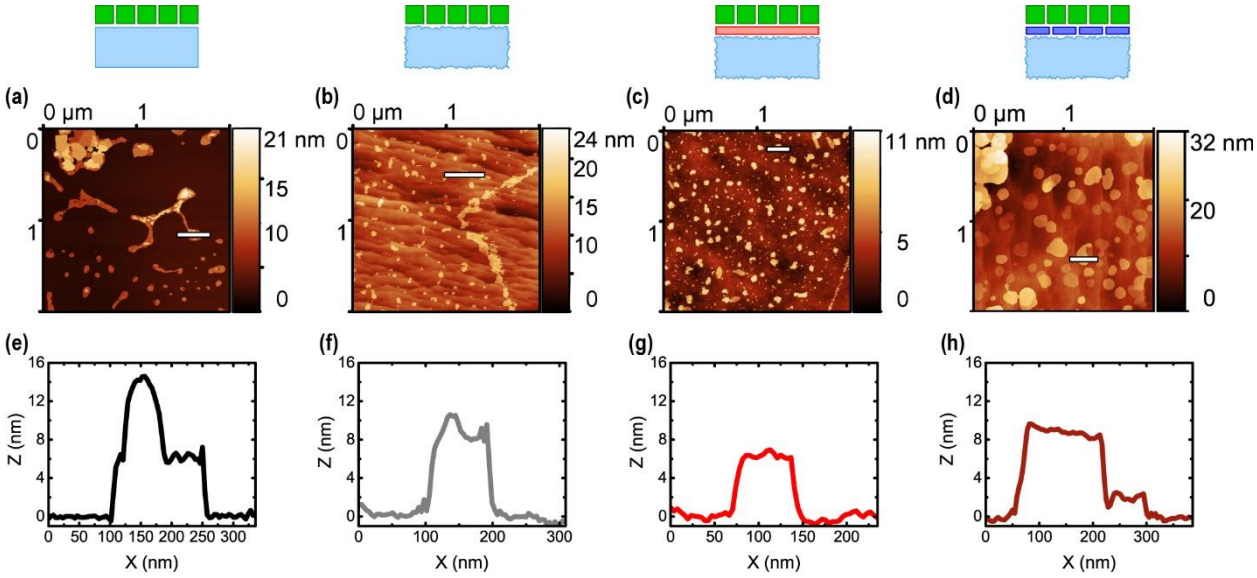

Figure 3.10. Atomic force micrographs of $CsPbBr_3$ nanocube thin films fabricated via spin coating onto a silicon wafer that was (a) untreated, (b) etched, (c) polymer-treated with 40 nm-thick PMMA, and (d) perovskite-treated with spectrally-distinct $CsPbBr_3$ nanoplates. Islands of nanocubes assembled in a monolayer were present in each sample, and the untreated silicon had an irregular distribution as compared to the other nanocube-only samples. The average height of these islands across nanocube-only samples was 6.0 nm. The average height of nanocubes and nanoplates together was 10.3 nm. Illustrative extracted cross sections (background normalized to 0 nm) showing height profiles corresponding to nanocubes on (e) untreated, (f) etched, (g) polymer-treated, and (h) perovskite-treated wafers. The white line in each scan (a)-(d) shows where cross section was extracted.

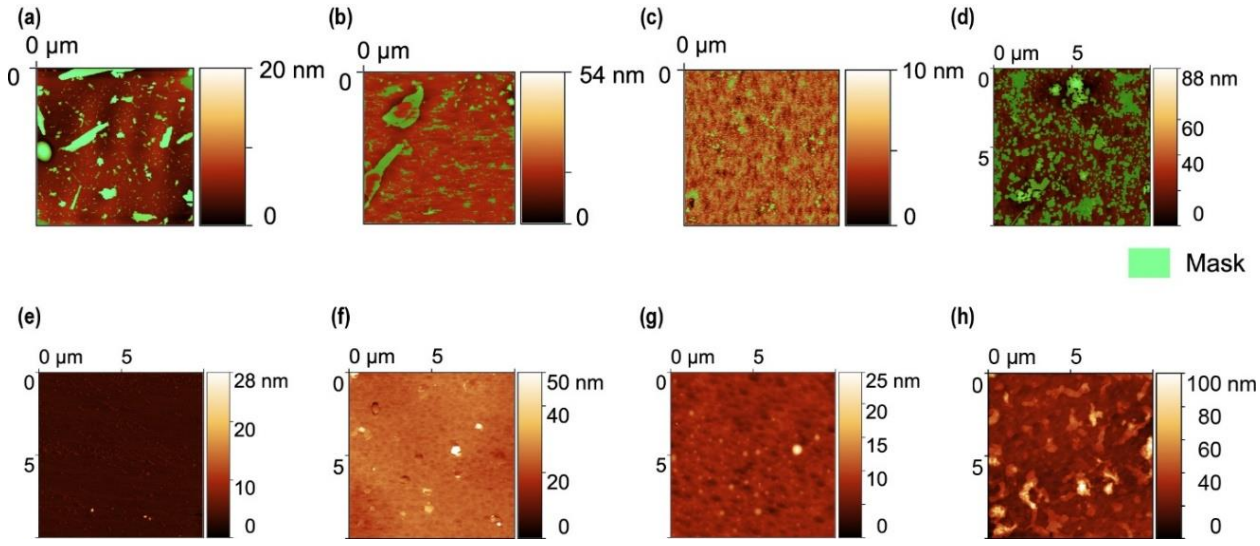

Figure 3.11. AFM images of a. untreated, b. etched, c. polymer-treated, and d. perovskite-treated samples from which nanocrystal coverage was extracted and of e. untreated, f. etched, g. polymer-treated, and h. perovskite-treated substrates alone from which RMS roughness was extracted.

Previous work proposed that substrate polarity might be the mechanism that induces electronic anisotropy in LHP nanocrystals at an interface.[54] We wanted to quantify the relative surface polarity in order to decouple this effect from other proposed mechanisms. Contact angles of water on each glass substrate were averaged from ≥50 measurements using an FTÅ125 goniometer (Table 3.2). For perovskite-treated substrate, water contact angle could not be accurately reported because LHP nanocrystals are soluble in water. We observed no relationship between contact angle (surface polarity) and the resultant dipole orientation of the emissive films reported in the following section.

Table 3.2. Substrate Properties

	Contact angle (θ_{water}) on glass	approx. fractional nanocrystal coverage	Substrate RMS Roughness (nm)
untreated	59±2	0.15	0.76
etched	40±3	0.15	3.50
polymer-treated	64±1	0.14	1.56
perovskite-treated	--	0.34	11.29

e. Quantifying angular light emission

We resolved the angular emission pattern of each sample using Back Focal Plane Fluorescence Microscopy (BFPFM), also known as Fourier Plane imaging.[68] The focal plane in a traditional imaging microscope was transformed from the sample plane to the Back Focal Plane by inserting an additional lens (Bertrand lens) between the microscope objective and the tube lens.[68]

The Back Focal Plane shows a 2D projection of the angular emission pattern (Figure 3.12).[70,71] We performed BFPFM using a home-built inverted microscope with excitation by a 405 nm continuous wave laser and a 100x oil immersion objective. A linear polarizer allowed us to study the p-polarized angular emission. Longpass filters were used to isolate the nanocube photoluminescence, removing any background laser or nanoplate emission. Further details of BFPFM can be found in Chapter I.e. Key metrology.

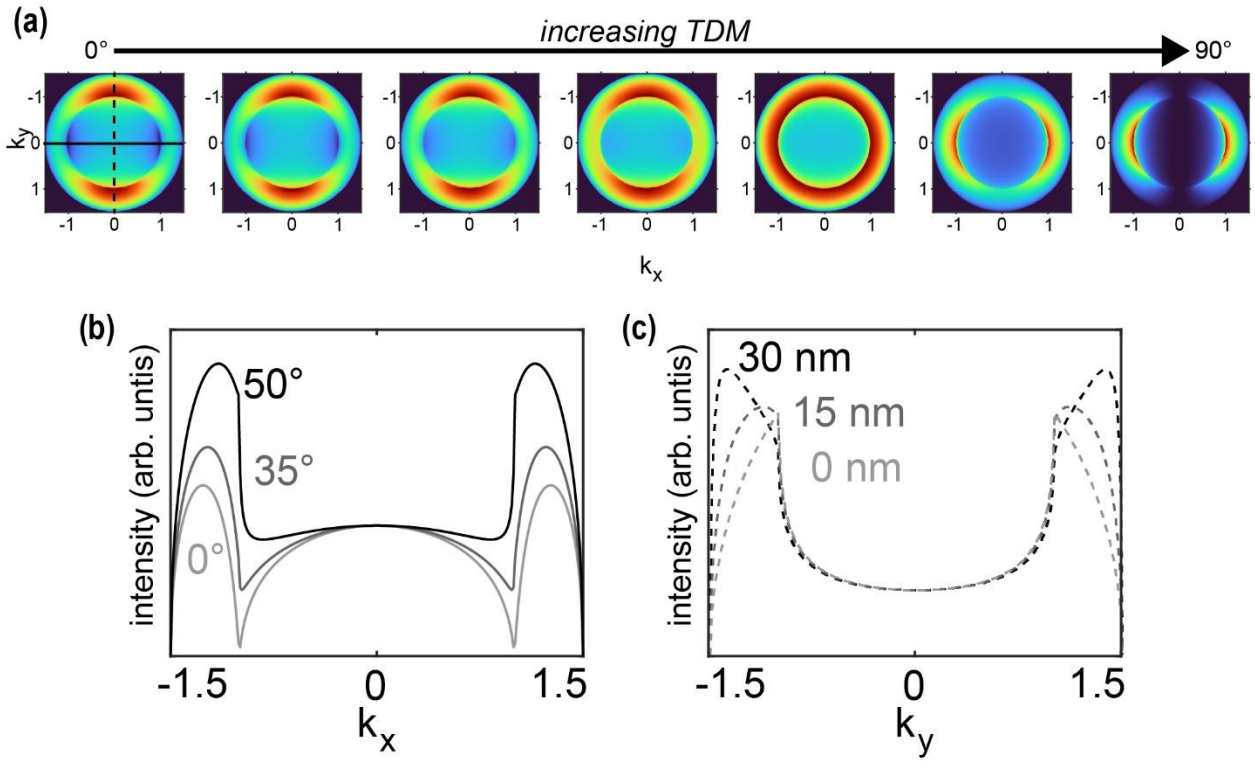

Figure 3.12. (a) Modeled BFPFM signal for a thin film of known effective transition dipole moment of 0° to 90°. Momentum space cross-sections show how TDM changes the signal along k_x, and how emitting layer thickness changes the signal along k_y.

In brief, the horizontal and vertical dipole contributions from a sample were determined by fitting the average collected emission pattern across 25 images to a simple three-layer analytical model which determines the angular emission pattern resulting from a thin emissive film on a substrate (here, glass) surrounded by air.[22,66,70–72] Orientation factor (Θ) was defined as the relative strength of in-plane dipoles to all dipoles, according to the convention given by Kim et al. [69]

$$\Theta = \frac{p_{\parallel}}{p_{\parallel}+p_{\perp}} \tag{3.2}$$

where p is relative dipole strength of the parallel and perpendicular dipoles. An effective transition dipole moment for the system as described in [64] can be defined as

$$TDM = arccos(\sqrt{\Theta}) \tag{3.3}$$

for the convention where TDM is the angle measured between the substrate and the vector of the transition. The following general equation describes the polarized light emission intensity projected onto a 2D collection plane (N_{pol}) as a function of photon momentum vectors along the x- and y-directions (k_x, k_y):[22,67]

$$N^{pol}(k_x, k_y) = C\left[\frac{1}{2}\left(\rho_{IP}^{p} + \rho_{IP}^{s}\right)\cos^2(TDM) \ + \rho_{OP}^{p}\sin^2(TDM)\right] \tag{3.4}$$

where C is a normalization constant arising from the integration time of the collection media and excitation intensity, ρ_{ip}^{s} and ρ_{ip}^{p} are the density of states of s- and p-polarized in-plane dipole contributions, and ρ_{op}^{p} is the out-of-plane dipole contribution Recall that the density of states is a function of the photoluminescence wavelength, the refractive indices of the three layers, and the thickness of the emissive layer. When modeling density of states for our samples, we used a wavelength of 503 nm (peak photoluminescence of the nanocube films), a refractive index of 1.92 (estimated from TEM using an effective medium approximation[22,53]), and a thickness of 0 nm, which is an accepted approximation for sub-monolayers of nanocrystals, or when thickness is much smaller than the wavelength of light.[53,66] See Supplemental Information for further details.

From TEM, an effective medium approximation gives an RI of 1.92 (similar to the RI of 2 used for close-packed nanoplates in prior literature [22]). An average thickness of 6.0 nm is extracted from AFM data, and we fit our angular emission data to a modeled film of thickness 0 nm (Frensel reflections are modeled, but negligible phase change was assumed: 6.0 nm << λ). We calculate the variances by collecting multiple ($N \geq 5$) datasets under identical conditions.

Background signal noise across datasets had a standard deviation of 1.25% which results in an associated inherent uncertainty of fit. Using Monte Carlo simulations over 500 iterations according to the procedure described in Russ et al., [72] the inherent uncertainty in the fit of our measurements given the

thickness and RI of the emitting layer standard deviation of background noise levels is ±0.01°. The p-values from two-tailed Student's t-tests for two independent samples, the etched versus untreated fits were not statistically different. The etched versus polymer-treated and etched versus perovskite-treated fits were statistically different (p-value = 7.54e-07 and p-value = 0.00015, respectively).

Because we investigated fluorescence from the same nanocrystals across substrates with nearly similar outcoupling behavior, the density of states ($\rho_{ip}^{s}, \rho_{ip}^{p}, \rho_{op}^{p}$) remained the same across all substrates. Thus, any change in the angular emission pattern arose from changes in only the effective dipole orientation. Figure 3.12 (a)-(b) models how the projected Back Focal Plane evolves as effective TDM, or dipole alignment, changes. This is shown clearly in the p-polarized cross section (k_y=0), or the cross-section taken across the center of the image.[64] When there are only horizontal dipoles present (TDM=0°, Θ=1), the p-polarized k-space axis (k_x) decreases sharply to 0 at $|k_x|$=1. As the vertical dipole strength increases (TDM > 0°, Θ<1), the signal increases for $|k_x| \geq 1$. When all dipoles are vertical (TDM=90°, Θ=0), the p-polarized axis shows instead an abrupt increase in photoluminescence intensity at $|k_x|$=1. A TDM of 35° (Θ=0.67) is expected for samples with isotropic dipole contributions (two horizontal dipoles and one vertical dipole), which can be seen in either unconfined, isotropically shaped nanostructures or randomly oriented assemblies of particles or dyes, such as CdSe quantum dots.[65] Note that the s-polarized cross section (kx = 0) does *not* change with dipole alignment, and is only a function of wavelength, thickness, and refractive index of the emitting layer (Figure 3.12 (c)). We verified that all four substrates have identical optical environments by plotting the s-polarized cross sections. For the four cases investigated here, the momentum space s-polarized cross section k_y remains consistent, indicating consistency across cases for the RI and thickness of the emitting layer, shown in Figure 3.13. Therefore, any changes in the Back Focal Plane image between different substrates are purely a function of the changing dipole alignment of the system.

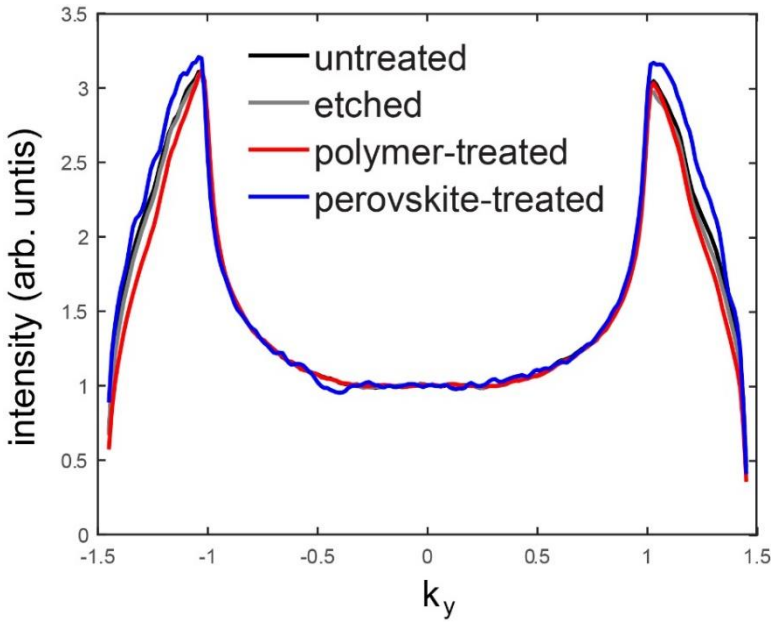

Figure 3.13. s-polarized cross section of BFPFM signal for $CsPbBr_3$ nanocube films on untreated, etched, polymer-treated, and perovskite-treated substrates.

Figure 3.14 (a)-(d) (lefthand column) shows the experimental BFPFM images of perovskite nanocube thin films on substrates of untreated glass, etched glass, polymer-treated glass, and perovskite-treated glass. Additionally, the extracted k_x cross section is shown in Figure 3.14 (e) to highlight the response to each substrate. The shading around each cross section shows one standard deviation from the average. The untreated and etched samples showed overlapping k_x cross sections, demonstrating the same dipole orientations. However, both the polymer-coated glass and the perovskite binary film showed a reduced signal at $|k_x| \geq 1$ outside of the variance of the previous samples, demonstrating a more horizontal dipole alignment compared to the other treatments. The polymer-treated sample had a much stronger decrease, indicating the most horizontal alignment.

We then fit each BFPFM image to the theory in Equation 3.4 to quantify the orientation of the dipoles as the effective transition dipole moment angle (TDM) and the orientation factor (Θ) for these four substrates. The best fit to the theoretical angular emission pattern is shown in the righthand column of Figure 3.14 (a)-(d). An isotropic dipole alignment (TDM=35°, Θ=0.67) would be expected in the case of

no structural or confinement anisotropy in the emitting film. However, as shown in Figure 3.14 (f), perovskite nanocrystals have shown an enhanced vertical dipole component for most surface treatments studied in prior work,[22,53,54] and for sparse films in particular.[53] This effect is likely due to charge redistribution in response to the substrate.[22,131] When two dissimilar materials are brought into contact, charge is generated due to work function mismatch. The work function mismatch between glass (5.0 eV)[22] and perovskite (4.0 eV)[132] creates interfacial charge and, because of the ionic nature of the perovskite lattice, charges redistribute within the perovskite near the surface, generating a more exaggerated vertical electronic dipole that is not seen in traditional semiconductor nanocrystals with more covalent lattices.[133] Additionally, it is theorized that this redistribution is even stronger for isolated groups of particles, and indeed more vertically oriented dipoles have been observed for sparser films.[53]

The untreated glass substrate in our study fit to a TDM of 47±1° and orientation factor Θ=0.47, also showing an enhanced vertical dipole component. This corroborated prior work from Jurow et al. who showed that a similar density of nanocubes on a glass substrate had a TDM of around 46.8°.[53] We hypothesized that the nano-roughening of glass might further influence the dipole alignment by increasing the surface area and thus the generation of interfacial charge. While the roughening did improve the film uniformity as shown by AFM, this treatment was shown to have no effect on the dipole alignment, yielding a TDM of 46±1° and orientation factor Θ=0.48, statistically the same as the untreated glass substrate.

As shown by the k_x cross sections, nanocubes on a PMMA substrate had a greater fraction of horizontal dipole contributions than the glass substrates. This led to a lower effective TDM angle (40±1°, Θ=0.59) that approached isotropic dipole behavior (TDM=35°, Θ=0.67); this change in orientation was statistically significant as compared to the etched treatment (p-value = 7.54e-07). Notably, this polymer-treated substrate achieved the same nearly-isotropic behavior as more densely packed films from prior studies (Figure 3.14 (f)), which is surprising given that sparse films tend towards more vertical dipole alignments.[54] PMMA did not show a significantly increased contact angle with water over untreated glass (θ_{water}=63±7° versus θ_{water}=59±2°), indicating similar substrate polarity. Instead, our hypothesis for this TDM effect builds on intuition established by Jurow et al.[22] The work function difference between PMMA

(4.68 eV)[134] and perovskite (4.0 eV)[132] is smaller than glass (5.0 eV)[22] and perovskite, and as a result, the polymer-treated substrate is expected to have fewer interfacial charges and therefore less charge redistribution. Our observations indicate that having a thin layer of PMMA is sufficient to reduce the vertical dipole strength by over 20%, bringing these nano-structured films much closer to their expected dipole alignment.

As a precursor to more extensive studies on the relationship of FRET and TDM, we studied nanocubes in the presence of nanoplates. Interestingly, as in other on-glass films, a vertically asymmetric TDM was again observed, though less than the untreated- and etched-substrates. After spectrally isolating the nanocube signal, the angular emission patterns fit to a TDM of 44±1° and orientation factor Θ=0.52. The extracted orientation for the binary film on an etched substrate was statistically different than the nanocubes alone on an etched substrate (p-value = 0.00015). While dipole-mediated energy transfer is a well-studied effect,[128,129,135] we note the effect of energy transfer on the TDM of perovskite nanocubes could not be decoupled from the effects of increasing film coverage (15% to 34%) in this study.[53,54] Further, charge generated at the nearby glass interface is highly relevant to exciton behavior in both the perovskite nanocubes and nanoplates. We note the work function of $CsPbBr_3$ increases with confinement, so work function mismatch of the different populations of nanoplates could contribute to this effect.[61] Further studies should continue to investigate the mechanism of the unique optoelectronic response of $CsPbBr_3$ nanocubes in a binary film.

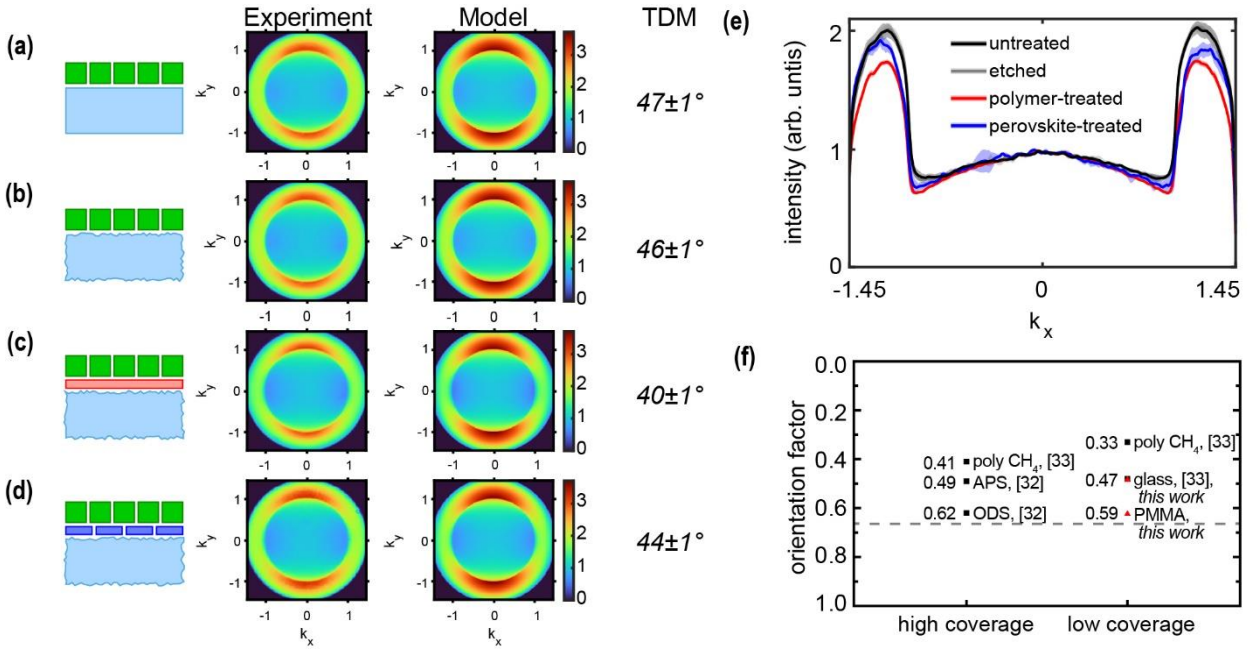

Figure 3.14. Experimental BFPFM signal, best fit BFPFM model and effective TDM for each substrate: (a) untreated (TDM=47±1°), (b) etched (TDM=46±1°), (c) polymer-treated (TDM=40±1°), and (d) perovskite-treated (TDM=44±1°) (e) Extracted k_x cross sections for emission on each substrate. Shading indicates one standard deviation from the average k_x cross section. (f) Orientation factors for LHP nanocubes on a given substrate in literature as compared to this work for high and low coverage films. Dashed line indicates isotropic dipole orientation.

f. Conclusions and outlook

We showed the angular photoluminescence response of LHP nanocrystal thin films to changes in the local electronic environment through substrate modifications. LHP nanocubes were synthesized via in-air methods and deposited via spin coating onto four substrates that changed the electronic environment while maintaining a comparable optical environment. We compared untreated glass, nano-roughened glass, a thin insulating polymer film, and a distinctly-emitting nanoplate treatment. We used Back Focal Plane Fluorescence Microscopy, which provided a 2D spatial projection of the 3D angular emission signal, to quantify the effects of the substrate on light emission. We fit resulting emission patterns to a photonic density of states model and extracted the effective transition dipole moment (TDM) orientations. Nano-

structured films of nanocubes on untreated borosilicate glass, nano-roughened glass, or in the presence of confined nanoplates exhibited an enhanced vertical dipole component (TDM=44-47±1°, Θ=0.52-0.47), while nanocubes on a PMMA substrate showed nearly isotropic dipole alignment (TDM=40±1°, Θ=0.59).

Generally, films of randomly oriented particles are expected to behave as isotropic emitters at an interface (TDM=35°, Θ=0.67). However, by leveraging this unique electronic response of perovskite nanocrystals to their local environment,[22] we can tune the emission mode directly to the desired application, allowing improved external quantum efficiency and energy transfer in solar concentrators or LEDs.[73,114,136] Specificity of emission mode may also enable enhanced coherence for quantum information technologies, for which perovskite nanocrystals are already a promising candidate.[31,52,137] This work demonstrates that perovskite nanocrystals can access tunable photophysics via facile benchtop processes, opening the door to a greater suite of quantum and new-wave semiconductor research by reducing the processing expense of such materials systems. However, the large amount of aggregation and non-conformality that is observed particularly in nanoplate films (RMS roughness >10 nm) motivates further studies of advanced solution-based deposition methods to achieve better film uniformity than is possible with typical solution-processing methods like spin coating.

IV. ORIENTED DIPOLES IN ORDERED ENSEMBLES OF CONFINED LEAD HALIDE PEROVSKITE NANOCRYSTALS

Abstract

Here, we demonstrated directed self-assembly of quasi-2D cesium lead bromide perovskite nanoplates by liquid-air interfacial assembly. Due to their ionic crystal nature, perovskite nanocrystals are susceptible to degradation by most polar immiscible sublayer solvents such as acetonitrile and diethylene glycol. We used glyceryl triacetate as a liquid substrate for nanoplate self-assembly. By tuning the interfacial energy and volume fraction of nanoplates, we achieved monolayer ensembles of nanoplates with both face down and edge up ordering 30-100 μm in size.

Control over the ordering of these confined structures allowed us to access aligned electronic transition vectors in perovskite nanocrystal thin films. The effective transition dipole moment was modulated from 28° for face down assemblies to 46° for edge up assemblies. Control over dipole orientation in perovskite nanocrystals could lead to enhanced waveguiding, light outcoupling, and photon coherence in photonic devices.

a. Background

Liquid-air interfacial assembly is a common method to obtain highly ordered assemblies of nanoparticles (size: 1 – 100s nm) across large size scales (100s of μm to cm). [66,138–143] Interfacial and intermolecular forces can be tuned to access an energetic minimum to achieve the desired regime of assembly, such assembling quantum dots (artificial atoms) into superlattices with specific crystal structures or ordering anisotropically shaped particles.[89,140,143,144] This can be accomplished by tuning particle concentration[138,145] or by adding unbound ligand into the sublayer that creates attractive or repulsive van der Waals (vdW) intermolecular forces at the interface. [66,139] Additionally, nanoparticles can be 'trapped' into a certain regime if their native solvent evaporates faster than the rate of assembly.[89] For example, this method has been be used to achieve face-to-face versus edge-to-edge assembled monolayers, which has unlocked advanced functionality in robust chalcogenide nanoplates like enhanced non-radiative energy transfer and tunable dipole orientation of the ensemble.[66,89]

Perovskite nanocrystals of varied morphologies have garnered broad attention as a next-generation semiconductor as a revolutionarily bright emitter with remarkable defect tolerance and fast exciton diffusion. [17,18,62,146] There has been recent success in obtaining uniform, ordered films of the isotropic shapes of these perovskite nanoparticles. Notably, Baranov et al.[147] demonstrated assembly of isotropically shaped perovskite nanocubes into 3D superlattices using perfluorodecalin as a sublayer, and Cherniukh et al.[144] demonstrated assembly of perovskite nanocubes into monolayer films or into binary monolayer films along with Fe_3O_4 nanoparticles using glyceryl triacetate as a sublayer. However, for anisotropic morphologies in particular, their assembly at the liquid-air interface has had limited efficacy to date due to their ionic crystal nature and degradation in polar solvents (e.g. diethylene glycol, acetonitrile). [56–58] For perovskite nanoplates, limited control of the edge up versus face down regime has been achieved with other methods, such as controlling the evaporation rate of the native solvent when the colloid is drop-cast onto a solid substrate,[135] controlling the passivation of nanoplate surface charges,[125] or nanoplates are assumed to be mostly in-plane by introducing horizontal shearing via spin-coating.[148] Here, we demonstrated control over the regime of assembly via the addition of oleic acid in the sublayer, where assembly was aided by

modifying the volume fraction of nanoplates used, resulting in oriented dipoles in monolayer assemblies. Films of $CsPbBr_3$ perovskite nanoplates were characterized by transmission electron microscopy (TEM) as well as UV-vis spectrophotometry and atomic force microscopy (AFM). Angular emission of assembled thin films was characterized using Back Focal Plane Fluorescence Microscopy (BFPFM), which demonstrated the effect of controlled assembly on the effective dipole orientation of the film.

b. $CsPbBr_3$ nanoplate synthesis

$CsPbBr_3$ perovskite nanoplates were synthesized via a hot injection approach adapted from Bertolotti et al.[55] In brief, cesium carbonate was heated with oleic acid under inert to form cesium oleate. Lead bromide in mesitylene was dried under vacuum at room temperature and then solubilized using oleic acid and oleylamine while heating under inert. The temperature was changed to 99 °C and cesium oleate was injected. The reaction was immediately quenched, and the cyan-colored colloidal product was cleaned and size selected for further use. We note that a narrow size distribution obtained from careful size selection was necessary to observe ordered assemblies of nanoparticles.

The nanoplates were 14±3 nm laterally and 4±1 nm thick as characterized by TEM, corresponding to a thickness of 6 monolayers.[19,55] Figure 4.1 (a) shows as-synthesized nanoplates. Figure 4.1 (b) shows the absorbance of the nanoplates, which had two excitonic peaks at 431 nm and 470 nm, and relative photoluminescence spectrum revealing a narrow emission centered at 490 nm with a full width at half maximum (FWHM) of 18.8 nm. Typical synthetic variability resulted in emission centered at 488-492 nm. We note that by lowering the reaction temperature or increasing the total concentration of precursors, thinner nanoplates (ca. 3 monolayers) could be easily synthesized. However, they were assessed to be too unstable to withstand preliminary interfacial assembly attempts and subsequent TEM imaging.

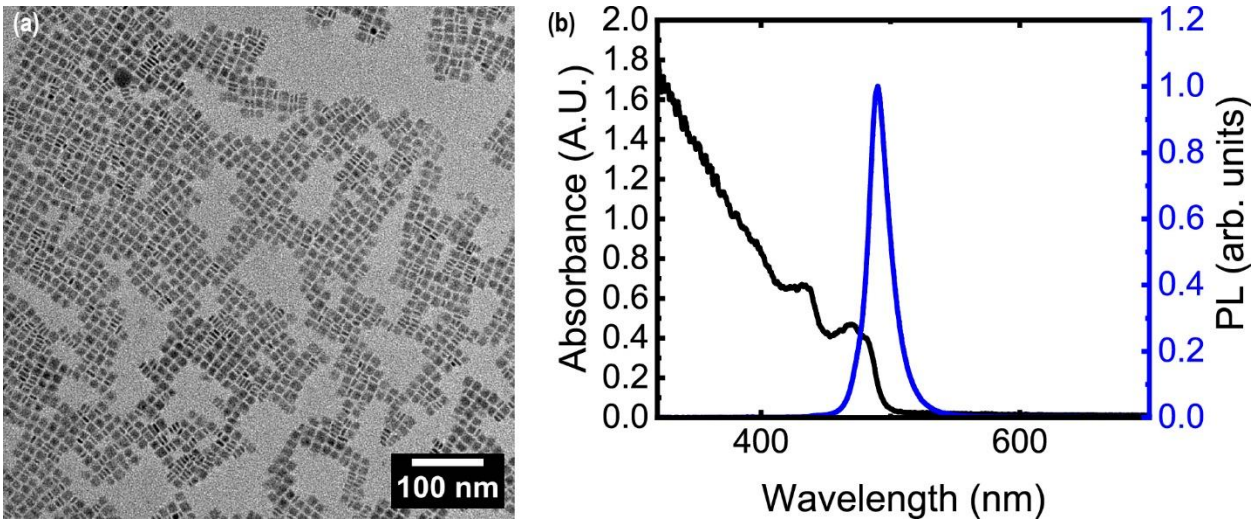

Figure 4.1. (a) Transmission electron micrograph showing as-synthesized $CsPbBr_3$ nanoplates with an average length of 14±3 nm and thickness of 4±1 nm. Plates can be seen in both the edge up and face down configuration when drop cast. (b) Absorbance and relative photoluminescence of $CsPbBr_3$ nanoplates emitting at 490 nm.

c. Nanocrystal assembly at the air-liquid interface

We hypothesized that air-liquid interfacial assembly could be tuned to control the orientation of anisotropic perovskite nanoplates in a monolayer assembly, and by extent the effective dipole orientation of the film, as demonstrated in other material systems. [66,89] In this approach, Brownian motion in the sublayer aids in achieving nanoparticle assembly into a thermodynamically favorable packing motif as the native solvent evaporates. The film is then transferred from the liquid sublayer to a solid substrate via controlled draining of the sublayer or via stamping the substrate onto the interface.[66,143] Sublayer choice can be used to directly tune the interfacial energy between particles and sublayer (Momper et al.[89] used acetonitrile to achieve an edge up assembly as opposed to diethylene glycol which delivered a face down assembly) or lower the contact angle between native solvent and sublayer, where a greater wettability is more desirable.[144]

An additional consideration in selecting a sublayer for use with perovskite nanoplates specifically was their rapid degradation in most polar solvents. A screening of sublayer candidates measured the relative photoluminescence of $CsPbBr_3$ nanoplates in hexane upon a small addition of each sublayer candidate (Figure 4.2). Photoluminescence intensity and peak position were tracked to understand particle degradation and fusing, as larger, fused particles will have redder emission. Acetonitrile and diethylene glycol were eliminated based on rapid decline in intensity and redshifting, indicating that particles were fusing and degrading. Fluorinert FC-40 showed greatest stability but was not selected based on the wettability considerations discussed in Cherniukh et al. for perfluorodecalin,[144] and due to the environmental and health concerns of fluorinated solvents.[149,150] Glyceryl triacetate (GTA) was selected as the sublayer since it produced minimal redshifting and significantly less photoluminescence degradation than acetonitrile or diethylene glycol.

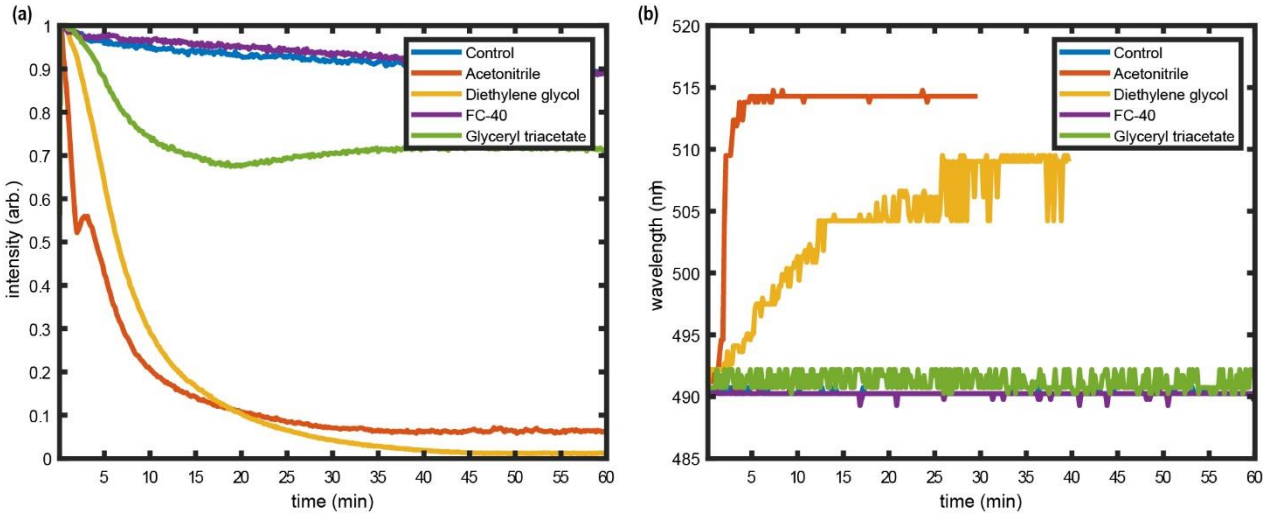

Figure 4.2. (a) Normalized maximum photoluminescence intensity and (b) center emission wavelength of $CsPbBr_3$ nanoplates in hexane after the addition of immiscible sublayer candidate (1% by volume)

The general film assembly process was as follows:

1. **Standardize dilution of nanoparticle suspension:** nanoparticle concentration was standardized in order to ensure repeatability in the number or volume fraction of particles in the assembly. Here, nanoplates in hexane were diluted to an optical density of 1.75 at 335 nm.
2. **Prepare liquid sublayer:** an immiscible sublayer was added to a petri dish along with a desired concentration of ligand, which was tuned to modulate the interfacial energy between nanoparticles and sublayer. Here, glyceryl triacetate was added to a 60 mm diameter petri dish along with 0 – 0.68 mM oleic acid.
3. **Cast nanoparticle suspension onto liquid sublayer:** nanoparticle suspension of a calibrated volume was dropped onto the liquid surface, which dictated the volume fraction of nanoparticles in the assembly. The dish was immediately covered to standardize the rate of solvent evaporation and protect the assembly process from outside movement of the surrounding gas. Here, usually 100-200 μL of the $CsPbBr_3$ nanoplate suspension was used.
4. **Transfer film:** Once the native solvent was completely evaporated, the cover was removed, and the assembled film was transferred to the desired substrate by stamping the substrate onto the liquid surface Here, substrate was a TEM grid or 22x22 mm borosilicate glass coverslip.

A schematic of assembly is given in Figure 4.3. See Appendix C for further details. Note that films were fabricated inside an argon glovebox to avoid detrimental oxygen and water exposure during assembly. Additionally, the glovebox purifiers were momentarily turned off and the glovebox was not allowed to refill to minimize airflow and reduce film disturbance.

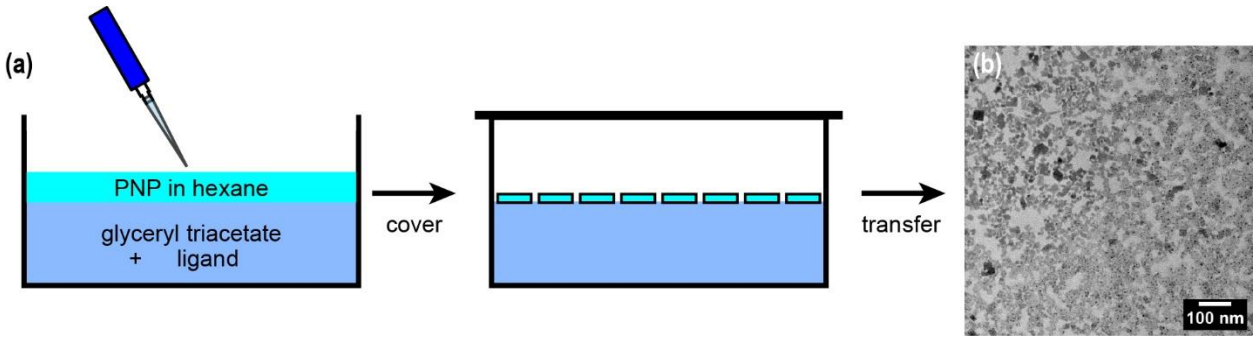

Figure 4.3. (a) Schematic of assembly at the liquid-air interface on a glyceryl triacetate (GTA) sublayer. The GTA forms an immiscible sublayer with hexane providing a liquid substrate on which nanoplates self-assemble during covered evaporation of hexane. (b) Transmission electron micrograph showing $CsPbBr_3$ film upon transferring to a solid substrate.

In this study, we explored how the addition of ligands to the sublayer and total volume of particle solution added affected the order and assembly of the anisotropic perovskite nanoplates. Nanoplates oriented face down have a larger surface area footprint than nanoplates oriented edge up (around 190 nm^2 versus 52 nm^2, respectively, exclusive of interparticle spacing and ligand chain length). Thus, we hypothesized that the volume fraction of nanoplates in the assembly could be tuned to achieve the desired phase where a higher volume (more total particles) would enable more edge up packing while a smaller volume (fewer total particles) would enable more face down packing. Such concentration-induced ordering is a well understood phenomenon borrowed from the field of lyotropic liquid crystals and adapted for our purposes.[145] Figure 4.4 shows the response in regime of assembly by changing the volume of nanoplate suspension added (effectively changing the volume fraction of nanoplates in the assembly). At lower volume fractions (100 μL), face down orientation was achieved most readily. Increasing the volume fraction resulted in a mix of orientations due to the energetic minimization of close packing, and at very high volume fractions (300 μL), aggregation and vertical stacking of plates were observed.

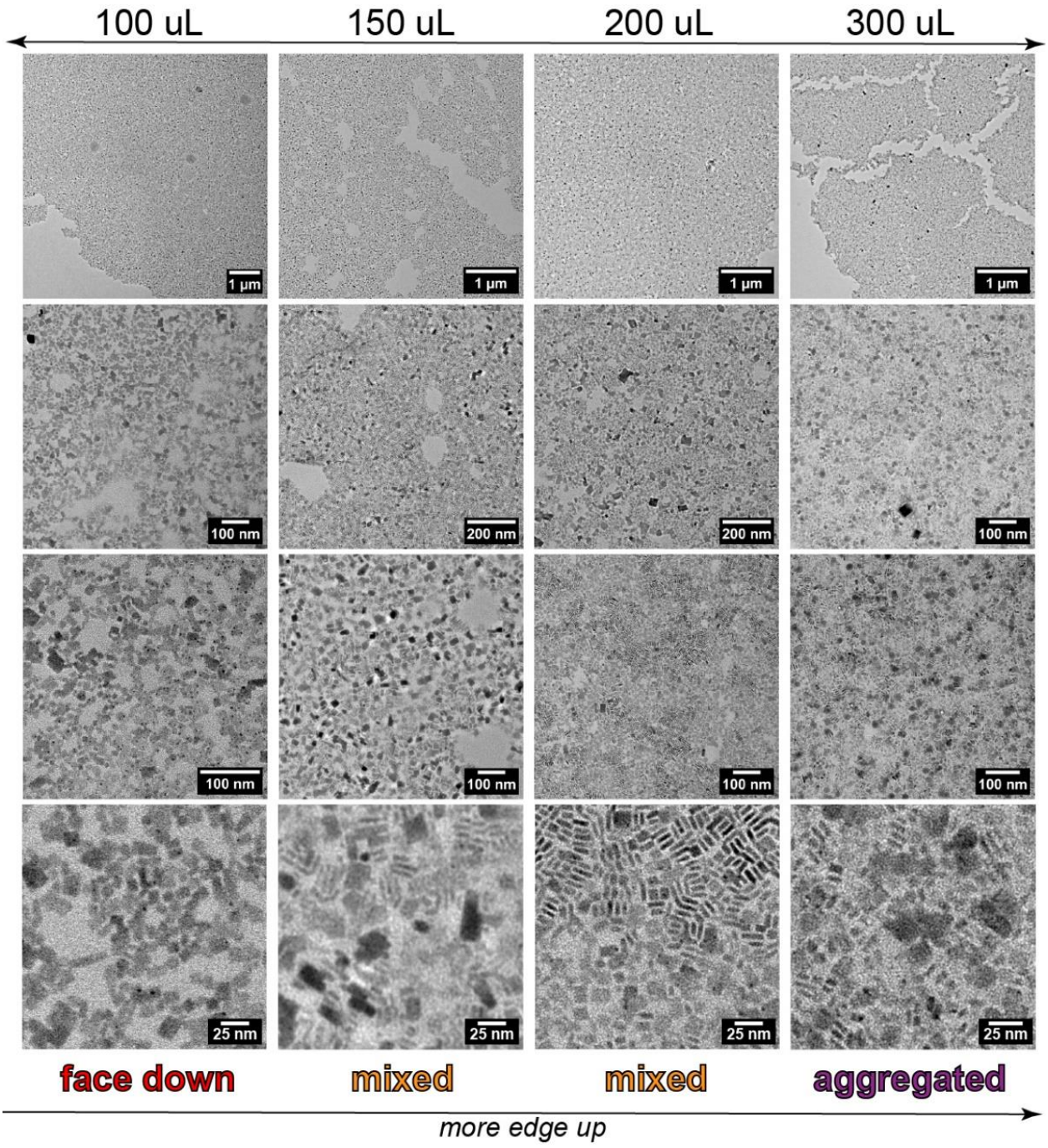

Figure 4.4. Transmission electron micrographs showing the evolution of assembly regime as the volume of nanoparticle suspension—and therefore total volume fraction of nanoparticles in the assembly—is increased from 100 to 300 µL. Images in row 4 are digitally cropped from images in row 3.

We hypothesized that a small addition of oleic acid (OA) into the GTA sublayer could be used to tune the orientation of the plates in the assembly by increasing the repulsive van der Waals (vdW) forces between the oleic acid/oleylamine-functionalized nanoplates and the sublayer.[151] This was reported in other nanocrystal systems to both tune the orientation and prevent nanoparticle aggregation.[66] Figure 4.5 shows a transition to edge up assembly when concentration of OA was increased for a consistent volume of nanoplates (200 μL). When no OA was added to the sublayer, nanoplates most readily assumed a face down regime. However, upon the addition of OA to the sublayer, we observed more edge up oriented nanoplates. We note that the optimum concentration is 0.68 mM OA as nanoplates assembled into edge up, nematic assemblies. At lower concentrations of OA (i.e. 0.068 mM), we observed a mix of edge up and face down particles, and at higher concentrations, we observed macroscopic aggregation on the surface of the GTA.

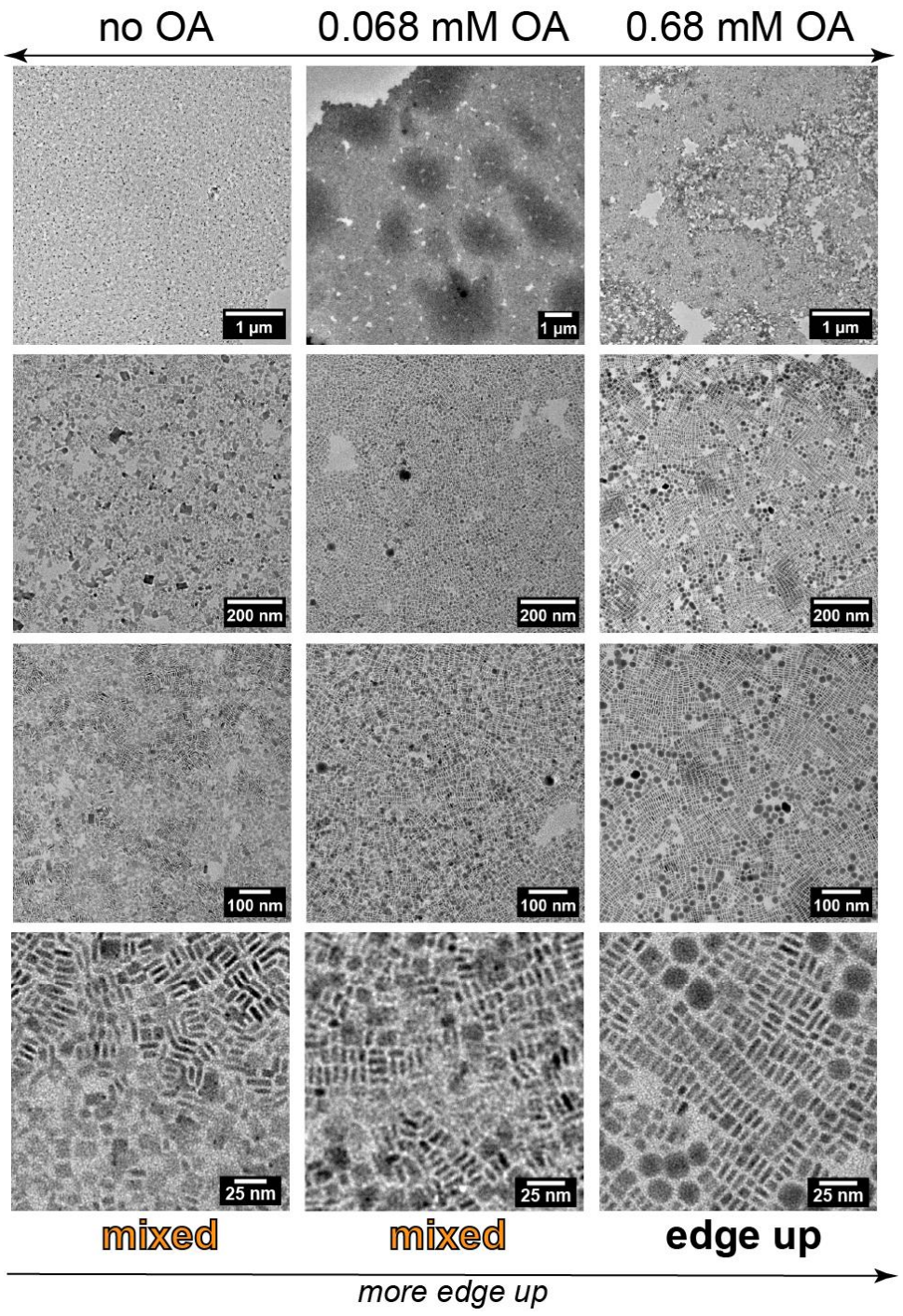

Figure 4.5. Transmission electron micrographs showing the evolution of assembly regime as the concentration of oleic acid in the sublayer is increased from 0 to 0.68 mM OA using 200 µL nanoplate suspension. Images in row 4 are digitally cropped from images in row 3.

Previous work by Gao et al.[66] reported ligand-directed assembly of only OA-capped CdSe nanoplates. We hypothesized that tuning the vdW interactions between both capping ligands in our system, oleic acid and oleylamine (OAm), might give finer control over the regime of assembly. TEM characterization of assemblies directed by OA + OAm addition are shown as Figure 4.6. We observed that adding both OA and OAm to the sublayer (0.68 mM OA and 0.66 mM OAm) yielded more undesirable aggregation than OA alone. Assemblies showed overlapping and multiple layers of plates and film bunching. Reducing the concentration of the unbound ligand concentration tenfold (0.068 mM OA and 0.066 mM OAm) yielded a monlayer film but the orientation was still clearly within the mixed regime, as evidenced by the presence of both face down and edge up nanoplates. We hypothesized that this may have been due to the amine group (NH_2) of the OAm and the carboxylic acid (COOH) of the OA having opposite effects on the interfacial energy, or the reaction of these two species in solution.

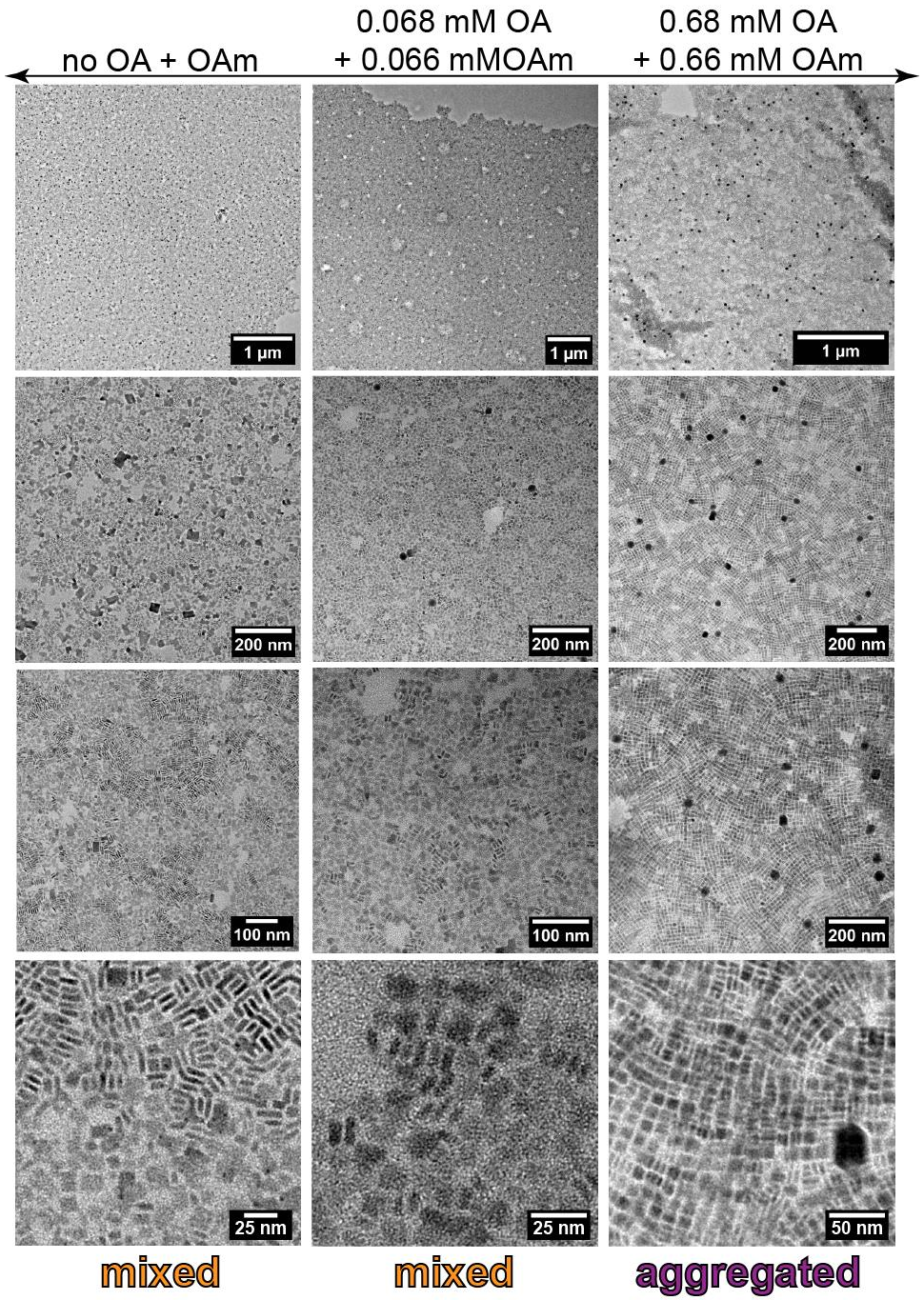

Figure 4.6. Transmission electron micrographs showing the evolution of assembly regime as the concentration of oleic acid plus oleylamine in the sublayer is increased from 0 to 0.68 mM OA + 0.66 mM OAm using 200 µL nanoplate suspension. Images in row 4 are digitally cropped from images in row 3.

Figure 4.7 provides a summary of the trends in assembly regime that can be achieved by tuning both the knobs of ligand concentration and nanoplate volume fraction via volume of nanoplate suspension added. A smaller volume fraction in the resulting assembly (100 μL vs 200 μL) thermodynamically favored a face down assembly due to unconstrained particle packing. The addition of OA to the sublayer (0.68 mM vs 0 mM) introduced repulsive vdW forces which induced an edge up configuration. While an edge up assembly was achieved for the smaller volume fraction of 100 μL also, we determined that the higher volume fraction case resulted in more ordered packing. Figure 4.8 shows the resulting interfacial assembly pathways to achieving face down and edge up films respectively.

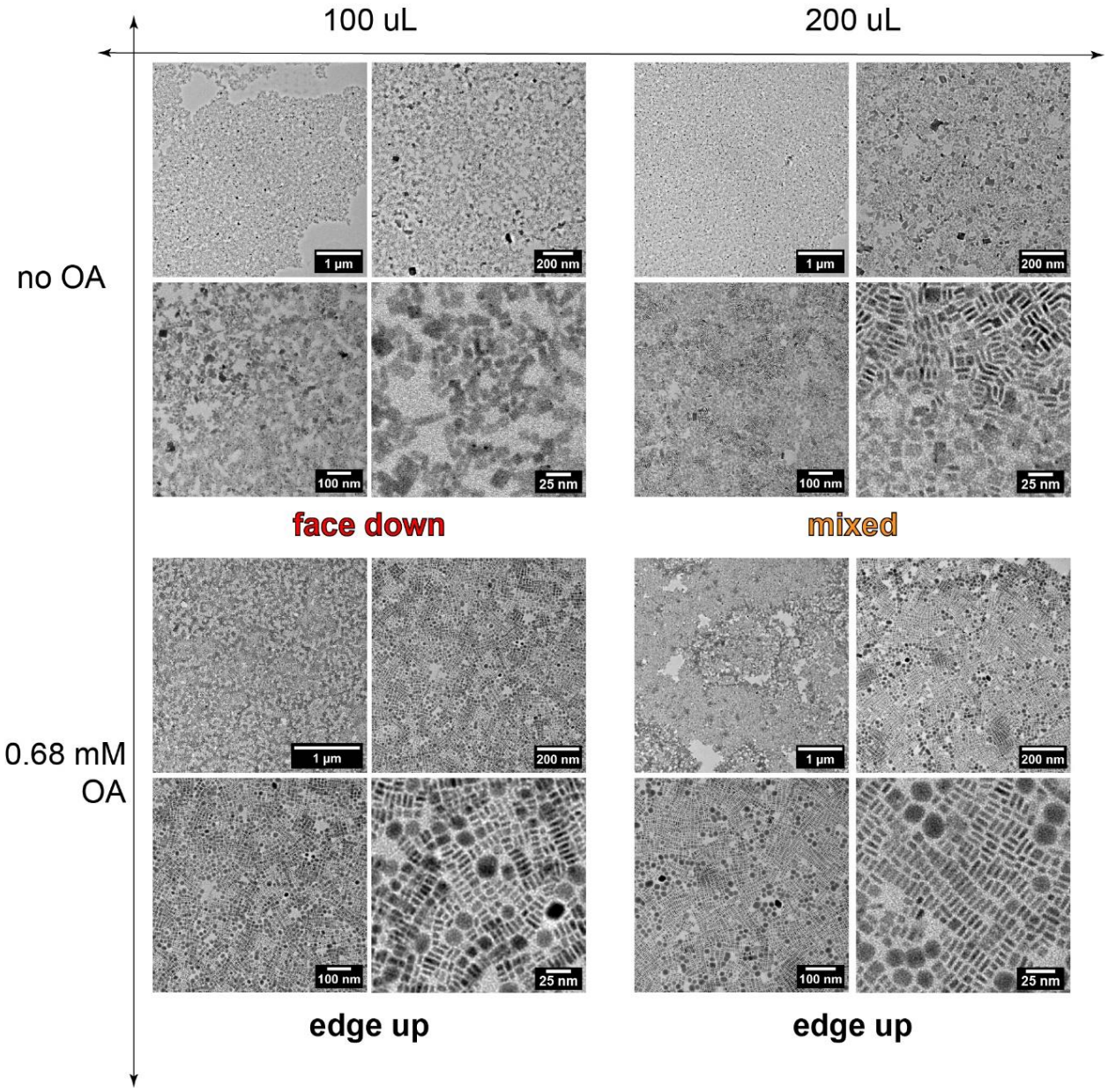

Figure 4.7. Transmission electron micrographs showing a summary of monolayer assembly regimes that can be achieved by tuning volume fraction and oleic acid addition. Images in the lower right quadrant for each condition are digitally cropped from images in the lower left quadrant for each condition.

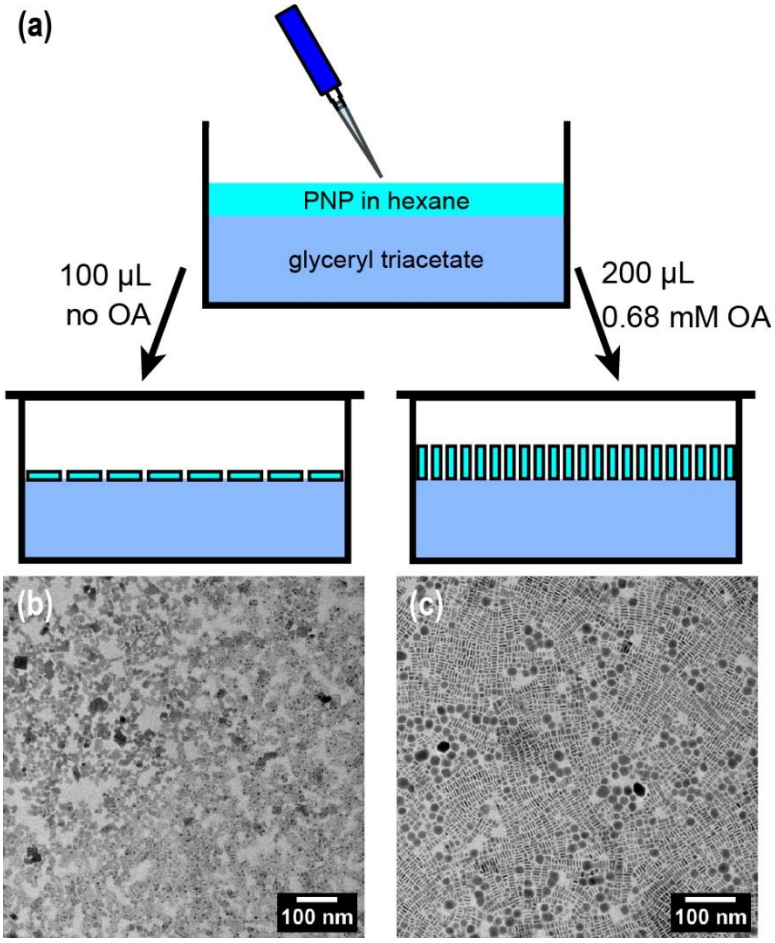

Figure 4.8. (a) Schematic of assembly at the liquid-air interface on a glyceryl triacetate (GTA) sublayer. The GTA forms an immiscible sublayer with hexane providing a liquid substrate on which nanoplates self-assemble upon evaporation of hexane. The addition of oleic acid in the sublayer causes nanoplates to assume an edge up configuration. Transmission electron micrograph showing $CsPbBr_3$ nanoplates assembled in a (b) face down and (c) edge up configuration.

d. Thin film characterization confirming ordering

Face down and edge up ensembles of $CsPbBr_3$ nanoplates were characterized to corroborate the regime of ordering and characterize them both optically and structurally. AFM was used to characterize film uniformity and thickness at the micron scale. From AFM, face down ensembles of nanoplates had an average thickness of 3.4 nm (Figure 4.9), and edge up ensembles had an average thickness of 15.2 nm

(Figure 4.10). This was in agreement with TEM particle sizing of 4±1 nm thick and 14±3 nm laterally. Figure 4.11 (b)-(e) shows face down assemblies and extracted AFM cross section. Both TEM and AFM revealed more gaps in the face down films at the nanometer and micron scale as compared to the edge up films—expected due to the lesser total volume fraction of nanoparticles. Figure 4.11 (f)-(i) shows edge up assemblies and extracted AFM cross section.

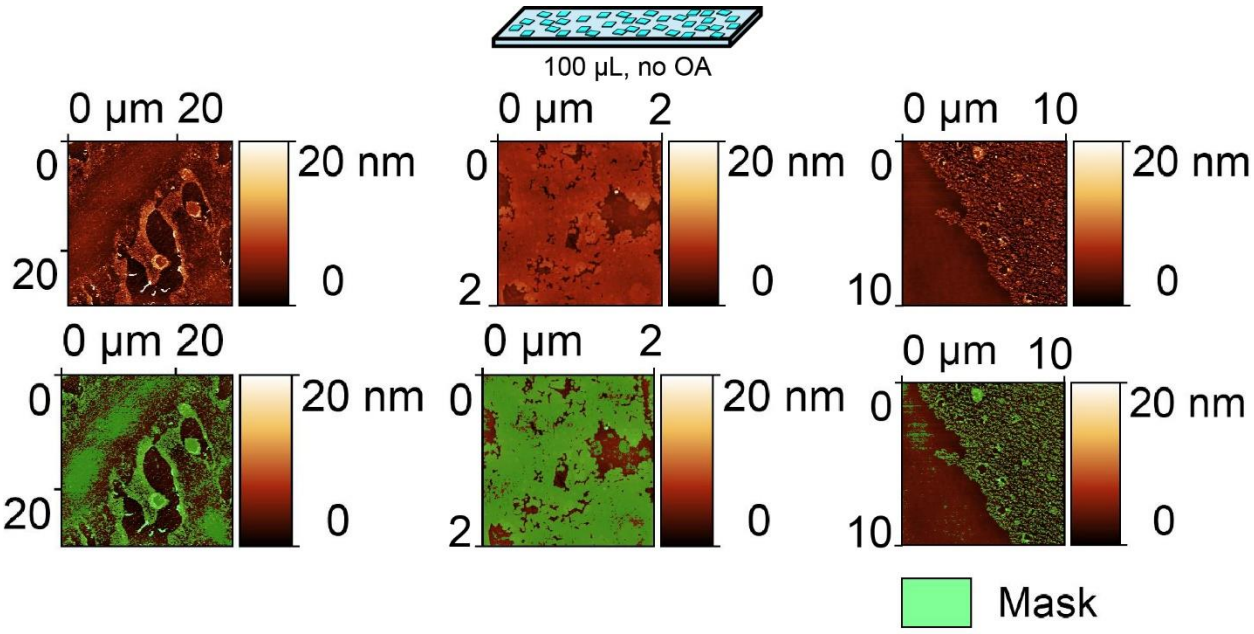

Figure 4.9. AFM showing face down assemblies, from which an average height of 3.4 nm was extracted using masked regions (green) and subtracted background.

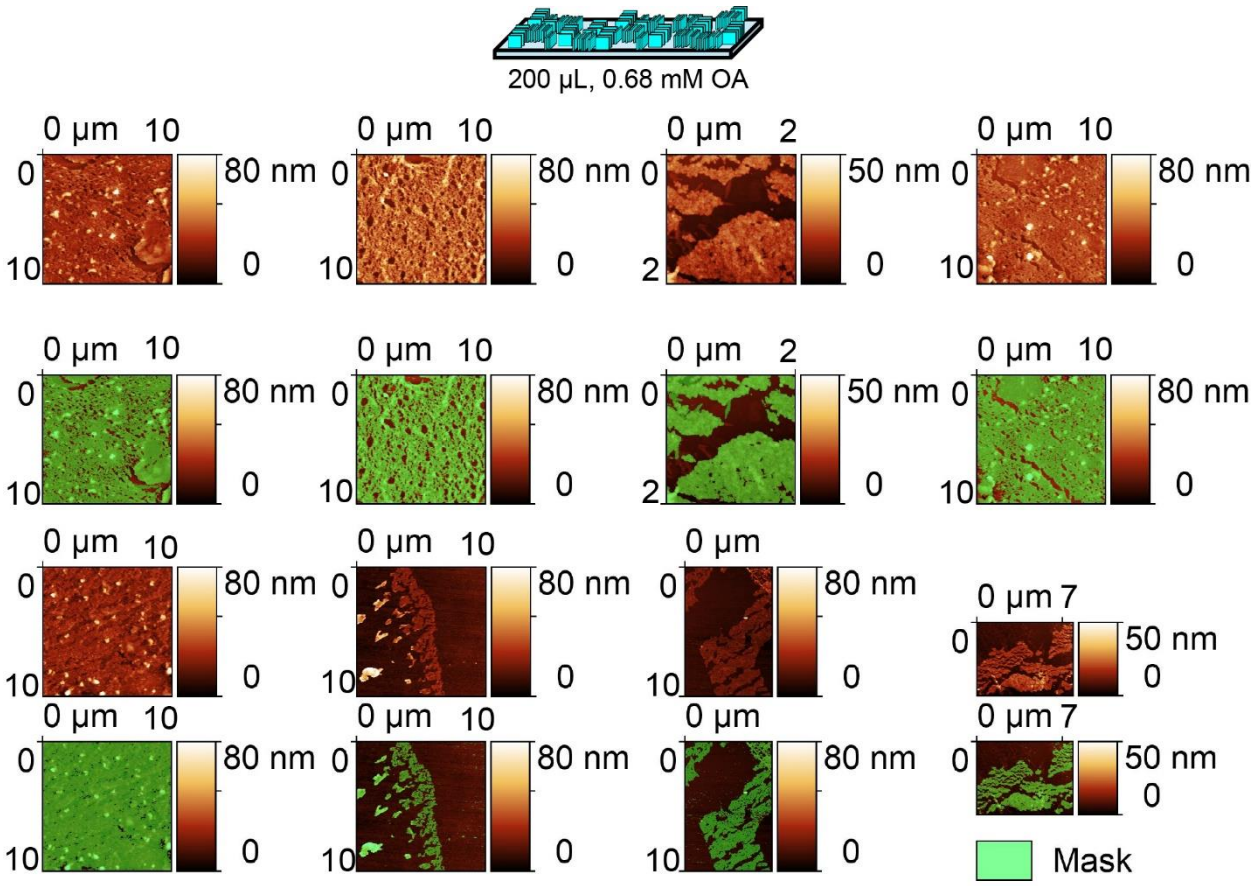

Figure 4.10. AFM showing edge up assemblies, from which an average height of 15.2 nm was extracted using masked regions (green) and subtracted background.

After transferring the assembled films to glass cover slips, relative photoluminescence of face down and edge up films showed emission centered at 493-496 nm and 491-496 nm, respectively (Figure 4.11 (a)). TEM was used to estimate the packing fraction of the face down and edge up regime at the nanoscale using a Bruggeman effective medium approximation for nanocrystal versus ligand area,[22,53] which resulted in an effective refractive index of 1.78 for face down assemblies and 1.87 for edge up assemblies. Figure 4.11 (b) and (f) shows TEM of larger assembled areas of the face down and edge regime, highlighting nanoscale aggregations at the edge of these assemblies that inevitably results in slight variability of thickness in the edge up regime. Thickness variability is further characterized by AFM as well as in Chapter IV.f. Resultant oriented dipoles.

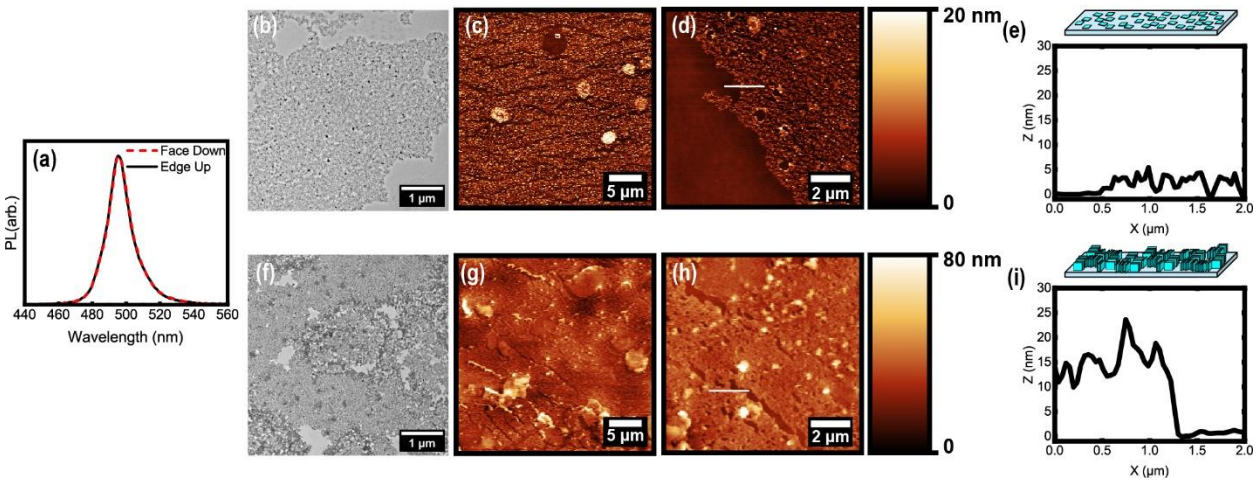

Figure 4.11. (a) Relative photoluminescence of face down and edge up assembled films showing emission at 496 nm and 495 nm respectively. For face down assemblies, (b) large area TEM showing interparticle spacing and (c)-(e) atomic force micrographs and extracted cross section showing film uniformity on a micron scale. The white line denotes where the 2 μm cross section was extracted. The average height of face down assemblies was 3.4 nm from AFM. For edge up assemblies, (f) large area TEM showing interparticle spacing and (g)-(i) atomic force micrographs and extracted cross section showing film uniformity on a micron scale. The white line denotes where the 2 μm cross section was extracted. The average height of edge up assemblies was 15.2 nm from AFM. Edge up assemblies showed more aggregation and film defects than face down assemblies.

Thicker areas and aggregations were prominently observed in edge up assemblies after being transferred to a solid substrate, particularly glass. AFM of large areas of complete aggregation are provided as Figure 4.12 (a). Additionally, the aforementioned coffee-ringing effect was also observed at the micron scale in samples where excess GTA sat before being evaporated under vacuum (Figure 4.12 (b)). In subsequent study of edge up assemblies, these highly aggregated areas were not included in our characterization. Future studies should investigate treatments to increase the hydrophobicity of substrate to combat this substrate-induced aggregation and deliver more pristine films larger than the 30 to 100 μm films seen here.

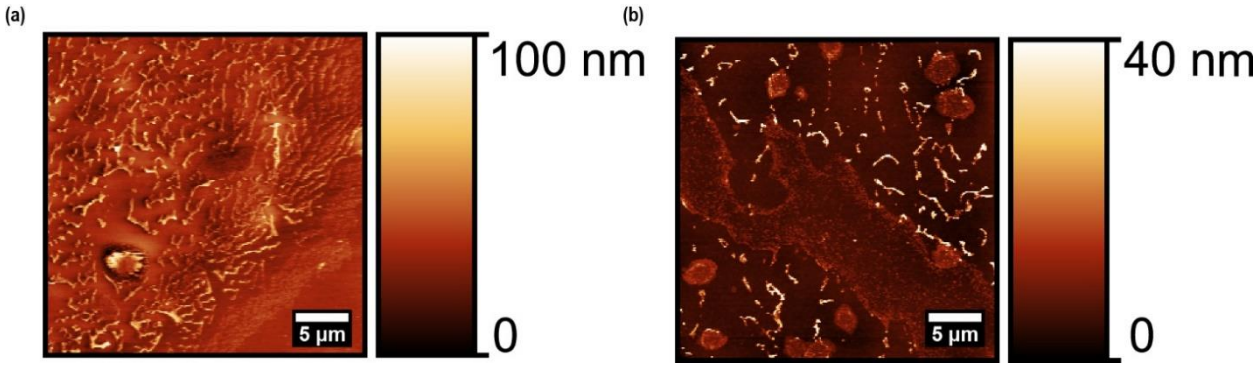

Figure 4.12. AFM showing (a) micron-scale aggregation commonly observed in edge up samples and on glass substrates and (b) coffee ringing-type aggregation that occurs from excess GTA on substrate.

e. Sensitivity and challenges of assembly

While this method produced large scale, highly oriented films of perovskite nanoplates, it was extremely sensitive to outside forces. For the effects of interfacial energy and vdW forces to control assembly regime, any other forces on the system had to be painstakingly minimized. Of note, movement of the surrounding gas of the environment had to be minimized as this was repeatedly observed to disrupt ordering of the particles. Similarly, any flow or bulk movement of the GTA or dust particles on the surface disrupted ordered assembly thoroughly. The GTA itself also caused some degradation of the nanoplates as revealed by sublayer screening study. Evident in Figure 4.8 (c), as a result, quasi-spherical aggregates are shown interspersed with the nanoparticle ensemble causing nanoscale interruptions to the film. After assembly on the liquid sublayer, the delicate assembly remained sensitive to aggregation and tearing when transferring to a solid substrate. For example, excess GTA droplets on the surface caused a coffee-ringing effect upon drying. The film could be easily torn while manually transferring it onto the substrate, and in particular, the hydrophilic nature of borosilicate glass causes repulsion of the non-polar capping ligands thereby causing disruptions to the nanocrystal assemblies. As a result, assemblies on glass were on the order of 30-100 µm as seen by AFM. Table 4.1 provides a summary of observed challenges to assembly.

Table 4.1. Challenges of assembly and mitigating steps

Challenge and resulting detriment to assembly	**Actions taken**	**Future suggestions**
Aggregation of particles • due to surface contaminations (e.g. dust, surfactant) • due to convection of gas or bulk movement of sublayer • upon contact with hydrophilic substrate	Inspect petri dishes, substrates for dust; sacrificial stamping of coverslip before casting NPs to attract micron scale contaminants; clean glassware using base bath; cover petri dish during assembly; turn off glovebox purifiers; prevent glovebox refill; allow sublayer to sit undisturbed before casting NPs	Hydrophobic substrates or substrate treatments
Degradation by sublayer	Sublayer screening for compatibility; use dry GTA	High-throughput sublayer compatibility study
Coffee-ringing due to excess sulayer droplets	Refrain from submerging substrate while stamping; use cover slip vacuum for more precision	

f. Resultant oriented dipoles

We characterized the resulting dipoles using fluorescence microscopy. We used widefield imaging to observe the film morphology, as shown in Figure 4.13. The gaussian intensity from the center of excitation is reflective of characteristic exciton transfer in the film. Features on the surface show the boundaries of nanoparticle assemblies. Film conformality showed similar motifs to AFM, including tearing and aggregated areas, and uniform assembled areas approached 100 μm in size.

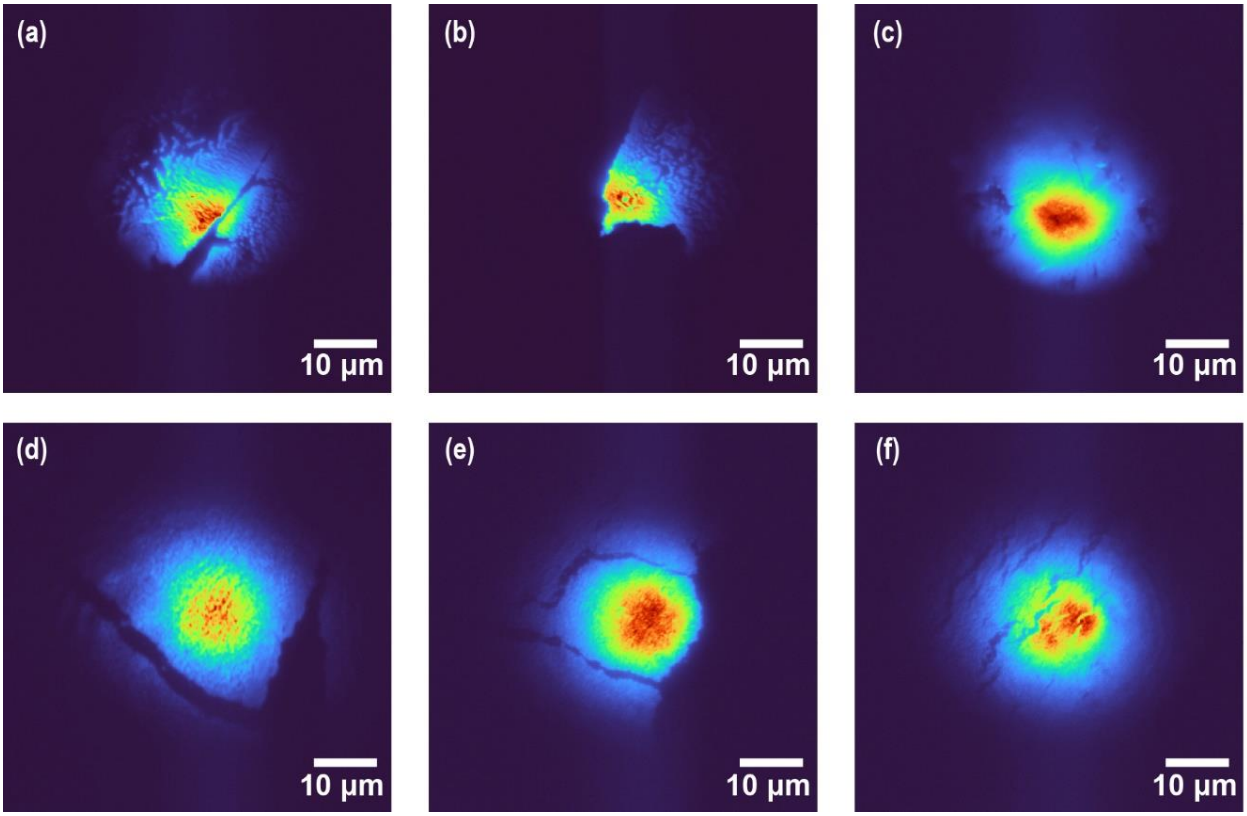

Figure 4.13. Fluroescence microscopy images of (a)-(c) edge up assemblies and (d)-(f) face down assemblies with an approximate scalebar of 10 µm.

We then performed Back Focal Plane Fluorescence Microscopy (BFPFM), in which the angular momentum space signal is collected across all measured angles simultaneously. This is accomplished by inserting a Bertrand lens into an inverted fluorescence microscope, which transforms the focal plane of the signal, according to the procedure described in Kurvits et al. [68] After changing the focus to the Back Focal Plane, angular emission signal is fit to a three-layer model of an emissive film as a function of momentum vectors, where the emission intensity (N_{pol}) in k-space (k_x, k_y) is given as [67,71]

$$N^{pol}(k_x, k_y) = C\left[\frac{1}{2}\left(\rho_{IP}^{p} + \rho_{IP}^{s}\right)\cos^2(TDM) \; + \rho_{OP}^{p}\sin^2(TDM)\right] \tag{4.1}$$

where C is a normalization constant. ρ_{ip}^{s}, ρ_{ip}^{p}, ρ_{op}^{p} are photonic density of states in the s- and p-polarized, in-plane and out-of-plane directions governed by the thickness, refractive index, and emission wavelength of the emissive layer. TDM is the effective angle of electronic transitions in the emitting layer, measured from the plane of the substrate in the z direction. TDM can be defined in terms of the dipole orientation factor Θ, which is the ratio of in-plane dipole contributions ($p_{\parallel}$) to all dipole contributions ($p_{\parallel}+p_{\perp}$).[64,69]

$$TDM = arccos(\sqrt{\Theta}) \tag{4.2}$$

$$\Theta = \frac{p_{\parallel}}{p_{\parallel}+p_{\perp}} \tag{4.3}$$

Details of BFPFM and dipole orientation fitting are provided in Chapter I.e. Key metrology.

In momentum space (or k-space), The p-polarized cross section of the signal (k_y=0) changes in response to dipole alignment (TDM). Figure 4.14 (a)-(c) shows how the signal evolves as a function of TDM, demonstrating the increase in intensity at $|k_x|\geq 1$ for increasing TDM. The s-polarized cross section of the signal (k_x=0) changes only in response to changes in the photonic density of states (thickness, RI, λ). Figure 4.14 (d) shows the s-polarized cross section for varying thickness, showing how the location of maximum intensity in k-space ($|k_{y,\text{max intensity}}|$) increases with increasing thickness of the emitting layer.[22]

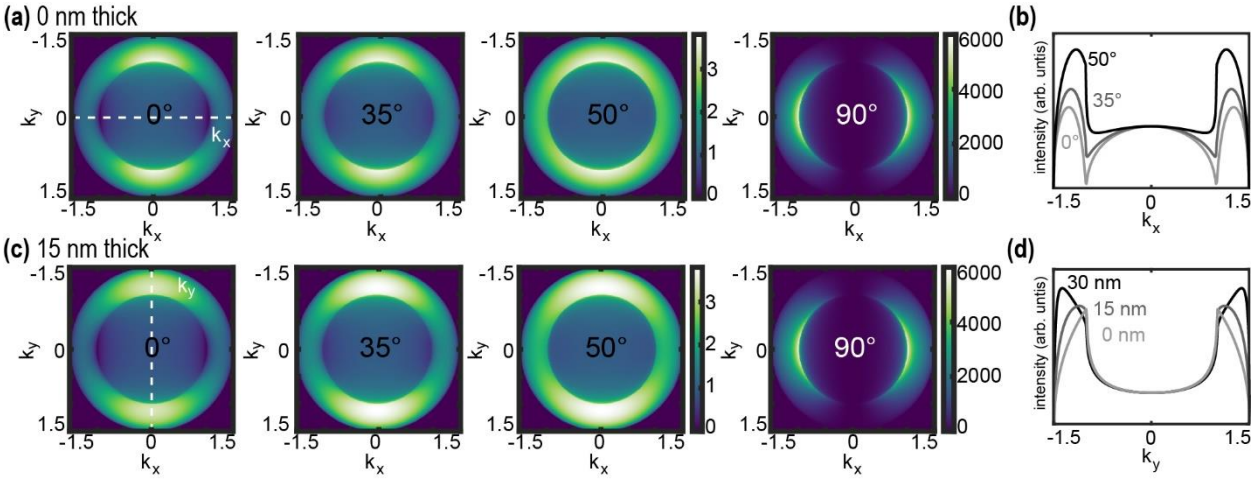

Figure 4.14. Modeled BFPFM signal for an emissive layer (a) 0 nm thick and (c) 15 nm thick with an effective transition dipole moment of the ensemble at 0° (in-plane contributions only), 35° (isotropic), 50°, and 90°(out-of-plane contributions only). (b) k_x cross section where k_y=0 for varying TDM. (d) k_y cross section where k_x=0 for varying thicknesses.

For an ensemble of strongly confined, ideal 2D plates oriented in-plane, the expected TDM would be 0° or Θ=1, completely eliminating out-of-plane dipole contributions. Ideal 2D plates oriented out-of-plane would have an expected TDM of 45° or Θ=0.5. The theoretical expected dipole contribution based only on the effect of particle geometry and orientation is given as Figure 4.15. Previous work accomplished tunability over this entire range (Θ=1 to Θ=0.5) using strongly confined 2D CdSe nanoplates.[66] For lightly confined perovskite nanoplates around 3 nm thick, previous work reported a TDM of 29° for face down plates.[22] Additionally, for perovskite nanocrystals, characteristic response to charge at an interface results in an enhanced vertical dipole contribution (Chapter III). We anticipated a modest enhancement of the vertical dipole contribution for edge up plates over face down plates, and an enhancement of the vertical dipole contribution in both regimes due to the glass interface.

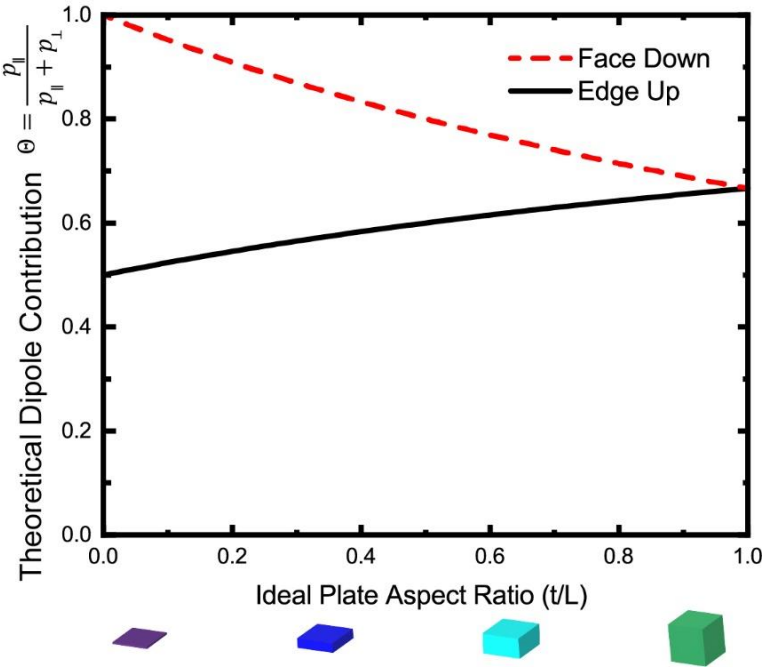

Figure 4.15. Theoretical dipole contribution for an ideal 2D or quasi-2D nanoplate geometry agnostic of surface response.

Also evidenced by TEM and AFM characterization, edge up assemblies partially aggregated upon transfer to a substrate, in particular glass. This, as well as lateral size variability of the plates (14±3 nm), arose in BFPFM data as changes in the k_y cross section due to film thickness. As such, data that could not be reasonably fit to 15 nm thickness was excluded from the reported average TDM fit for edge up assemblies. Figure 4.16 shows the k_y cross sections of data that were excluded from the reported fit, as well as the average k_y cross section and modeled k_y cross section at 15 nm.

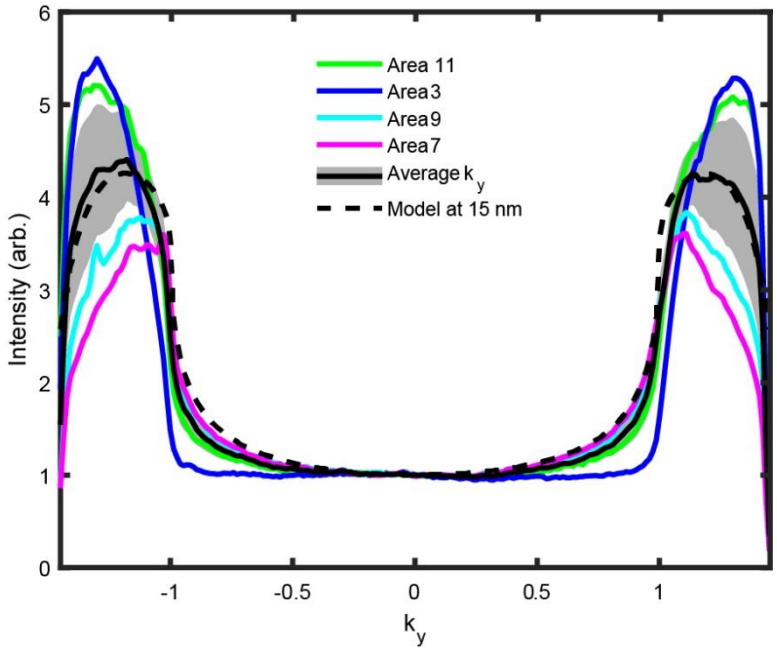

Figure 4.16. k_y cross sections for collected data that showed a poor fit to 15 nm, indicating thickness variation in edge up samples. Gray shading denotes one standard deviation from the average k_y across measured areas.

Figure 4.17 shows collected BFPFM signal and modeled signal of best fit for the face down and edge up assembly regimes. $|k_{y,max\ intensity}|$ for k_x=0 was greater for edge up assemblies than face down, corroborating other comparative measurements of thickness between regimes. Thus, face down assemblies were fit using a model thickness of 0 nm (phase shift is neglected), which is accepted approximation when the thickness is much smaller than the wavelength of light (film thickness from AFM = 3.4 nm),[53,66] and an RI of 1.78 from effective medium approximation. Edge up assemblies were fit using a model thickness of 15 nm in accordance with average film thickness from AFM (15.2 nm), and an RI of 1.87. Notably, signal intensity at $|k_x|\geq 1$ for $k_y = 0$ was greater for edge up assemblies than face down assemblies.

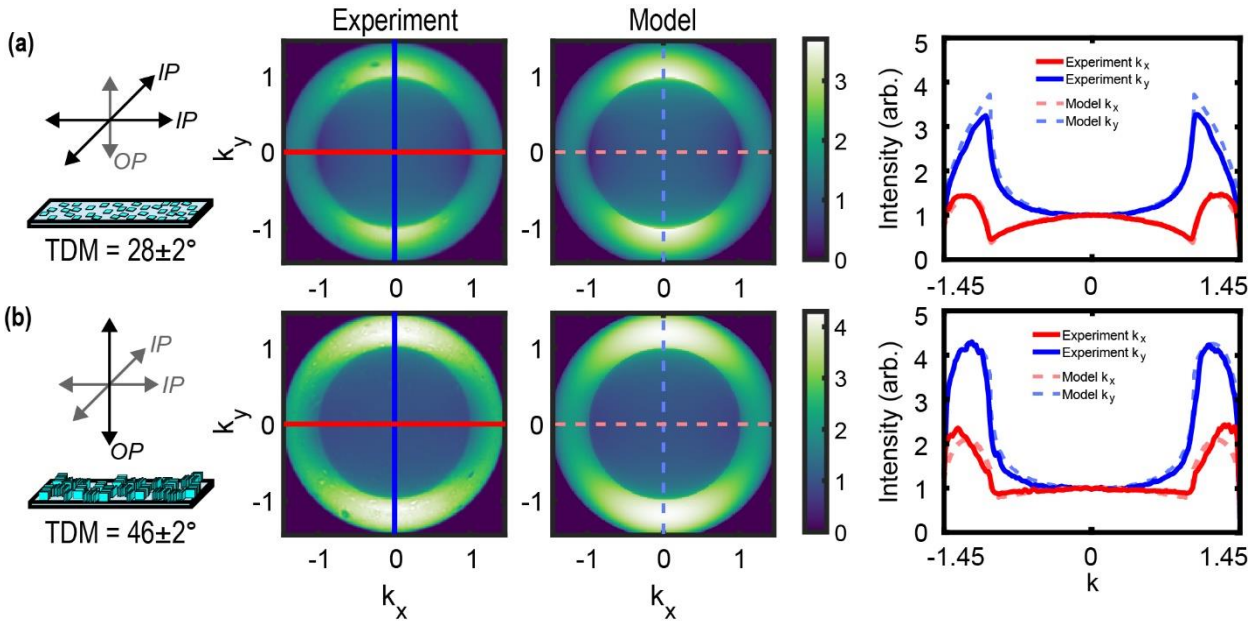

Figure 4.17. (a) Collected BFPFM signal, modeled signal of best fit, and extracted k_x (red) and k_y (blue) cross sections for face down assemblies with an effective TDM of the ensemble at 28±2° or Θ=0.78, corresponding to stronger in-plane dipole contributions. (b) Collected BFPFM signal, modeled signal of best fit, and extracted k_x (red) and k_y (blue) cross sections for edge up assemblies with an effective TDM of the ensemble at 46±2° or Θ=0.48, corresponding to stronger out-of-plane dipole contributions.

Ensembles of face down $CsPbBr_3$ nanoplates displayed a TDM of best fit of 28±2° (or Θ=0.78), as expected from previous reports of face down nanoplates of similar nanoplate thickness on glass (29°, around 3 nm thick). These plates were lightly confined, and thus, we did not anticipate transitions along the out-of-plane thickness dimension of the plate to be completely eliminated. In accordance, for a face down assembly, the observed Θ was less than an ideal 2D plate oriented in-plane. Of note for perovskite nanomaterials, charge redistribution at the surface due to ionic lattice nature serves to reduce the dipole orientation factor below even what a lightly confined geometry would suggest.[22,53,54,112,131] These effects both served to reduce the effective dipole orientation of the ensemble below ideal.

Ensembles of edge up $CsPbBr_3$ nanoplates displayed a TDM of best fit of 46±2° (or Θ=0.48). Due to their light confinement, we would expect the dipole orientation factor of an edge up ensemble to be

slightly higher than an ideal 2D plate oriented out-of-plane, which would be 45° or Θ=0.5. However, the observed dipole orientation factor was again lower (Θ=0.48 versus 0.5), which we attributed to the effect of interfacial charge generation on the ionic lattice. These two effects worked in opposition such that the apparent effect of interfacial charge generation was diminished: edge up nanoplates showed a dipole orientation factor that was reduced by 4% below ideal, while for face down nanoplates, the dipole orientation factor wase reduced by 22% below ideal.

g. Liquid-air interfacial assembly for other morphologies of $CsPbBr_3$

To explore the range of uses for liquid-air interfacial assembly for perovskite nanocrystals, we applied the method to other morphologies of $CsPbBr_3$ nanoparticles with different ligand binding. Figure 4.18 shows TEM ((a)-(c)) and AFM ((d)-(f)) of DDAB stabilized $CsPbBr_3$ nanoparticles (isotropic shape) assembled into a close-packed monolayer on glyceryl triacetate and transferred to a solid substrate. For certain applications, this offers increased monolayer film density on untreated borosilicate glass over what was achieved by spin coating (Chapter III).

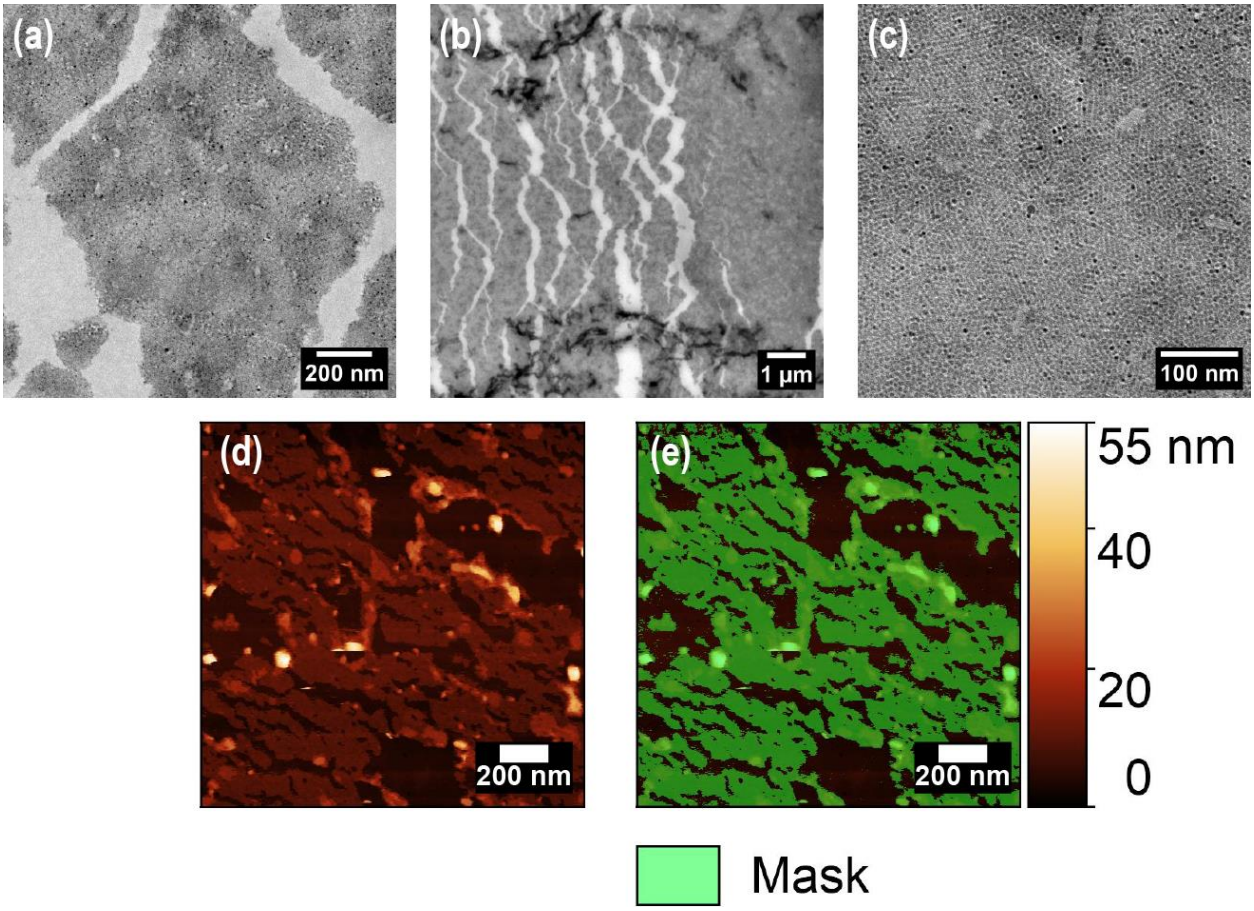

Figure 4.18. (a)-(c) TEM showing DDAB-stabilized isotropic $CsPbBr_3$ nanoparticles assembled at the liquid-air interface diluted 40x from reaction concentration in heptane. (d)-(e) AFM showing assemblies on glass from which an average height of 6.9 nm was extracted (particle diameter ca. 7.4 nm).[112]

Additionally, $CsPbBr_3$ nanoplates synthesized by microemulsion approach[125] stabilized by only oleylamine were assembled on an FC-40 sublayer. Figure 4.19 (a)-(d) shows TEM of oleylamine-capped nanoplates. [112] In previous characterizations (Chapter III.c.), nanoplates were estimated to be around 9.5 nm laterally and around 3 monolayers (ca. 1.8 nm thick) based on the emission wavelength (462 nm). Some larger, fused flakes were observed, 100s of nm laterally.[112] In this study, we noted similar lateral fusing of assembled nanoplates (Figure 4.19 (c)-(d)). BFPFM images of such assemblies showed more in-plane dipole contribution than nanoplates synthesized via hot-injection that did not readily fuse. Across sampled areas, best fit TDMs ranged from 0° to 34° for a modeled emissive layer 0 nm thick. and emission

wavelength of 462 nm. Since RI is not known, we fit emission data to the range of expected RI, which is 2 (literature value for nanoplate film)[22] to 2.3 (only perovskite). The average of best fits at each RI was 9° and 12° respectively. We stress that for cases of largely in-plane alignment, small changes in signal correspond to a large change in best fit dipole orientation.[72] Figure 4.19 (e)-(f) shows experimental BFPFM signal and best fit modeled BFPFM signal at 0°, for a model thickness of 0 nm, emission at 462 nm, and RI of 2.0, and (g) shows the average p-polarized cross section and associated standard deviation, illustrating the narrow range of signal that can evolve the best fit TDM substatially. Preliminarlily, this result suggests that the contribution of in-plane dipoles in electronically responsive $CsPbBr_3$ nanocrystals—which typically shows a diminished horizontal contribution on glass[22,53,112]—may be enhanced with dramatic material aspect ratios (L/t>>100, approaching nanosheets).

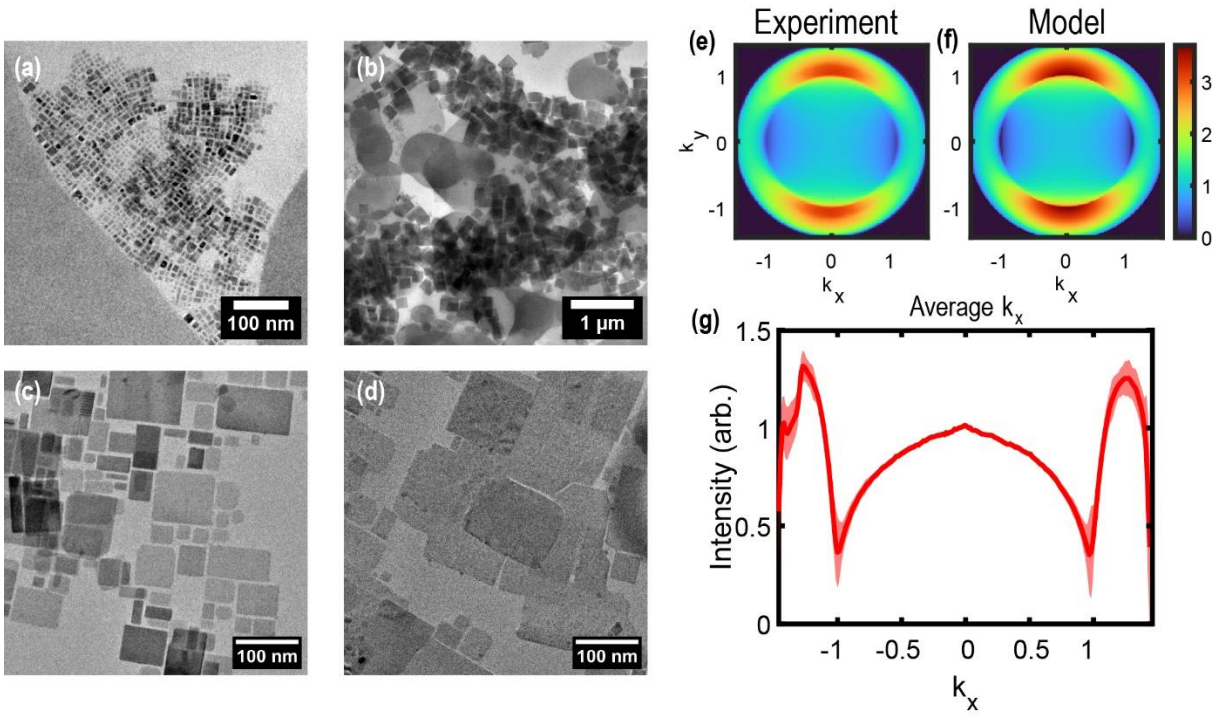

Figure 4.19. (a)-(b) TEM of smaller (estimated length 9.5 nm, 3 monolayers thick) and larger (up to 100s nm long) fused populations of oleylamine-capped nanoplates. (c)-(d) Fused nanoplates assembled on FC-40. (e)-(f) Collected and modeled BFPFM signal for a sample area with a best fit TDM of 0°. (g) Average p-polarized cross section (k_x) for sampled areas, which displayed a range of best fit TDMs from 0° to 34°. Shading indicates one standard deviation from the average.

h. Conclusions and outlook

We showed that by careful sublayer selection, assembly at the liquid-air interface can be applied to delicate inorganic lead halide perovskite nanocrystals. By tuning the knobs of volume fraction and interfacial energy via addition of unbound ligand in the sublayer, we could direct monolayer assembly on the order of 30 to 100 μm into the face down or edge up regime. We then characterized momentum-resolved photoluminescence of the resultant films, uncovering the interplay of orientation and confinement—as well as characteristic response to surface charges—on the effective orientation of dipoles in 2D ensembles of $CsPbBr_3$ nanoplates. Since the out-of-plane dipole contribution of a lightly confined plate is not completely

eliminated, we did not expect to achieve dipole orientation control over the entire range of effective TDMs that are theoretically possible for 2D morphologies (0° to 45°).[66] However, paired with the characteristically enhanced vertical dipole contribution of $CsPbBr_3$ nanocrystals on glass, we can achieve a vertical effective TDM of greater than 45°. Face down assemblies of lightly confined nanoplates showed a TDM of 28±2° (Θ=0.78), while edge up assemblies showed a TDM of 46±2° (Θ=0.48).

This method for achieving thermodynamic nanocrystal assembly, while common in other material systems,[66,89,139] has had limited success for perovskite nanocrystals.[144,147] This work provides a promising route by which the technique may be leveraged for applications that benefit from both in-plane or out-of-plane specific modes of emission, such as solar concentrating technologies, LEDs, or quantum information technologies.[11,14,31,73,114,152] With improved substrate compatibility, these assemblies could be realized over larger areas (>1 cm), and for more extreme shapes approaching 1D (nanorods, nanowires), vertical assembly could enable nearly entirely in-plane light emission.

V. CONCLUSION

Control over the electronic and photonic interactions inside a photonic device, and specifically in the uniquely tunable cesium lead halide perovskite nanocrystals, can deliver an immense payoff in specificity of angular modes and optical efficiency. We demonstrated that using a nanophotonic waveguide as an LSC, coupled to InGaP and Si subcells, could provide a cost-competitive advantage over a single junction silicon cell, suggesting that efficiencies over 31% are possible in an optimized design case. The result indicates the need for minimized reabsorption and escape losses, as well as for a very thin device. With a high degree of complexity and parameter specificity needed to achieve such a design, we make the case to move towards anisotropic emitters as a route to alleviate much of these optical losses.

We delivered our results characterizing the unique electronic response of isotropic $CsPbBr_3$ nanocubes to substrate work function mismatch. The dipole orientation factor is modulated by the presence of an electric field generated at an interface. As a result, we were able to achieve not only better film uniformity but induce a tunable change in the dipole orientation by more than 20% (Θ=0.47 to Θ=0.59) by introducing substrate treatments that brought the work function closer to that of the nanocrystals (PMMA, perovskite). This motivates future work that could instead identify higher work function materials to induce an anisotropic response, and potentially further improve film uniformity and packing, which is also known to affect the dipole orientation factor for perovskite nanocrystals.

We developed a route to apply liquid-air interfacial assembly to delicate $CsPbBr_3$ perovskite nanoplates and leveraged it to achieve face-to-face and edge-to-edge assembled monolayers 30-100 μm wide by tuning nanocrystal volume fraction and interfacial energy. We characterized the oriented films and showed that this method could be used to modulate dipole alignment to favor emission towards both in-plane and out-of-plane based on particle orientation (Θ=0.48 and Θ=0.78). Future work should identify hydrophobic substrate choices and treatments to apply this approach and move to larger size scale assemblies, which will deliver control over photon momentum for a range of applications and size scales.

Understanding the chemical, thermodynamic, and electronic behavior of this nascent material class precludes the use of these nanocrystals in advanced photonics devices such as concentrators, LEDs,

photovoltaics, waveguides, and qubits. Elaborated here is the culmination of our efforts towards high precision photon momentum control, targeting an entirely new field of devices (non-traditional optoelectronics) and materials ($CsPbX_3$ nanocrystals). This work informs our fundamental understanding of physics and chemistry in the context of light-material interactions at the quantum level by uncovering how color and composition is linked to dipole moment and photon momentum. Answering crucial mechanistic questions about this new material class, perovskite nanocrystals, as well as rethinking with advanced understanding the manufacture and performance characteristics of photonic devices, this fundamental knowledge provides a framework for optoelectronics and nanophotonics from the nano- and device-scale.

Our expanding energy demands necessitate radical developments to the field of optics and optoelectronics to enable energy efficient devices. By surpassing what is considered to be traditional optics, breakthroughs in the fields of solar power, lighting, and information systems are possible. In the face of rapidly increasing computational energy demands globally, we have the potential to reframe and redefine photonic device efficiency by engineering light directionality from the nanoscale. This technology shows promise not only to the fundamental science community but also to increase the economic viability of solar as a renewable energy source. The result of the implementation of these advances is both a relieved energy burden and a reduced dependence on fossil fuels within the energy sector.

APPENDIX A: MATLAB CODE FOR CHAPTER II—PHOTONIC LUMINESCENT SOLAR CONCENTRATOR DESIGN FOR HIGH EFFICIENCY, LOW COST MULTIJUNCTION PHOTOVOLTAICS

Script that calculates Total Module Efficiency:

```
clc;
clear all;
%%
mod_eff = zeros(11,42);
%%

%Concentration = linspace(1,500, 20);
Concentration = 100;
%for r = 1:8

%for q = 1:20
    tic
%%
ODnames = ['OD05 ' 'OD075 ' 'OD1 ' 'OD15 ' 'OD2 ' 'OD25 ' 'OD3 ' 'OD35 ' 'OD4 ' 'OD45
' 'OD5'];
OD = strsplit(ODnames);
ODvals = [0.5, 0.75, 1, 1.5, 2, 2.5, 3, 3.5, 4, 4.5, 5];
wavelength = linspace(300,1000,701);
layernum = linspace(4,86,42);
layerstr = num2str(layernum);
layer = strsplit(layerstr);
thick = (layernum-2).*0.5*1775*10.^-6;
[X,Y] = meshgrid(thick(1:42),ODvals);

C_si = 1;
ERE = 0.01;
absorb = 0.9649;
Eg_si = 1.14;


%%
A=importdata('E_flux.mat');
E=flip(A.E);
flux=flip(A.flux);
WL= 1242.1875./E;
targetWL = linspace(300,1000,701)';
targetE = flip(1242.1875./targetWL);



fluxInterp = interp1(WL, flux, targetWL);



%%
```

```
for m = 1:11
    for n=1:42
    filename = "TAR_" + layer(n)+"layer_"+OD(m) ;

fileID = fopen(filename,'r');
formatSpec = '%f%f%f';
A = textscan(fileID,'%s','delimiter','\n');
fclose(fileID);
B = A{1,1};
for i = 706:1406
L(1:2,i-705)= strsplit(B{i});
end
D=str2double(L);
TRANSM=D';

curveflux = flip(TRANSM(:,2).*fluxInterp);
[slice_inc_power, speceff, cell_power, cell, Jtot, v] = indepDB(Eg_si,C_si,
curveflux, targetE, ERE, absorb);

incidentpwr_si(m,n)=slice_inc_power;
convpwr_si(m,n)=cell_power;




   end
end




% figure
% mesh(X,Y,convpwr_si)
% colorbar
% xlabel('LSC thickness (mm)');
% ylabel('optical density');
% zlabel('Power converted by Si Cell (w/cm2)');

C_ingap = Concentration;
ERE = 0.05;
absorb = 0.8989;
Eg_ingap = 1.84;


%%
A=importdata('E_flux.mat');
E=flip(A.E);
flux=flip(A.flux);
WL= 1242.1875./E;
targetWL = linspace(300,1000,701)';
targetEtot = flip(1242.1875./targetWL);
targetE = targetEtot(401:701);
```

```
fluxInterp = interp1(WL, flux, targetWL);

%%


for m = 1:11
    for n=1:42
    filename = "TAR_" + layer(n)+"layer_"+OD(m) ;

fileID = fopen(filename,'r');
formatSpec = '%f%f%f';
A = textscan(fileID,'%s','delimiter','\n');
fclose(fileID);
B = A{1,1};
for i = 1:701
P(1:2,i) = strsplit(B{i+2});
end
D=str2double(P);
ABS=D';

curvefluxtot = flip(ABS(:,2).*fluxInterp);
curveflux = curvefluxtot(401:701);
absphot=(701-401).*(curveflux(1)+2.*sum(curveflux(2:300))+curveflux(301))./600;

Num_reabsorption(m,n) = calc_reabsorb_events(ODvals(m),thick(n),Concentration);
% trap_eff = trap_eff_init.^Num_reabsorption(m,n,q);
trap_eff = (0.74).^Num_reabsorption(m,n);
xval = 401:701;
plcurve=absphot*normpdf(xval,630,11.57).*trap_eff.*0.98;
[slice_inc_power, speceff, cell_power, cell, Jtot, v] = indepDB(Eg_ingap,C_ingap,
plcurve', targetE, ERE, absorb);

incidentpwr_ingap(m,n)=slice_inc_power;
convpwr_ingap(m,n)=cell_power;
Siefficiency(m,n)=speceff;



   end
end

% figure
% mesh(X,Y,convpwr_ingap)
% colorbar
% xlabel('LSC thickness (mm)');
% ylabel('optical density');
% zlabel('Power converted by InGaP Cell (w/cm2)');
```

```
for n = 1:11
    for m = 1:42

mod_eff(n,m) = 100.*((convpwr_si(n,m))./0.1 + (convpwr_ingap(n,m))./0.1./C_ingap);
    end
end
toc
%end
%end
%%

% [X,Y] = meshgrid(Num_reabsorption,Concentration);
figure(1)
contourf(X,Y,mod_eff)
colorbar
xlabel('Device Thickness (mm)');
ylabel('Optical Density');
zlabel('Sub Module Efficiency');

set(gca, 'FontName', 'Arial');
'LineWidth',2;
```

Function that performs Reabsorption Events Calculation:

```
function [num_reabsorb_events] = calc_reabsorb_events(OD, thickness, Concentration)
%REABSORB_EVENT calculates the expected number of reabsorption events
%within a CdSe/CdS LSC given its Optical density and geometry
%
l = 0.3./OD;
r = 2.*thickness.*Concentration.*0.1;

val = l/r;

sample_vals = [5 4 3 2.5 2 1.5 1 0.75 0.5 0.333 0.25 0.2 0.16667 0.125 0.1 0.05
0.025];
sample_coeffs = [28.1 18.5 10.9 7.9 5.3 3.2 1.7 1.1 0.67 0.42 0.33 0.28 0.24 0.20
0.18 0.15 0.13];

if val>5
    num_reabsorb_events = 1;
elseif val<0.025
        num_reabsorb_events = 0.125.*(val.^-2);
else

coeff = interp1(sample_vals, sample_coeffs, val);

num_reabsorb_events = coeff.*(val.^-2);
    end


end
```

Script for Monte Carlo LSC Simulation:

```
%% concentration for big matrix.m
% by Lindsey Parsons 13 april 2023
% photons are assigned a direction in this code
% change certain LSC parameters to predict PLSC performance using Monte
% Carlo. This geometry represents edge collection and has the option for
% filter reflectivity
clear; close all; clc;
rng('shuffle')

%% initialize vars

% LSC will be LxL
L = 100; %cm
thick = 1; %cm

% transition dipole moment we will call theta
theta = 91; %put 91 for isotropic emission

% refractive index
RI_substrate = 1.5;
RI_air = 1.0003;

if theta<91
    trap_eff = sqrt(1-(RI_air/RI_substrate).^2).*(1 +
(0.5.*(RI_air/RI_substrate).^2).*(1-1.5.*sin(theta).*sin(theta)));
else
    trap_eff = sqrt(1-(RI_air/RI_substrate).^2);  %isotropic emission
end
L = logspace(1,5,12);
QYvals = [0.5, 0.85, 0.9, 0.95, 0.97, 0.99, 0.999, 0.9999, 0.99999, 0.999999,
0.9999999, 0.99999999, 1];
trap_eff_vals = [0.74, 0.89, 0.91, 0.95, 0.97, 0.98, 0.99, 0.999, 0.9999, 0.99999,
1];
alphavals = linspace(0,0.1,10);

for b = 1:10
for a = 1:11
for m = 1:12
for n = 1:13
QY = QYvals(n);
%QY = 0.99;

trap_eff = trap_eff_vals(a); %this is calculated by mulder equations above but you
can
%edit manually to experiment here

%will have option for filter later. This will need to be corrected for number
%of bounces
filter_reflectivity = 1;


gridsize = 1000;
numPhotons_init = 10000;
```

```
numPhotons_coll = 0;
phot_death_counter = 0;

%alpha is absorption coefficient with units of cm^-1
alpha = alphavals(b);
path_length = L(m)./gridsize;

perc_abs_frac = alpha.*path_length;

% get locations of photons initially
ind = randi((gridsize.^2).*4, numPhotons_init, 1);
meshsize = [gridsize, gridsize,4];
[row,col,dir] = ind2sub(meshsize, ind);

phot_loc = zeros(gridsize, gridsize,4);

% add photons to grid initially
for i = 1:numPhotons_init
    phot_loc(row(i),col(i),(dir(i))) = phot_loc(row(i),col(i),dir(i))+1;
end

stepcounter = 0;
%% check
% check that num of photons is correct
A = sum(phot_loc, "all"); % correct woooooo

%direction is the 3rd dimension of the phot_loc matrix
%1 = up
%2 = down
%3 = left
%4 = right

%% monte carlo simulation
while sum(phot_loc,"all")~=0
    for i = 1:gridsize
        for j = 1:gridsize
            if (i==1)&&(j==1)
                % top left corner
                for k = 1:4
                    num_phot_here = phot_loc(i,j,k);
                    for d=1:num_phot_here
                        if k==1 || k==3
                            phot_loc(i,j,k)=phot_loc(i,j,k)-1;
                            numPhotons_coll = numPhotons_coll+1;
                        else
                            prob = rand(1,1);
                            if (prob>perc_abs_frac)&&(prob<=filter_reflectivity)
                                if k == 4
                                    phot_loc(i,j,k)=phot_loc(i,j,k)-1;
                                    phot_loc(i,j+1,k)=phot_loc(i,j+1,k)+1;
                                else
                                    phot_loc(i,j,k)=phot_loc(i,j,k)-1;
                                    phot_loc(i+1,j,k)=phot_loc(i+1,j,k)+1;
                                end
```

```
                            elseif
prob<=perc_abs_frac.*QY*trap_eff*filter_reflectivity
                                probmove = randi(2,1,1);
                                if probmove == 2
                                    phot_loc(i,j,k)=phot_loc(i,j,k)-1;
                                    phot_loc(i,j+1,4)=phot_loc(i,j+1,4)+1;
                                else
                                    phot_loc(i,j,k)=phot_loc(i,j,k)-1;
                                    phot_loc(i+1,j,2)=phot_loc(i+1,j,2)+1;
                                end
                            else
                                phot_loc(i,j,k)=phot_loc(i,j,k)-1;
                                phot_death_counter = phot_death_counter+1;
                            end
                        end
                    end
                end
            elseif (i==1)&&(j==gridsize)
                %top right corner
                for k = 1:4
                    num_phot_here = phot_loc(i,j,k);
                    for d=1:num_phot_here
                        if k==1 || k==4
                            phot_loc(i,j,k)=phot_loc(i,j,k)-1;
                            numPhotons_coll = numPhotons_coll+1;
                        else
                            prob = rand(1,1);
                            if (prob>perc_abs_frac)&&(prob<=filter_reflectivity)

                                if k == 3
                                    phot_loc(i,j,k)=phot_loc(i,j,k)-1;
                                    phot_loc(i,j-1,k)=phot_loc(i,j-1,k)+1;
                                else
                                    phot_loc(i,j,k)=phot_loc(i,j,k)-1;
                                    phot_loc(i+1,j,k)=phot_loc(i+1,j,k)+1;
                                end
                            elseif
prob<=perc_abs_frac.*QY*trap_eff*filter_reflectivity
                                probmove = randi(2,1,1);
                                if probmove == 2
                                    phot_loc(i,j,k)=phot_loc(i,j,k)-1;
                                    phot_loc(i,j-1,3)=phot_loc(i,j-1,3)+1;
                                else
                                    phot_loc(i,j,k)=phot_loc(i,j,k)-1;
                                    phot_loc(i+1,j,2)=phot_loc(i+1,j,2)+1;
                                end
                            else
                                phot_loc(i,j,k)=phot_loc(i,j,k)-1;
                                phot_death_counter = phot_death_counter+1;
                            end
                        end
                    end
                end
            elseif (i==gridsize)&&(j==1)
                %bottom left corner
```

```
                for k = 1:4
                    num_phot_here = phot_loc(i,j,k);
                    for d=1:num_phot_here
                        if k==2 || k==3
                            phot_loc(i,j,k)=phot_loc(i,j,k)-1;
                            numPhotons_coll = numPhotons_coll+1;
                        else
                            prob = rand(1,1);
                            if (prob>perc_abs_frac)&&(prob<=filter_reflectivity)

                                if k == 4
                                    phot_loc(i,j,k)=phot_loc(i,j,k)-1;
                                    phot_loc(i,j+1,k)=phot_loc(i,j+1,k)+1;
                                else
                                    phot_loc(i,j,k)=phot_loc(i,j,k)-1;
                                    phot_loc(i-1,j,k)=phot_loc(i-1,j,k)+1;
                                end
                            elseif
prob<=perc_abs_frac.*QY*trap_eff*filter_reflectivity
                                probmove = randi(2,1,1);
                                if probmove == 2
                                    phot_loc(i,j,k)=phot_loc(i,j,k)-1;
                                    phot_loc(i,j+1,4)=phot_loc(i,j+1,4)+1;
                                else
                                    phot_loc(i,j,k)=phot_loc(i,j,k)-1;
                                    phot_loc(i-1,j,1)=phot_loc(i-1,j,1)+1;
                                end
                            else
                                phot_loc(i,j,k)=phot_loc(i,j,k)-1;
                                phot_death_counter = phot_death_counter+1;
                            end
                        end
                    end
                end
            elseif (i==gridsize)&&(j==gridsize)
                % bottom right corner
                for k = 1:4
                    num_phot_here = phot_loc(i,j,k);
                    for d=1:num_phot_here
                        if k==2 || k==4
                            phot_loc(i,j,k)=phot_loc(i,j,k)-1;
                            numPhotons_coll = numPhotons_coll+1;
                        else
                            prob = rand(1,1);
                            if (prob>perc_abs_frac)&&(prob<=filter_reflectivity)
                                if k == 3
                                    phot_loc(i,j,k)=phot_loc(i,j,k)-1;
                                    phot_loc(i,j-1,k)=phot_loc(i,j-1,k)+1;
                                else
                                    phot_loc(i,j,k)=phot_loc(i,j,k)-1;
                                    phot_loc(i-1,j,k)=phot_loc(i-1,j,k)+1;
                                end
                            elseif
prob<=perc_abs_frac.*QY*trap_eff*filter_reflectivity
                                probmove = randi(2,1,1);
```

```
                                if probmove == 2
                                    phot_loc(i,j,k)=phot_loc(i,j,k)-1;
                                    phot_loc(i,j-1,3)=phot_loc(i,j-1,3)+1;
                                else
                                    phot_loc(i,j,k)=phot_loc(i,j,k)-1;
                                    phot_loc(i-1,j,1)=phot_loc(i-1,j,1)+1;
                                end
                            else
                                phot_loc(i,j,k)=phot_loc(i,j,k)-1;
                                phot_death_counter = phot_death_counter+1;
                            end
                        end
                    end
                elseif (i==1)
                    %top edge
                    for k = 1:4
                        num_phot_here = phot_loc(i,j,k);
                        for d=1:num_phot_here
                            if k==1
                                phot_loc(i,j,k)=phot_loc(i,j,k)-1;
                                numPhotons_coll = numPhotons_coll+1;
                            else
                                prob = rand(1,1);
                                if (prob>perc_abs_frac)&&(prob<=filter_reflectivity)
                                    if k == 4
                                        phot_loc(i,j,k)=phot_loc(i,j,k)-1;
                                        phot_loc(i,j+1,k)=phot_loc(i,j+1,k)+1;
                                    elseif k == 2
                                        phot_loc(i,j,k)=phot_loc(i,j,k)-1;
                                        phot_loc(i+1,j,k)=phot_loc(i+1,j,k)+1;
                                    else
                                        phot_loc(i,j,k)=phot_loc(i,j,k)-1;
                                        phot_loc(i,j-1,k)=phot_loc(i,j-1,k)+1;
                                    end
                                elseif
prob<=perc_abs_frac.*QY*trap_eff*filter_reflectivity
                                    probmove = randi(3,1,1);
                                    if probmove == 4
                                        phot_loc(i,j,k)=phot_loc(i,j,k)-1;
                                        phot_loc(i,j+1,2)=phot_loc(i,j+1,2)+1;
                                    elseif probmove == 2
                                        phot_loc(i,j,k)=phot_loc(i,j,k)-1;
                                        phot_loc(i+1,j,3)=phot_loc(i+1,j,3)+1;
                                    else
                                        phot_loc(i,j,k)=phot_loc(i,j,k)-1;
                                        phot_loc(i,j-1,3)=phot_loc(i,j-1,3)+1;
                                    end

                                else
                                    phot_loc(i,j,k)=phot_loc(i,j,k)-1;
                                    phot_death_counter = phot_death_counter+1;
                                end
                            end
                        end
```

```
                end
            elseif (i==gridsize)
                %bottom edge
                for k = 1:4
                    num_phot_here = phot_loc(i,j,k);
                    for d=1:num_phot_here
                        if k==2
                            phot_loc(i,j,k)=phot_loc(i,j,k)-1;
                            numPhotons_coll = numPhotons_coll+1;
                        else
                            prob = rand(1,1);
                            if (prob>perc_abs_frac)&&(prob<=filter_reflectivity)
                                if k == 4
                                    phot_loc(i,j,k)=phot_loc(i,j,k)-1;
                                    phot_loc(i,j+1,k)=phot_loc(i,j+1,k)+1;
                                elseif k == 1
                                    phot_loc(i,j,k)=phot_loc(i,j,k)-1;
                                    phot_loc(i-1,j,k)=phot_loc(i-1,j,k)+1;
                                else
                                    phot_loc(i,j,k)=phot_loc(i,j,k)-1;
                                    phot_loc(i,j-1,k)=phot_loc(i,j-1,k)+1;
                                end
                            elseif
prob<=perc_abs_frac.*QY*trap_eff*filter_reflectivity
                                probmove = randi(3,1,1);
                                if probmove == 4
                                    phot_loc(i,j,k)=phot_loc(i,j,k)-1;
                                    phot_loc(i,j+1,4)=phot_loc(i,j+1,4)+1;
                                elseif probmove == 1
                                    phot_loc(i,j,k)=phot_loc(i,j,k)-1;
                                    phot_loc(i-1,j,1)=phot_loc(i-1,j,1)+1;
                                else
                                    phot_loc(i,j,k)=phot_loc(i,j,k)-1;
                                    phot_loc(i,j-1,3)=phot_loc(i,j-1,3)+1;
                                end
                            else
                                phot_loc(i,j,k)=phot_loc(i,j,k)-1;
                                phot_death_counter = phot_death_counter+1;
                            end
                        end
                    end
                end
            elseif (j==1)
                %left edge
                for k = 1:4
                    num_phot_here = phot_loc(i,j,k);
                    for d=1:num_phot_here
                        if k==3
                            phot_loc(i,j,k)=phot_loc(i,j,k)-1;
                            numPhotons_coll = numPhotons_coll+1;
                        else
                            prob = rand(1,1);
                            if (prob>perc_abs_frac)&&(prob<=filter_reflectivity)
                                if k == 4
                                    phot_loc(i,j,k)=phot_loc(i,j,k)-1;
```

```
                                    phot_loc(i,j+1,k)=phot_loc(i,j+1,k)+1;
                                elseif k == 1
                                    phot_loc(i,j,k)=phot_loc(i,j,k)-1;
                                    phot_loc(i-1,j,k)=phot_loc(i-1,j,k)+1;
                                else
                                    phot_loc(i,j,k)=phot_loc(i,j,k)-1;
                                    phot_loc(i+1,j,k)=phot_loc(i+1,j,k)+1;
                                end
                            elseif
prob<=perc_abs_frac.*QY*trap_eff*filter_reflectivity
                                probmove = randi(3,1,1);
                                if probmove == 4
                                    phot_loc(i,j,k)=phot_loc(i,j,k)-1;
                                    phot_loc(i,j+1,4)=phot_loc(i,j+1,4)+1;
                                elseif probmove == 1
                                    phot_loc(i,j,k)=phot_loc(i,j,k)-1;
                                    phot_loc(i-1,j,1)=phot_loc(i-1,j,1)+1;
                                else
                                    phot_loc(i,j,k)=phot_loc(i,j,k)-1;
                                    phot_loc(i+1,j,2)=phot_loc(i+1,j,2)+1;
                                end

                            else
                                phot_loc(i,j,k)=phot_loc(i,j,k)-1;
                                phot_death_counter = phot_death_counter+1;
                            end
                        end
                    end
                end
            elseif (j==gridsize)
                %right edge
                for k = 1:4
                    num_phot_here = phot_loc(i,j,k);
                    for d=1:num_phot_here
                        if k==4
                            phot_loc(i,j,k)=phot_loc(i,j,k)-1;
                            numPhotons_coll = numPhotons_coll+1;
                        else
                            prob = rand(1,1);
                            if (prob>perc_abs_frac)&&(prob<=filter_reflectivity)

                                if k == 3
                                    phot_loc(i,j,k)=phot_loc(i,j,k)-1;
                                    phot_loc(i,j-1,k)=phot_loc(i,j-1,k)+1;
                                elseif k == 1
                                    phot_loc(i,j,k)=phot_loc(i,j,k)-1;
                                    phot_loc(i-1,j,k)=phot_loc(i-1,j,k)+1;
                                else
                                    phot_loc(i,j,k)=phot_loc(i,j,k)-1;
                                    phot_loc(i+1,j,k)=phot_loc(i+1,j,k)+1;
                                end
                            elseif
prob<=perc_abs_frac.*QY*trap_eff*filter_reflectivity
                                probmove = randi(3,1,1);
                                if probmove == 3
```

```
                        phot_loc(i,j,k)=phot_loc(i,j,k)-1;
                        phot_loc(i,j-1,3)=phot_loc(i,j-1,3)+1;
                    elseif probmove == 1
                        phot_loc(i,j,k)=phot_loc(i,j,k)-1;
                        phot_loc(i-1,j,1)=phot_loc(i-1,j,1)+1;
                    else
                        phot_loc(i,j,k)=phot_loc(i,j,k)-1;
                        phot_loc(i+1,j,2)=phot_loc(i+1,j,2)+1;
                    end

                else
                    phot_loc(i,j,k)=phot_loc(i,j,k)-1;
                    phot_death_counter = phot_death_counter+1;
                end
            end
        end
    end
else
    %center
    for k = 1:4
        num_phot_here = phot_loc(i,j,k);
        for d=1:num_phot_here
            prob = rand(1,1);
            if (prob>perc_abs_frac)&&(prob<=filter_reflectivity)
                if k == 3
                    phot_loc(i,j,k)=phot_loc(i,j,k)-1;
                    phot_loc(i,j-1,k)=phot_loc(i,j-1,k)+1;
                elseif k == 1
                    phot_loc(i,j,k)=phot_loc(i,j,k)-1;
                    phot_loc(i-1,j,k)=phot_loc(i-1,j,k)+1;
                elseif k == 4
                    phot_loc(i,j,k)=phot_loc(i,j,k)-1;
                    phot_loc(i,j+1,k)=phot_loc(i,j+1,k)+1;
                else
                    phot_loc(i,j,k)=phot_loc(i,j,k)-1;
                    phot_loc(i+1,j,k)=phot_loc(i+1,j,k)+1;
                end
            elseif (prob<=perc_abs_frac.*QY*trap_eff*filter_reflectivity)
                probmove = randi(4,1,1);
                if probmove == 3
                    phot_loc(i,j,k)=phot_loc(i,j,k)-1;
                    phot_loc(i,j-1,3)=phot_loc(i,j-1,3)+1;
                elseif probmove == 1
                    phot_loc(i,j,k)=phot_loc(i,j,k)-1;
                    phot_loc(i-1,j,1)=phot_loc(i-1,j,1)+1;
                elseif probmove == 4
                    phot_loc(i,j,k)=phot_loc(i,j,k)-1;
                    phot_loc(i,j+1,4)=phot_loc(i,j+1,4)+1;
                else
                    phot_loc(i,j,k)=phot_loc(i,j,k)-1;
                    phot_loc(i+1,j,2)=phot_loc(i+1,j,2)+1;
                end

            else
                phot_loc(i,j,k)=phot_loc(i,j,k)-1;
```

```
                            phot_death_counter = phot_death_counter+1;
                        end
                    end
                end

            end
        end
    end
end



%% concentration calculation
geom_conc = L(m)./(4.*thick);

optical_eff = numPhotons_coll/numPhotons_init;

concentration(b,a,m,n) = optical_eff.*geom_conc;
grid_optical_eff(b,a,m,n)= optical_eff;

geom_conc_vals(m) = geom_conc;


end
end
end
end
```

APPENDIX B: SUPPLEMENTAL INFORMATION FOR CHAPTER III—TUNABLE ANGULAR LIGHT EMISSION OF LEAD HALIDE PEROVSKITE NANOCRYSTAL THIN FILMS VIA SOLUTION-PROCESSED SUBSTRATE TREATMENT

Materials

Lead (II) bromide ($PbBr_2$, 99.999%, Sigma Aldrich), cesium carbonate (Cs_2CO_3, 99.9%, Sigma Aldrich), 1-octyl phosphonic acid (OPA, 99%, Thermo Scientific), trioctylphosphine oxide (TOPO, 99% Sigma Aldrich), didecyldimethyl ammonium bromide (DDAB, >98%, TCI), methyl acetate (MeAc, 99.5%, Sigma Aldrich), toluene (99.8%, Sigma Aldrich), heptane (99%, Sigma Aldrich), N,N-dimethyl formamide (DMF, 99.8%, Sigma Aldrich), oleylamine (OAm, technical grade 70%, Sigma Aldrich), Cesium bromide (CsBr, 99.999%, Sigma Aldrich), hydrobromic acid (HBr, 48 wt.% in H_2O, ≥99.99%, Sigma Aldrich), hexane (≥95%, Sigma Aldrich), oleic acid (OA, 90%, Sigma Aldrich) and ethanol (≥99.5%, Sigma Aldrich) were used without further purification.

Nanocube Synthesis

Procedure was adapted from Brown et al. [124]

Cs-octanoate precursor: 326 mg Cs_2CO_3 was added to 10 mL OctAc and vortexed until dissolved.

Pb precursor: 500 mg $PbBr_2$ was added to 10 mL toluene along with 5.8 g TOPO and heated to 80 °C while stirring until completely dissolved (around 15 minutes). Solution was allowed to cool completely to room temperature before use.

DDAB precursor: 233 mg DDAB was added to 10 mL toluene and vortexed until dissolved.

Synthesis: Under constant stirring, 2 mL of Pb precursor was added to round bottom flask. 233 mg of OPA was added and stirred at room temperature until dissolved to create a ligand concentration of 0.6 mM. In air and at room temperature, 220 µL Cs-octanoate precursor was injected, and the reaction was allowed to proceed for 30 seconds. 624 µL DDAB precursor was added, and the product was allowed to continue stirring for 5 minutes.

Cleaning: First 6 mL MeAc was added to the crude solution to clean the particles. The product was divided between 3 centrifuge tubes and centrifuged for 20 minutes at 10,000 rpm (12298 g). The precipitate was retained and redispersed in 150 μL heptane per tube to then perform a knockout step. The three tubes were centrifuged for 1 minute at 5000 rpm (3354 g), and the supernatant was retained as product.

Nanoplate Synthesis

Procedure was adapted from Pan et al. [125]

Pb precursor: 367 mg $PbBr_2$ was added to 2 mL DMF along with 2 mL OAm and stirred at room temperature to dissolve.

CsBr precursor: 213 mg CsBr was added to 1 mL HBr and vortexed until dissolved.

Synthesis: Under constant stirring, 5 mL hexane and 10 μL OA was added to a round bottom flask, and 200 μL Pb precursor was added. 50 μL CsBr precursor was injected then the reaction was immediately quenched by injection of 200 μL ethanol.

Cleaning: Crude product was divided into two centrifuge tubes and centrifuged for 10 minutes at 10,000 rpm (12298 g). An immiscible bilayer of two supernatants was observed and the less dense nanoplate-containing non-polar supernatant was retained as product.

Transmission Electron Microscopy

Images were collected on a FEI Tecnai T12 microscope. Nanocubes were diluted 50x after synthesis and drop cast onto a 400 μm carbon coated copper grid. Nanoplates were diluted 10x after synthesis and drop cast onto a 400 μm carbon coated copper grid.

TEM images in figure S1 were used to estimate nanoparticle packing in order to determine the effective film RI via Bruggeman Effective Medium Approximation as was done by Jurow et al. [53] After smoothing, despeckling, and increasing the contrast using ImageJ, nanocrystal was estimated at 55% of the area, the average of six selected representative regions of best resolution and close-packed monolayer. Perovskite nanocrystal has an RI of 2.3.[26] Space between particles comprising 45% of the area was presumed to be ligand with an RI of 1.45. [153]

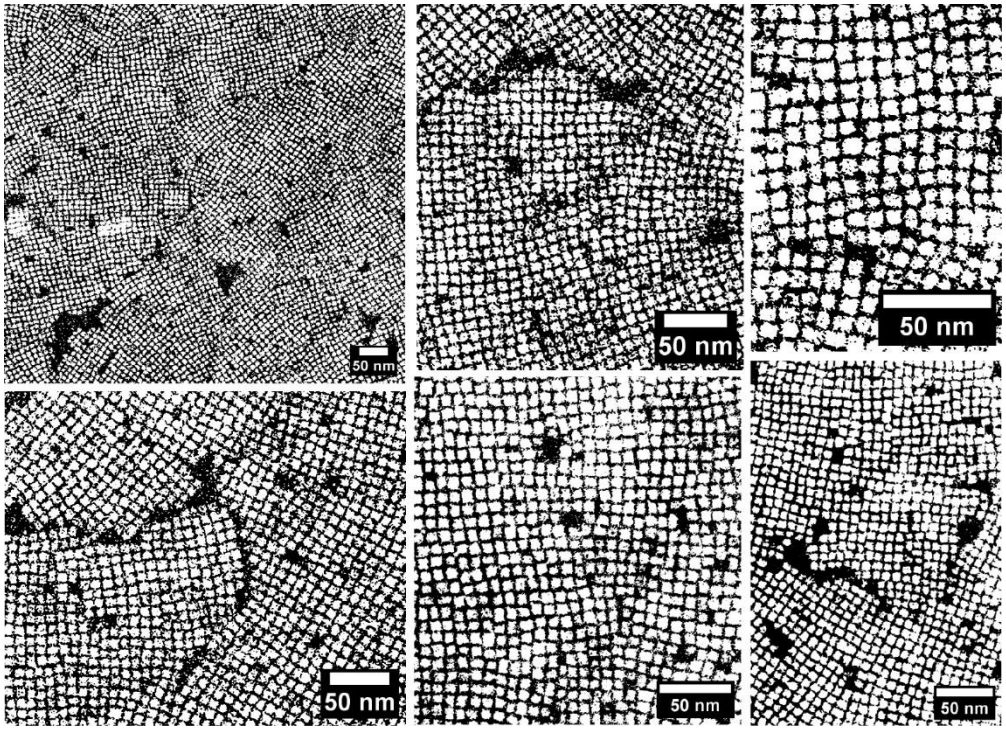

Figure B.1. Contrast-enhanced TEM images used for effective medium approximation. White pixels are counted as nanocrystal area and black pixels are counted as ligand area.

The effective RI of the film was thereby estimated by the following equation:

$$RI = Packing\ Fraction_1(RI_1) + Packing\ Fraction_2(RI_2)$$

$$RI = 0.55(2.3) + 0.45(1.45) = 1.92$$

Assessing the packing fraction over a larger sample area is reflective of close packing and any larger gaps that form; hence, as expected, we calculate a smaller packing fraction that literature previously reports (70%) [53]. The estimated RI was used in modeling the angular emission signal for a given transition dipole moment angle.

UV-vis Spectrophotometry

Absorbance and relative photoluminescence spectra were collected using a Stellarnet BLACK-Comet UV-vis reconfigurable spectrometer. For colloidal absorbance and PL measurements, a broad-spectrum Stellarnet SL-5 Halogen/Deuterium light source is used for absorbance measurements, and a 392

nm LED light source 90° from the detector is used for photoluminescence measurements. A StarnaCells quartz cuvette with a path length of 1cm was used. For film PL spectra, a 405 nm CW laser (30mA, 149.34 mW) was used to excite thin film samples mounted on a glass slide and a Chroma AT435LP 435 nm longpass filter was used as the laser was mounted normal to the plane of detection.

Thin Film Deposition

For caustic-treated glass or silicon substrates, 0.16 - 0.19 mm-thick Corning borosilicate coverslips or silcon wafers were placed in a 1M potassium hydroxide in 80% ethanol base bath (pH ~11-12) for two hours then removed and rinsed thoroughly with DI water followed by ethanol before being allowed to dry in the oven. Untreated coverslips or wafers were inspected to be free of dust before deposition.

Polymer films were made via spin coating 100 μL of 20 mg/mL PMMA solution in toluene onto glass coverslips or silicon wafers at 4000 rpm for 45 seconds.

Nanoplate films were made via spin coating 100 μL of the obtained colloidal product onto glass coverslips or silicon wafers at 6000 rpm for 45 seconds. For nanoplate films that would not receive an additional deposition of nanocubes, 100 μL heptane was spun onto dried films at 1500 rpm for 45 seconds to simulate any rinsing effects of adding another layer.

Nanocube films were made via spin coating 100 μL of colloidal product diluted 50x in heptane onto glass coverslips or silicon wafers at 1500 rpm for 45 seconds.

Atomic Force Microscopy

Measurements were collected using a Bruker Dimension FastScan Atomic Force Microscope in ScanAsyst mode. A ScanAsyst-Air-HPI probe was used, and measurements were taken from films deposited on silicon substrates.

To determine the thickness of the polymer layer, scores were made along samples using a razor blade and the interface was scanned. Gwyddion was used for image analysis. After plane-leveling the image and aligning rows, a difference was taken of the average height far from the interface on the polymer and scored region.

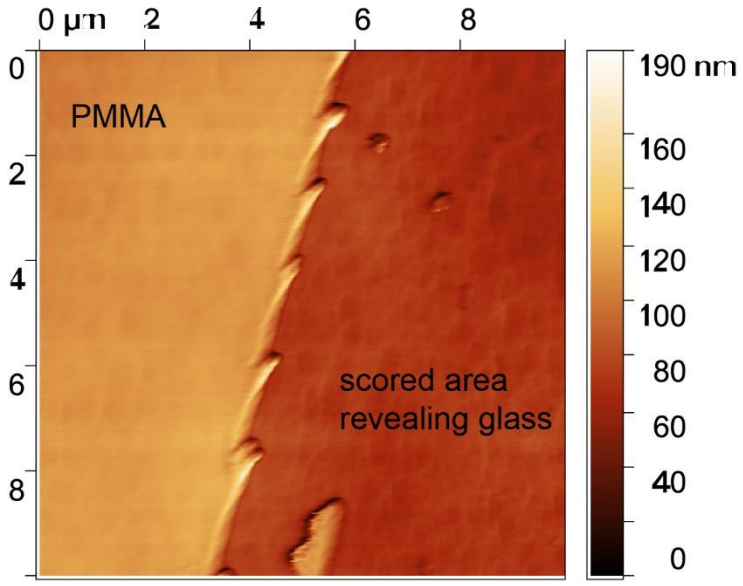

Figure B.2. AFM images used in verifying the thickness of PMMA

Back Focal Plane Fluorescence Microscopy (BFPFM)

Thin film samples on a glass coverslip mounted face down were measured to determine the angular emission pattern at the air-glass interface.

A home-built inverted fluorescence microscope was used, including a Back Focal Plane imaging mode according to the procedure described in Kurvits et al. [68]. Excitation was done by a ThorLabs LP405-SF10 405 nm laser diode (24 mA, 0.8 mW). This laser diode was collimated using a Thor Labs F810FC-405 collimation package and then expanded using a ThorLabs GBE02-A beam expander. A Semrock Di02-R405-25x36 25.2mm x 35.6 mm dichroic beamsplitter was used to direct the laser to the objective and minimize the transmission of any reflected laser light off the sample to the detector camera. The sample was excited through a UPlanSApo Olympus 100x oil-immersion objective (NA=1.45, Immersion Oil type F), by which the laser beam was focused to a diffraction-limited spot.

Fluorescence from the sample was collected by the objective and then passed through a tube lens (Thorlabs TTL180-A, f=180mm) to focus the signal onto a CCD camera for collection (Andor iXon Ultra 888 EMCCD). Additional filters (Chroma AT435LP 435 nm longpass filter, ThorLabs FELH0500 500 nm

longpass filter) were placed before the camera to help cut out any remaining laser signal (435 nm longpass) and eliminate any signal from the 462-489 nm emitting nanoplates (500 nm longpass).

To transform the setup from fluorescence imaging into Back Focal Plane imaging, a Bertrand lens (Thorlabs AC254-400-A-ML achromatic doublet) was placed between the beam splitter and tube lens as this changes the focal plane from the real-space sample to the Back Focal Plane within the objective, creating a projection of the 3D angular emission pattern on the camera [68]. A linear polarizer (Thorlabs LPVISE100-A) was also added after the beamsplitter to polarize the Back Focal Plane image and simplify the extraction of the transition dipole moment angle. All BFP images were generated using 1s exposure times. 5 images were collected at 5 locations across the sample, or 25 images per sample.

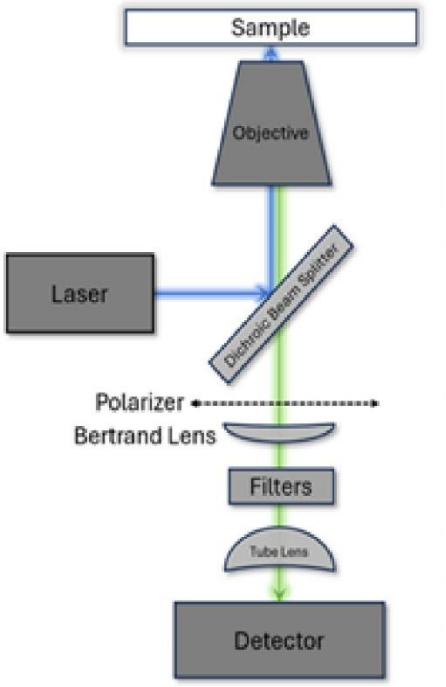

Figure B.3. Schematic of Back Focal Plane microscope. Adapted from Russ et al. [72]

Modeling Angle-Resolved Light Emission to Extract Effective Transition Dipole Moment

The dipole orientation factor (Θ) is the relative dipole strength (*p*) of in-plane or parallel dipoles to all dipoles: [69]

$$\Theta = \frac{p_{\parallel}}{p_{\parallel}+p_{\perp}} \tag{1.1}$$

The orientation factor and effective transition dipole moment (TDM) are related by[64]

$$TDM = arccos(\sqrt{\Theta}) \tag{1.2}$$

The angular light emission pattern from these dipoles within a thin film can be described by a three layer model where the top layer (n_1) is air, the middle layer (n_2) is the emissive film, and the bottom layer (n_3) is the glass substrate. [22,66,70,71] The horizontal dipole contribution along x is eliminated by linear polarizer in experiment, which allows us to decouple horizontal and vertical dipole contributions when fitting to experimental data. Polarized light emission intensity projected onto a 2-D collection plane (N_{pol}) as a function of photon momentum vectors along the x- and y-directions (k_x, k_y) is defined as:[67,71]

$$N^{pol}(k_x, k_y) = C\left[\frac{1}{2}\left(\rho_{IP}^{p} + \rho_{IP}^{s}\right)\cos^2(TDM) \ + \rho_{OP}^{p}\sin^2(TDM)\right] \tag{1.3}$$

or, in terms of orientation factor:

$$N^{pol}(k_x, k_y) = C\left[\frac{1}{2}\left(\rho_{IP}^{p} + \rho_{IP}^{s}\right)\Theta \ + \rho_{OP}^{p}(1-\Theta)\right] \tag{1.4}$$

where C is a normalization constant. ρ_{ip}^{s}, ρ_{ip}^{p}, ρ_{op}^{p} are photonic density of states in the *s*- and *p*-polarized, in-plane and out-of-plane directions governed by the thickness, refractive index, and emission wavelength of the emissive layer. Density of states in each direction are given by:

$$\rho_{IP}^{s} = \rho_{y}^{s}(k_x, k_y) = \left(\frac{1}{8\pi k_0^2}\right)\left(\frac{k_0}{k_{z,3}}\right)\left|\frac{t_{32}^{s} e^{\frac{ik_{z,2}D}{2}}\left(1+r_{21}^{s} e^{ik_{z,2}D}\right)}{1-r_{21}^{s} r_{23}^{s} e^{2ik_{z,2}D}} \frac{k_y}{\sqrt{k_x^2+k_y^2}}\right|^2 \quad (1.5)$$

$$\rho_{IP}^{p} = \rho_{x}^{p}(k_x, k_y) = \left(\frac{1}{8\pi k_0^2}\right)\left(\frac{k_0}{k_{z,3}}\right)\left|\frac{t_{32}^{p} e^{\frac{ik_{z,2}D}{2}}\left(1-r_{21}^{p} e^{ik_{z,2}D}\right)\frac{k_{z,2}}{n_2 k_0}}{1-r_{21}^{p} r_{23}^{p} e^{2ik_{z,2}D}} \frac{k_x}{\sqrt{k_x^2+k_y^2}}\right|^2 \quad (1.6)$$

$$\rho_{OP}^{p} = \rho_{z}^{s}(k_x, k_y) = \left(\frac{1}{8\pi k_0^2}\right)\left(\frac{k_0}{k_{z,3}}\right)\left|\frac{t_{32}^{p} e^{\frac{ik_{z,2}D}{2}}\left(1+r_{21}^{p} e^{ik_{z,2}D}\right)\frac{k_x}{n_2 k_0}}{1-r_{21}^{p} r_{23}^{p} e^{2ik_{z,2}D}}\right|^2 \quad (1.7)$$

where

$$k_{z,i} = \sqrt{n_i^2 k_0^2 - \left(k_x^2 + k_y^2\right)} \quad (1.8)$$

$$k_0 = \frac{2\pi}{\lambda} \quad (1.9)$$

λ is the wavelength of the emitted light, n_i is the refractive index of layer i, t_{ij}^{l} and r_{ij}^{l} are the Fresnel transmission and reflection coefficients between layers *i* and *j* for *l*-polarized light, and *D* is the thickness of the emissive layer. The Fresnel coefficients for s and p polarized light are given by[22,66]

$$t_{ij}^{p} = \frac{2n_i n_j k_{zi}}{n_j^2 k_{zi} + n_i^2 k_{zj}};\ t_{ij}^{s} = \frac{2k_{zi}}{k_{zi}+k_{zj}};\ r_{ij}^{p} = \frac{n_j^2 k_{zi} - n_i^2 k_{zj}}{n_j^2 k_{zi} + n_i^2 k_{zj}};\ r_{ij}^{p} = \frac{k_{zi}-k_{zj}}{k_{zi}+k_{zj}} \quad (1.10)$$

We note that light emission in polar coordinates ($N^{pol}(\theta, \phi)$), where θ is the polar angle and ϕ is the azimuthal angle, is related to light emission in k-space by

$$k_x = k_0 n_3 \, sin \, sin \, (\phi) \;\; sin \, sin \, (\theta) \, ; k_y = k_0 n_3 \, sin \, sin \, (\phi) \;\; cos \, cos \, (\theta) \qquad (1.11)$$

This model for emission signal is compared to our measured BFPFM data, and the effective TDM of best fit is determined by $\chi 2$ minimization according to the procedure described in Russ et al.[72]

APPENDIX C: SUPPLEMENTAL INFORMATION FOR CHAPTER IV—ORIENTED DIPOLES IN ORDERED ENSEMBLES OF CONFINED LEAD HALIDE PEROVSKITE NANOCRYSTALS

Materials

Lead (II) bromide ($PbBr_2$, 99.999%, Sigma Aldrich), cesium carbonate (Cs_2CO_3, 99%, Sigma Aldrich), oleic acid (OA, technical grade 90%, Sigma Aldrich), oleylamine (OAm, technical grade 70%, Sigma Aldrich), Mesitylene (99%, Sigma Aldrich), hexane (anhydrous, ≥99%, Sigma Aldrich), ethyl acetate (anhydrous 99.8%, Sigma Aldrich), octanoic acid (OctAc, ≥98%%, Sigma Aldrich), 1-octyl phosphonic acid (OPA, 99%, Thermo Scientific), trioctylphosphine oxide (TOPO, 99% Thermo Scientific), didecyldimethyl ammonium bromide (DDAB, >98%, TCI), methyl acetate (MeAc, 99.5%, Sigma Aldrich), toluene (99.8%, Sigma Aldrich), heptane (99%, Sigma Aldrich), and Glyceryl triacetate (≥99.0%, Sigma Aldrich) were used without further purification.

Nanoplate Synthesis

Procedure was adapted from Kovalenko et al. [55] and Bekenstein et al.[19]

Cs-oleate precursor: 0.4 g Cs_2CO_3 was added to a round bottom flask along with 1.2 mL OA and 15 mL ODE. Flask was connected to the Schlenk line and degassed under vacuum for 1 hr at 100 °C, then switched to Ar and heated at 120 °C until all Cs_2CO_3 was dissolved and solution was brown in color, indicating that it had all reacted with OA.

Synthesis: 0.069 g $PbBr_2$ added to a 25 mL round bottom flask along with 5 mL mesitylene. Flask was connected to the Schlenk line and degassed at room temperature. Flask was then switched to Ar and heated to 100 °C, followed by the injection of 0.5 mL OA and 0.5 mL OAm. Once all $PbBr_2$ was dissolved, the temperature was changed to 99 °C, and 0.4 mL heated (to at least 100°C) Cs-oleate was injected into the PbBr2 precursor, and the reaction was immediately quenched with liquid nitrogen.

For a 2x scaled reaction, 0.138 g $PbBr_2$ was used, along with 1 mL OA and 1 mL OAm, 0.8 mL heated Cs-oleate. The injection was done at 125 °C.

Cleaning: Crude solution was divided into 3 tubes and centrifuged for 10 minutes at 11,000 rpm (14,881 g). Pellet was retained, and any supernatant that could not be sufficiently decanted by pipetting was gently removed using a cotton-tipped applicator. Pellet was redispersed in 100 μL hexane per tube and centrifuged again for 20 minutes at 11,000 rpm.

100 μL supernatant was added to two new tubes, along with 200 μL hexane and 600 μL ethyl acetate per tube. The tubes were centrifuged for 5 minutes at 11,000 rpm. Pellet was retained, and again any supernatant that could not be sufficiently decanted was removed using a cotton-tipped applicator. Pellet was redispersed in 100 μL hexane per tube and centrifuged again for 10 minutes at 11,000 rpm. The supernatant was filtered by a 0.22 μm nylon syringe filter and retained as product.

Transmission Electron Microscopy

Images were collected on a FEI Tecnai T12 microscope using 200 μm or 400 μm carbon coated copper grids.

TEM images in figure S1 were used to estimate nanoparticle packing in order to determine the effective film RI via Bruggeman Effective Medium Approximation as was done by Jurow et al. [53] For face down cases, after smoothing, despeckling, and increasing the contrast using ImageJ, nanoplate was estimated at 39% of the area, the average of three selected representative regions of best resolution. For edge up cases, nanoplate was estimated at 49% of the area. Perovskite nanocrystal has an RI of 2.3.[26] Space between particles comprising the remainder of the area was presumed to be ligand with an RI of 1.45. [153]

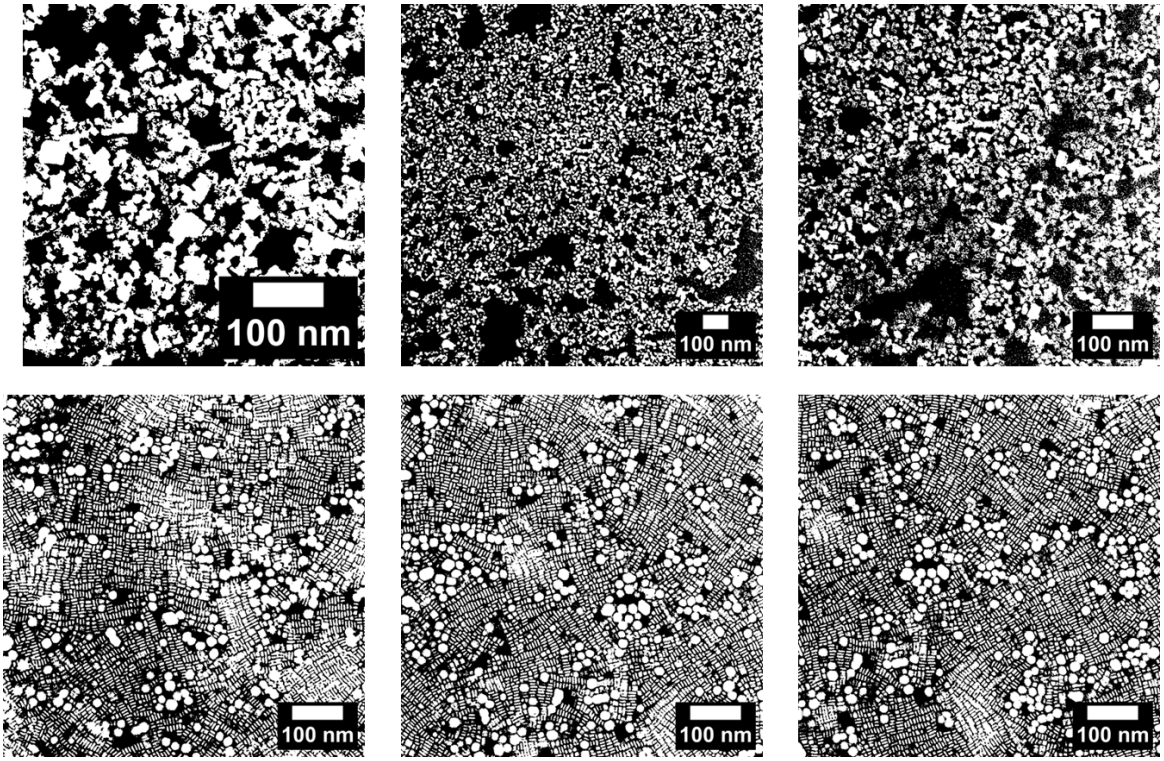

Figure C.1. Contrast-enhanced TEM images used for effective medium approximation. Top row is face down samples; bottom row is edge up samples. White pixels are counted as nanocrystal area and black pixels are counted as ligand area.

The effective RI of the film was thereby estimated by the following equation:

$$RI = Packing\ Fraction_1(RI_1) + Packing\ Fraction_2(RI_2)$$

$$RI_{face\ down} = 0.39(2.3) + 0.61(1.45) = 1.78$$

$$RI_{edge\ up} = 0.49(2.3) + 0.51(1.45) = 1.87$$

The estimated RI was used in modeling the angular emission signal for a given transition dipole moment angle.

UV-vis Spectrophotometry

Absorbance and relative photoluminescence spectra were collected using a Stellarnet BLACK-Comet UV-vis reconfigurable spectrometer. For colloidal absorbance and PL measurements, a broad-spectrum Stellarnet SL-5 Halogen/Deuterium light source is used for absorbance measurements, and a

392 nm LED light source 90° from the detector is used for photoluminescence measurements. A StarnaCells quartz cuvette with a path length of 1 cm was used. For film PL spectra, a 405 nm CW laser (44mA, 9 mW) was used to excite thin film samples mounted on a glass slide and a Thorlabs FEL0450 450 nm longpass filter was used as the laser was mounted normal to the plane of detection.

Sublayer screening

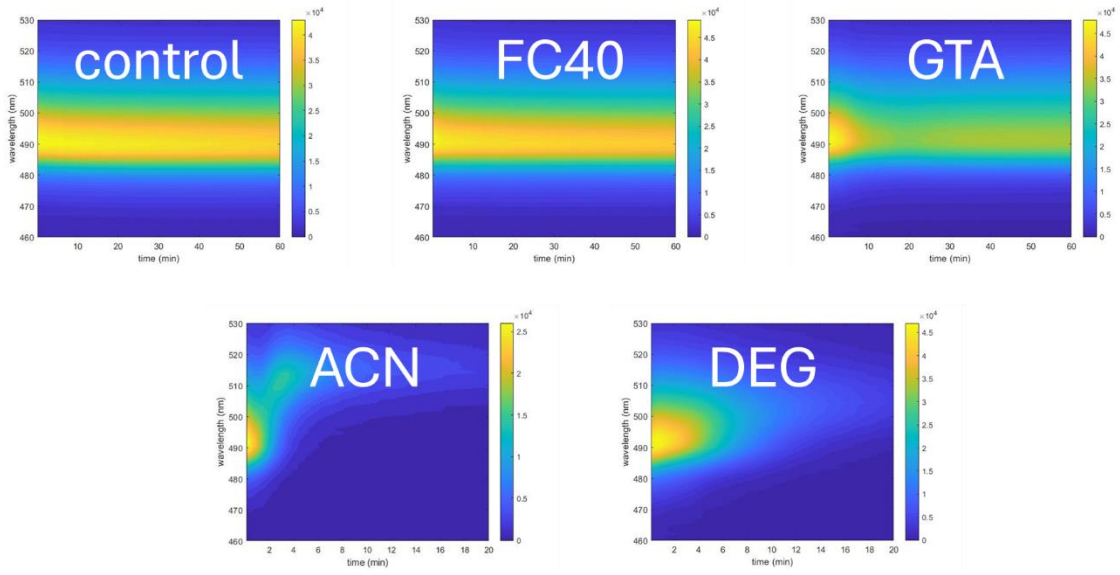

Figure C.2. Photoluminescence spectra over time for $CsPbBr_3$ nanoplates in hexane after the addition of immiscible sublayer candidate (1% by volume)

Thin Film Preparation via assembly at the liquid-air interface

Assembly at the liquid-air interface was done in glass petri dishes (60 mm diameter, 15 mm height). First, approximately 23 mL glyceryl triacetate (GTA) was added to the petri dish with the desired concentration of unbound ligand additive (0 to 0.68 mM OA and 0 to 0.66 mM OAm). We found that using higher concentrations of ligand (4x-10x) resulted in complete aggregation instead of a monolayer film. Then, a suspension of $CsPbBr_3$ nanoplates in hexane (dilution standardized to 1.75 OD at 335 nm, around 100x diluted for a typical synthesis) was deposited onto the surface of the GTA to form two phases and was quickly covered with the top of the petri dish until all hexane had completely evaporated.

The assembled film was transferred to the desired substrate by stamping the substrate onto the surface of the GTA. This was done using reverse action tweezers to hold TEM grids, or using wide mouth tweezers or a cover slip vacuum tool to hold cover slips. Once the films had been transferred to the substrates, substrates were dried under vacuum to remove any excess GTA that remained on the surface.

This method was extremely sensitive to competing forces or outside effects, so many steps were taken to minimize these occurrences. Petri dishes and substrates were inspected for dust and cleaned before use, and the surface of the sublayer was inspected for dust and stamped using a sacrificial cover slip to remove any microscopic contaminants on the liquid surface. Preparation was done inside an Ar glovebox, and glovebox filters were momentarily turned off during deposition of the nanoparticle suspension and substrate stamping to minimize movement of gas in the environment. Additionally, GTA was allowed to sit undisturbed for at least 1 minute before depositing the nanoparticles to minimize movement in the sublayer.

Figure C.3. Photos showing (a) the addition of nanoplate suspension onto GTA sublayer, (b) covered petri dish during evaporation of native solvent, and (c) coverslip vacuum tool used to aid in the even stamping of glass onto the liquid sublayer.

Atomic Force Microscopy

Measurements were collected using a Bruker Dimension FastScan Atomic Force Microscope in ScanAsyst mode. A ScanAsyst-Air-HPI probe was used.

To determine the thickness of the nanoplate assemblies, the image was plane-leveled, row-aligned, and masked via height threshold to isolate the islands of nanocubes from the background. The average height of the masked region was subtracted from the average height of the background.

Physical Properties Used in Fitting the Effective Transition Dipole Moment and Inherent Uncertainty of Fit

Table S1 gives the physical parameters used to model each sample condition when fitting TDM alignment.

Table C.1. Properties of emitting layer describing the BFP signal for each sample condition

	λ (nm)	**RI (TEM using EMA)**	**D (nm) (AFM)**	**D (nm) (TEM)**	**D (nm) (model input)**
100 µL, no OA	492	1.78	3.4	3.79±0.59	0
200 µL, 0.68 mM OA	492	1.87	15.2	13.8±2.7	15

Background signal noise across datasets had an estimated standard deviation of 2.31% which results in an associated inherent uncertainty of fit. According to the confidence intervals reported by Russ et al.,[72] the inherent uncertainty in the fit of our measurements given the thickness, RI of the emitting layer, and standard deviation of background noise levels is less than ±0.1°.

REFERENCES

(1) *Goals of the Solar Energy Technologies Office*. Energy.gov.

(2) *S.579 - Department of Energy Quantum Leadership Act of 2025*. Congress.gov.

(3) Hanifi, D. A.; Bronstein, N. D.; Koscher, B. A.; Nett, Z.; Swabeck, J. K.; Takano, K.; Schwartzberg, A. M.; Maserati, L.; Vandewal, K.; van de Burgt, Y.; Salleo, A.; Alivisatos, A. P. Redefining Near-Unity Luminescence in Quantum Dots with Photothermal Threshold Quantum Yield. *Science* **2019**, *363* (6432), 1199–1202. https://doi.org/10.1126/science.aat3803.

(4) Polman, A.; Atwater, H. A. Photonic Design Principles for Ultrahigh-Efficiency Photovoltaics. *Nat Mater* **2012**, *11* (3), 174–177. https://doi.org/10.1038/nmat3263.

(5) Gutmann, J.; Peters, M.; Bläsi, B.; Hermle, M.; Gombert, A.; Zappe, H.; Goldschmidt, J. C. Electromagnetic Simulations of a Photonic Luminescent Solar Concentrator. *Opt Express* **2012**, *20* (S2), A157–A167. https://doi.org/10.1364/OE.20.00A157.

(6) Yu, Z.; Raman, A.; Fan, S. Fundamental Limit of Nanophotonic Light Trapping in Solar Cells. *Proceedings of the National Academy of Sciences* **2010**, *107* (41), 17491–17496. https://doi.org/10.1073/pnas.1008296107.

(7) Zhang, Y.; Biswas, R. High Light Outcoupling Efficiency from Periodically Corrugated OLEDs. *ACS Omega* **2021**, *6* (13), 9291–9301. https://doi.org/10.1021/acsomega.1c00903.

(8) Marcato, T.; Kumar, S.; Shih, C.-J. Strategies for Controlling Emission Anisotropy in Lead Halide Perovskite Emitters for LED Outcoupling Enhancement. *Advanced Materials* **2024**, *n/a* (n/a), 2413622. https://doi.org/https://doi.org/10.1002/adma.202413622.

(9) Chen, W.; Chen, J.; Gu, L.; Huang, Z.; Ma, P.; Zhang, Y.; Liu, H.; Zhou, H.; Wang, N.; Wang, J.; Xiao, Z. Overcoming the Outcoupling Limit of Perovskite Light-Emitting Diodes with Artificially Formed Nanostructures. *Advanced Materials* **2022**, *34* (49), 2207180. https://doi.org/https://doi.org/10.1002/adma.202207180.

(10) Zou, C.; Lin, L. Y. Effect of Emitter Orientation on the Outcoupling Efficiency of Perovskite Light-Emitting Diodes. *Opt Lett* **2020**, *45* (17), 4786–4789. https://doi.org/10.1364/OL.400814.

(11) Mulder, C. L.; Reusswig, P. D.; Beyler, A. P.; Kim, H.; Rotschild, C.; Baldo, M. A. Dye Alignment in Luminescent Solar Concentrators: II. Horizontal Alignment for Energy Harvesting in Linear Polarizers. *Opt Express* **2010**, *18* (S1), A91–A99. https://doi.org/10.1364/OE.18.000A91.

(12) Green, M. A.; Dunlop, E. D.; Yoshita, M.; Kopidakis, N.; Bothe, K.; Siefer, G.; Hao, X.; Jiang, J. Y. Solar Cell Efficiency Tables (Version 65). *Progress in Photovoltaics: Research and Applications* **2025**, *33* (1), 3–15. https://doi.org/10.1002/pip.3867.

(13) Bronstein, N. D.; Yao, Y.; Xu, L.; O'Brien, E.; Powers, A. S.; Ferry, V. E.; Alivisatos, A. P.; Nuzzo, R. G. Quantum Dot Luminescent Concentrator Cavity Exhibiting 30-Fold Concentration. *ACS Photonics* **2015**, *2* (11), 1576–1583. https://doi.org/10.1021/acsphotonics.5b00334.

(14) Mulder, C. L.; Reusswig, P. D.; Velazquez, M.; Kim, H.; Rotschild, C.; Baldo, M. A. Dye Alignment in Luminescent Solar Concentrators: I Vertical Alignment for Improved Waveguide Coupling. *Opt Express* **2010**, *18* (S1), A79. https://doi.org/10.1364/OE.18.000A79.

(15) Nobel Committee for Chemistry. *Scientific Background to the Nobel Prize in Chemistry 2023: Quantum Dots – Seeds Of Nanoscience*. Royal Swedish Academy of Sciences.

(16) Montanarella, F.; Kovalenko, M. V. Three Millennia of Nanocrystals. *ACS Nano* **2022**, *16* (4), 5085–5102. https://doi.org/10.1021/acsnano.1c11159.

(17) Protesescu, L.; Yakunin, S.; Bodnarchuk, M. I.; Krieg, F.; Caputo, R.; Hendon, C. H.; Yang, R. X.; Walsh, A.; Kovalenko, M. V. Nanocrystals of Cesium Lead Halide Perovskites ($CsPbX_3$, X = Cl, Br, and I): Novel Optoelectronic Materials Showing Bright Emission with Wide Color Gamut. *Nano Lett* **2015**, *15* (6), 3692–3696. https://doi.org/10.1021/nl5048779.

(18) Sheehan, T. J.; Saris, S.; Tisdale, W. A. Exciton Transport in Perovskite Materials. *Advanced Materials* **2024**, *n/a* (n/a), 2415757. https://doi.org/https://doi.org/10.1002/adma.202415757.

(19) Bekenstein, Y.; Koscher, B. A.; Eaton, S. W.; Yang, P.; Alivisatos, A. P. Highly Luminescent Colloidal Nanoplates of Perovskite Cesium Lead Halide and Their Oriented Assemblies. *J Am Chem Soc* **2015**, *137* (51), 16008–16011. https://doi.org/10.1021/jacs.5b11199.

(20) Zhang, D.; Yang, Y.; Bekenstein, Y.; Yu, Y.; Gibson, N. A.; Wong, A. B.; Eaton, S. W.; Kornienko, N.; Kong, Q.; Lai, M.; Alivisatos, A. P.; Leone, S. R.; Yang, P. Synthesis of Composition Tunable and Highly Luminescent Cesium Lead Halide Nanowires through Anion-Exchange Reactions. *J Am Chem Soc* **2016**, *138* (23), 7236–7239. https://doi.org/10.1021/jacs.6b03134.

(21) Smith, M. D.; Crace, E. J.; Jaffe, A.; Karunadasa, H. I. The Diversity of Layered Halide Perovskites. *Annu Rev Mater Res* **2018**, *48*, 111–136. https://doi.org/10.1146/annurev-matsci-070317-124406.

(22) Jurow, M. J.; Morgenstern, T.; Eisler, C.; Kang, J.; Penzo, E.; Do, M.; Engelmayer, M.; Osowiecki, W. T.; Bekenstein, Y.; Tassone, C.; Wang, L. W.; Alivisatos, A. P.; Brütting, W.; Liu, Y. Manipulating the Transition Dipole Moment of $CsPbBr_3$ Perovskite Nanocrystals for Superior Optical Properties. *Nano Lett* **2019**, *19* (4), 2489–2496. https://doi.org/10.1021/acs.nanolett.9b00122.

(23) Zhou, N.; Bekenstein, Y.; Eisler, C. N.; Zhang, D.; Schwartzberg, A. M.; Yang, P.; Paul Alivisatos, A.; Lewis, J. A. Perovskite Nanowire–Block Copolymer Composites with Digitally Programmable Polarization Anisotropy. *Sci Adv* **2019**, *5* (5). https://doi.org/10.1126/sciadv.aav8141.

(24) Zhou, D.; Liu, D.; Pan, G.; Chen, X.; Li, D.; Xu, W.; Bai, X.; Song, H. Cerium and Ytterbium Codoped Halide Perovskite Quantum Dots: A Novel and Efficient Downconverter for Improving the Performance of Silicon Solar Cells. *Advanced Materials* **2017**, *29* (42). https://doi.org/10.1002/ADMA.201704149.

(25) Akkerman, Q. A.; Gandini, M.; Di Stasio, F.; Rastogi, P.; Palazon, F.; Bertoni, G.; Ball, J. M.; Prato, M.; Petrozza, A.; Manna, L. Strongly Emissive Perovskite Nanocrystal Inks for High-Voltage Solar Cells. *Nature Energy 2016 2:2* **2016**, *2* (2), 1–7. https://doi.org/10.1038/nenergy.2016.194.

(26) Yakunin, S.; Protesescu, L.; Krieg, F.; Bodnarchuk, M. I.; Nedelcu, G.; Humer, M.; De Luca, G.; Fiebig, M.; Heiss, W.; Kovalenko, M. V. Low-Threshold Amplified Spontaneous Emission and Lasing from Colloidal Nanocrystals of Caesium Lead Halide Perovskites. *Nat Commun* **2015**, *6*. https://doi.org/10.1038/ncomms9056.

(27) Ramasamy, P.; Lim, D. H.; Kim, B.; Lee, S. H.; Lee, M. S.; Lee, J. S. All-Inorganic Cesium Lead Halide Perovskite Nanocrystals for Photodetector Applications. *Chemical Communications* **2016**, *52* (10), 2067–2070. https://doi.org/10.1039/c5cc08643d.

(28) Zhang, J.; Wang, Q.; Zhang, X.; Jiang, J.; Gao, Z.; Jin, Z.; Liu, S. High-Performance Transparent Ultraviolet Photodetectors Based on Inorganic Perovskite $CsPbCl_3$ Nanocrystals. *RSC Adv* **2017**, *7* (58), 36722–36727. https://doi.org/10.1039/c7ra06597c.

(29) Chen, Q.; Wu, J.; Ou, X.; Huang, B.; Almutlaq, J.; Zhumekenov, A. A.; Guan, X.; Han, S.; Liang, L.; Yi, Z.; Li, J.; Xie, X.; Wang, Y.; Li, Y.; Fan, D.; Teh, D. B. L.; All, A. H.; Mohammed, O. F.; Bakr, O. M.; Wu, T.; Bettinelli, M.; Yang, H.; Huang, W.; Liu, X. All-Inorganic Perovskite Nanocrystal Scintillators. *Nature* **2018**, *561* (7721), 88–93. https://doi.org/10.1038/s41586-018-0451-1.

(30) Cao, Z.; Hu, F.; Zhang, C.; Zhu, S.; Xiao, M.; Wang, X. Optical Studies of Semiconductor Perovskite Nanocrystals for Classical Optoelectronic Applications and Quantum Information Technologies: A Review. *Advanced Photonics* **2020**, *2* (5), 054001. https://doi.org/10.1117/1.AP.2.5.054001.

(31) Zhu, J.; Li, Y.; Lin, X.; Han, Y.; Wu, K. Coherent Phenomena and Dynamics of Lead Halide Perovskite Nanocrystals for Quantum Information Technologies. *Nat Mater* **2024**, *23* (8), 1027–1040. https://doi.org/10.1038/s41563-024-01922-z.

(32) Dey, A.; Ye, J.; De, A.; Debroye, E.; Ha, S. K.; Bladt, E.; Kshirsagar, A. S.; Wang, Z.; Yin, J.; Wang, Y.; Quan, L. N.; Yan, F.; Gao, M.; Li, X.; Shamsi, J.; Debnath, T.; Cao, M.; Scheel, M. A.; Kumar, S.; Steele, J. A.; Gerhard, M.; Chouhan, L.; Xu, K.; Wu, X.; Li, Y.; Zhang, Y.; Dutta, A.; Han, C.; Vincon, I.; Rogach, A. L.; Nag, A.; Samanta, A.; Korgel, B. A.; Shih, C.-J.; Gamelin, D.

R.; Son, D. H.; Zeng, H.; Zhong, H.; Sun, H.; Demir, H. V.; Scheblykin, I. G.; Mora-Seró, I.; Stolarczyk, J. K.; Zhang, J. Z.; Feldmann, J.; Hofkens, J.; Luther, J. M.; Pérez-Prieto, J.; Li, L.; Manna, L.; Bodnarchuk, M. I.; Kovalenko, M. V; Roeffaers, M. B. J.; Pradhan, N.; Mohammed, O. F.; Bakr, O. M.; Yang, P.; Müller-Buschbaum, P.; Kamat, P. V; Bao, Q.; Zhang, Q.; Krahne, R.; Galian, R. E.; Stranks, S. D.; Bals, S.; Biju, V.; Tisdale, W. A.; Yan, Y.; Hoye, R. L. Z.; Polavarapu, L. State of the Art and Prospects for Halide Perovskite Nanocrystals. *ACS Nano* **2021**, *15* (7), 10775–10981. https://doi.org/10.1021/acsnano.0c08903.

(33) *Web of Science™*. Clarivate™ .

(34) Koscher, B. A.; Swabeck, J. K.; Bronstein, N. D.; Alivisatos, A. P. Essentially Trap-Free $_{CsPb}Br_3$ Colloidal Nanocrystals by Postsynthetic Thiocyanate Surface Treatment. *J Am Chem Soc* **2017**, *139* (19), 6566–6569. https://doi.org/10.1021/jacs.7b02817.

(35) Mondal, N.; De, A.; Samanta, A. Achieving Near-Unity Photoluminescence Efficiency for Blue-Violet-Emitting Perovskite Nanocrystals. *ACS Energy Lett* **2019**, *4* (1), 32–39. https://doi.org/10.1021/acsenergylett.8b01909.

(36) Di Stasio, F.; Christodoulou, S.; Huo, N.; Konstantatos, G. Near-Unity Photoluminescence Quantum Yield in $CsPbBr_3$ Nanocrystal Solid-State Films via Postsynthesis Treatment with Lead Bromide. *Chemistry of Materials* **2017**, *29* (18), 7663–7667. https://doi.org/10.1021/acs.chemmater.7b02834.

(37) Liu, F.; Zhang, Y.; Ding, C.; Kobayashi, S.; Izuishi, T.; Nakazawa, N.; Toyoda, T.; Ohta, T.; Hayase, S.; Minemoto, T.; Yoshino, K.; Dai, S.; Shen, Q. Highly Luminescent Phase-Stable $CsPbI_3$ Perovskite Quantum Dots Achieving Near 100% Absolute Photoluminescence Quantum Yield. *ACS Nano* **2017**, *11* (10), 10373–10383. https://doi.org/10.1021/acsnano.7b05442.

(38) Park, Y. S.; Guo, S.; Makarov, N. S.; Klimov, V. I. Room Temperature Single-Photon Emission from Individual Perovskite Quantum Dots. *ACS Nano* **2015**, *9* (10), 10386–10393. https://doi.org/10.1021/acsnano.5b04584.

(39) Hu, F.; Yin, C.; Zhang, H.; Sun, C.; Yu, W. W.; Zhang, C.; Wang, X.; Zhang, Y.; Xiao, M. Slow Auger Recombination of Charged Excitons in Nonblinking Perovskite Nanocrystals without Spectral Diffusion. *Nano Lett* **2016**, *16* (10), 6425–6430. https://doi.org/10.1021/acs.nanolett.6b02874.

(40) Rainò, G.; Nedelcu, G.; Protesescu, L.; Bodnarchuk, M. I.; Kovalenko, M. V.; Mahrt, R. F.; Stöferle, T. Single Cesium Lead Halide Perovskite Nanocrystals at Low Temperature: Fast Single-Photon Emission, Reduced Blinking, and Exciton Fine Structure. *ACS Nano* **2016**, *10* (2), 2485–2490. https://doi.org/10.1021/acsnano.5b07328.

(41) Rainò, G.; Yazdani, N.; Boehme, S. C.; Kober-Czerny, M.; Zhu, C.; Krieg, F.; Rossell, M. D.; Erni, R.; Wood, V.; Infante, I.; Kovalenko, M. V. Ultra-Narrow Room-Temperature Emission from Single $CsPbBr_3$ Perovskite Quantum Dots. *Nat Commun* **2022**, *13* (1), 1–8. https://doi.org/10.1038/s41467-022-30016-0.

(42) Zhu, C.; Marczak, M.; Feld, L.; Boehme, S. C.; Bernasconi, C.; Moskalenko, A.; Cherniukh, I.; Dirin, D.; Bodnarchuk, M. I.; Kovalenko, M. V.; Raino, G. Room-Temperature, Highly Pure Single-Photon Sources from All-Inorganic Lead Halide Perovskite Quantum Dots. *Nano Lett* **2022**, *22* (9), 3751–3760. https://doi.org/10.1021/acs.nanolett.2c00756.

(43) Hu, F.; Zhang, H.; Sun, C.; Yin, C.; Lv, B.; Zhang, C.; Yu, W. W.; Wang, X.; Zhang, Y.; Xiao, M. Superior Optical Properties of Perovskite Nanocrystals as Single Photon Emitters. *ACS Nano* **2015**, *9* (12), 12410–12416. https://doi.org/10.1021/acsnano.5b05769.

(44) Park, Y. S.; Guo, S.; Makarov, N. S.; Klimov, V. I. Room Temperature Single-Photon Emission from Individual Perovskite Quantum Dots. *ACS Nano* **2015**, *9* (10), 10386–10393. https://doi.org/10.1021/acsnano.5b04584.

(45) Utzat, H.; Sun, W.; Kaplan, A. E. K.; Krieg, F.; Ginterseder, M.; Spokoyny, B.; Klein, N. D.; Shulenberger, K. E.; Perkinson, C. F.; Kovalenko, M. V.; Bawendi, M. G. Coherent Single-Photon Emission from Colloidal Lead Halide Perovskite Quantum Dots. *Science* **2019**, *363* (6431). https://doi.org/10.1126/science.aau7392.

(46) Posmyk, K.; Zawadzka, N.; Kipczak, Ł.; Dyksik, M.; Surrente, A.; Maude, D. K.; Kazimierczuk, T.; Babiński, A.; Molas, M. R.; Bumrungsan, W.; Chooseng, C.; Paritmongkol, W.; Tisdale, W. A.; Baranowski, M.; Plochocka, P. Bright Excitonic Fine Structure in Metal-Halide Perovskites: From Two-Dimensional to Bulk. *J Am Chem Soc* **2024**, *146* (7), 4687–4694. https://doi.org/10.1021/jacs.3c11957.

(47) Sercel, P. C.; Lyons, J. L.; Wickramaratne, D.; Vaxenburg, R.; Bernstein, N.; Efros, A. L. Exciton Fine Structure in Perovskite Nanocrystals. *Nano Lett* **2019**, *19* (6), 4068–4077. https://doi.org/10.1021/acs.nanolett.9b01467.

(48) Gramlich, M.; Swift, M. W.; Lampe, C.; Lyons, J. L.; Döblinger, M.; Efros, A. L.; Sercel, P. C.; Urban, A. S. Dark and Bright Excitons in Halide Perovskite Nanoplatelets. *Advanced Science* **2022**, *9* (5), 2103013. https://doi.org/10.1002/advs.202103013.

(49) Biliroglu, M.; Findik, G.; Mendes, J.; Seyitliyev, D.; Lei, L.; Dong, Q.; Mehta, Y.; Temnov, V. V.; So, F.; Gundogdu, K. Room-Temperature Superfluorescence in Hybrid Perovskites and Its Origins. *Nat Photonics* **2022**, *16* (4), 324–329. https://doi.org/10.1038/s41566-022-00974-4.

(50) Zhu, C.; Boehme, S. C.; Feld, L. G.; Moskalenko, A.; Dirin, D. N.; Mahrt, R. F.; Stöferle, T.; Bodnarchuk, M. I.; Efros, A. L.; Sercel, P. C.; Kovalenko, M. V.; Rainò, G. Single-Photon Superradiance in Individual Caesium Lead Halide Quantum Dots. *Nature* **2024**, *626* (7999), 535–541. https://doi.org/10.1038/s41586-023-07001-8.

(51) Sekh, T. V.; Cherniukh, I.; Kobiyama, E.; Sheehan, T. J.; Manoli, A.; Zhu, C.; Athanasiou, M.; Sergides, M.; Ortikova, O.; Rossell, M. D.; Bertolotti, F.; Guagliardi, A.; Masciocchi, N.; Erni, R.; Othonos, A.; Itskos, G.; Tisdale, W. A.; Stöferle, T.; Rainò, G.; Bodnarchuk, M. I.; Kovalenko, M. V. All-Perovskite Multicomponent Nanocrystal Superlattices. *ACS Nano* **2024**, *18* (11), 8423–8436. https://doi.org/10.1021/acsnano.3c13062.

(52) Rainò, G.; Becker, M. A.; Bodnarchuk, M. I.; Mahrt, R. F.; Kovalenko, M. V.; Stöferle, T. Superfluorescence from Lead Halide Perovskite Quantum Dot Superlattices. *Nature* **2018**, *563* (7733), 671–675. https://doi.org/10.1038/s41586-018-0683-0.

(53) Jurow, M. J.; Lampe, T.; Penzo, E.; Kang, J.; Koc, M. A.; Zechel, T.; Nett, Z.; Brady, M.; Wang, L. W.; Alivisatos, A. P.; Cabrini, S.; Brütting, W.; Liu, Y. Tunable Anisotropic Photon Emission from Self-Organized $CsPbBr_3$ Perovskite Nanocrystals. *Nano Lett* **2017**, *17* (7), 4534–4540. https://doi.org/10.1021/acs.nanolett.7b02147.

(54) Miranti, R.; Komatsu, R.; Enomoto, K.; Inoue, D.; Pu, Y. J. Symmetry-Broken Electronic State of $CsPbBr_3$ Cubic Perovskite Nanocrystals. *J Phys Chem Lett* **2024**, *15* (39), 10009–10017. https://doi.org/10.1021/acs.jpclett.4c02160.

(55) Bertolotti, F.; Nedelcu, G.; Vivani, A.; Cervellino, A.; Masciocchi, N.; Guagliardi, A.; Kovalenko, M. V. Crystal Structure, Morphology, and Surface Termination of Cyan-Emissive, Six-Monolayers-Thick $CsPbBr_3$ Nanoplatelets from X-Ray Total Scattering. *ACS Nano* **2019**, *13* (12), 14294–14307. https://doi.org/10.1021/acsnano.9b07626.

(56) Brivio, F.; Frost, J. M.; Skelton, J. M.; Jackson, A. J.; Weber, O. J.; Weller, M. T.; Goñi, A. R.; Leguy, A. M. A.; Barnes, P. R. F.; Walsh, A. Lattice Dynamics and Vibrational Spectra of the Orthorhombic, Tetragonal, and Cubic Phases of Methylammonium Lead Iodide. *Phys Rev B* **2015**, *92* (14), 144308. https://doi.org/10.1103/PhysRevB.92.144308.

(57) De Roo, J.; Ibáñez, M.; Geiregat, P.; Nedelcu, G.; Walravens, W.; Maes, J.; Martins, J. C.; Van Driessche, I.; Kovalenko, M. V; Hens, Z. Highly Dynamic Ligand Binding and Light Absorption Coefficient of Cesium Lead Bromide Perovskite Nanocrystals. *ACS Nano* **2016**, *10* (2), 2071–2081. https://doi.org/10.1021/acsnano.5b06295.

(58) Wang, S.; Yousefi Amin, A. A.; Wu, L.; Cao, M.; Zhang, Q.; Ameri, T. Perovskite Nanocrystals: Synthesis, Stability, and Optoelectronic Applications. *Small Struct* **2021**, *2* (3), 2000124. https://doi.org/10.1002/sstr.202000124.

(59) Lorenzon, M.; Jurow, M.; Hong, M. J.; Lu, Y. H.; Barnard, E. S.; Salmeron, M.; Liu, Y.; Penzo, E.; Schwartzberg, A. M.; Weber-Bargioni, A. Improved Stability and Exciton Diffusion of Self-Assembled 2D Lattices of Inorganic Perovskite Nanocrystals by Atomic Layer Deposition. *Adv Opt Mater* **2020**, *8* (20). https://doi.org/10.1002/adom.202000900.

(60) Zhang, F.; Shi, Z. F.; Ma, Z. Z.; Li, Y.; Li, S.; Wu, D.; Xu, T. T.; Li, X. J.; Shan, C. X.; Du, G. T. Silica Coating Enhances the Stability of Inorganic Perovskite Nanocrystals for Efficient and Stable Down-Conversion in White Light-Emitting Devices. *Nanoscale* **2018**, *10* (43), 20131–20139. https://doi.org/10.1039/c8nr07022a.

(61) Sun, Y.; Li, Y.; Zhang, W.; Zhu, P.; Zhu, H.; Qin, W.; Wang, G. Simultaneous Synthesis, Modification, and DFT Calculation of Three-Color Lead Halide Perovskite Phosphors for Improving Stability and Luminous Efficiency of WLEDs. *Adv Opt Mater* **2022**, *10* (2), 2101765. https://doi.org/10.1002/adom.202101765.

(62) Dirin, D. N.; Protesescu, L.; Trummer, D.; Kochetygov, I. V.; Yakunin, S.; Krumeich, F.; Stadie, N. P.; Kovalenko, M. V. Harnessing Defect-Tolerance at the Nanoscale: Highly Luminescent Lead Halide Perovskite Nanocrystals in Mesoporous Silica Matrixes. *Nano Lett* **2016**, *16* (9), 5866–5874. https://doi.org/10.1021/acs.nanolett.6b02688.

(63) Moody, G.; Sorger, V. J.; Blumenthal, D. J.; Juodawlkis, P. W.; Loh, W.; Sorace-Agaskar, C.; Jones, A. E.; Balram, K. C.; Matthews, J. C. F.; Laing, A.; Davanco, M.; Chang, L.; Bowers, J. E.; Quack, N.; Galland, C.; Aharonovich, I.; Wolff, M. A.; Schuck, C.; Sinclair, N.; Lončar, M.; Komljenovic, T.; Weld, D.; Mookherjea, S.; Buckley, S.; Radulaski, M.; Reitzenstein, S.; Pingault, B.; Machielse, B.; Mukhopadhyay, D.; Akimov, A.; Zheltikov, A.; Agarwal, G. S.; Srinivasan, K.; Lu, J.; Tang, H. X.; Jiang, W.; McKenna, T. P.; Safavi-Naeini, A. H.; Steinhauer, S.; Elshaari, A. W.; Zwiller, V.; Davids, P. S.; Martinez, N.; Gehl, M.; Chiaverini, J.; Mehta, K. K.; Romero, J.; Lingaraju, N. B.; Weiner, A. M.; Peace, D.; Cernansky, R.; Lobino, M.; Diamanti, E.; Vidarte, L. T.; Camacho, R. M. 2022 Roadmap on Integrated Quantum Photonics. *Journal of Physics: Photonics* **2022**, *4* (1), 012501. https://doi.org/10.1088/2515-7647/ac1ef4.

(64) Hofmann, A.; Schmid, M.; Brütting, W. The Many Facets of Molecular Orientation in Organic Optoelectronics. *Adv Opt Mater* **2021**, *9* (21), 2101004. https://doi.org/10.1002/ADOM.202101004.

(65) Colvin, V. L.; Alivisatos, A. P. CdSe Nanocrystals with a Dipole Moment in the First Excited State. *J Chem Phys* **1992**, *97* (1), 730–733. https://doi.org/10.1063/1.463573.

(66) Gao, Y.; Weidman, M. C.; Tisdale, W. A. CdSe Nanoplatelet Films with Controlled Orientation of Their Transition Dipole Moment. *Nano Lett* **2017**, *17* (6), 3837–3843. https://doi.org/10.1021/acs.nanolett.7b01237.

(67) Schuller, J. A.; Karaveli, S.; Schiros, T.; He, K.; Yang, S.; Kymissis, I.; Shan, J.; Zia, R. Orientation of Luminescent Excitons in Layered Nanomaterials. *Nat Nanotechnol* **2013**, *8* (4), 271–276. https://doi.org/10.1038/nnano.2013.20.

(68) Kurvits, J. A.; Jiang, M.; Zia, R. Comparative Analysis of Imaging Configurations and Objectives for Fourier Microscopy. *Journal of the Optical Society of America A* **2015**, *32* (11), 2082. https://doi.org/10.1364/JOSAA.32.002082.

(69) Kim, K.-H.; Kim, J.-J.; Kim, K.-H.; Kim, J.-J. Origin and Control of Orientation of Phosphorescent and TADF Dyes for High-Efficiency OLEDs. *Advanced Materials* **2018**, *30* (42), 1705600. https://doi.org/10.1002/ADMA.201705600.

(70) Lieb, M. A.; Zavislan, J. M.; Novotny, L. Single-Molecule Orientations Determined by Direct Emission Pattern Imaging. *Journal of the Optical Society of America B* **2004**, *21* (6), 1210. https://doi.org/10.1364/JOSAB.21.001210.

(71) Taminiau, T. H.; Karaveli, S.; Hulst, N. F. Van; Zia, R. Quantifying the Magnetic Nature of Light Emission. *Nat Commun* **2012**, *3*, 976–979. https://doi.org/10.1038/ncomms1984.

(72) Russ, B.; Lin, T.-T.; Elenteny, H.; Eisler, C. N. Quantifying the Accuracy and Precision of the Transition Dipole Moment Alignment from Realistic Angular Emission Data. *ACS Photonics* **2025**. https://doi.org/10.1021/acsphotonics.5c00684.

(73) Eisler, C. N.; Parsons, L. E.; Nett, Z.; Love, C.; Schwartzberg, A. M.; Alivisatos, A. P. Photonic Luminescent Solar Concentrator Design for High Efficiency, Low Cost Multijunction Photovoltaics. *Frontiers in Photonics* **2022**, *3*. https://doi.org/10.3389/fphot.2022.932913.

(74) Shockley, W.; Queisser, H. J. Detailed Balance Limit of Efficiency of P-n Junction Solar Cells. *J Appl Phys* **1961**, *32* (3), 510–519. https://doi.org/10.1063/1.1736034.

(75) Marti, A.; Arafijo, G. L. *Limiting Efficiencies for Photovoltaic Energy Conversion in Multigap Systems*; 1996; Vol. 43.

(76) Horowitz, K. A.; Remo, T. W.; Smith, B.; Ptak, A. J. *A Techno-Economic Analysis and Cost Reduction Roadmap for III-V Solar Cells*; United States, 2018. https://doi.org/10.2172/1484349.

(77) Bobela, D. C.; Gedvilas, L.; Woodhouse, M.; Horowitz, K. A. W.; Basore, P. A. Economic Competitiveness of III–V on Silicon Tandem One-Sun Photovoltaic Solar Modules in Favorable Future Scenarios. *Progress in Photovoltaics: Research and Applications* **2017**, *25* (1), 41–48. https://doi.org/10.1002/pip.2808.

(78) Nicolás, R. O.; Durán, J. C. Theoretical Maximum Concentration Factors for Solar Concentrators. *Journal of the Optical Society of America A* **1984**, *1* (11), 1110–1113. https://doi.org/10.1364/JOSAA.1.001110.

(79) Alzahrani, M. M.; Shanks, K.; Chanchangi, Y.; Cameron, W. J.; Maatallah, T. S.; Mallick, T. K. Record High Solar Concentration Ratio for Photovoltaics: Experimental Validation for Achieving Effective Concentration of >1200 Suns. *Solar Energy* **2024**, *271*, 112427. https://doi.org/10.1016/j.solener.2024.112427.

(80) Kinsey, G. S.; Nayak, A.; Liu, M.; Garboushian, V. Increasing Power and Energy in Amonix CPV Solar Power Plants. *IEEE J Photovolt* **2011**, *1* (2), 213–218. https://doi.org/10.1109/JPHOTOV.2011.2172775.

(81) Yablonovitch, E. Thermodynamics of the Fluorescent Planar Concentrator. *J Opt Soc Am* **1980**, *70* (11), 1362. https://doi.org/10.1364/JOSA.70.001362.

(82) Bronstein, N. D. Material and Optical Design Rules for High Performance Luminescent Solar Concentrators, 2015.

(83) de Clercq, D. M.; Chan, S. v.; Hardy, J.; Price, M. B.; Davis, N. J. L. K. Reducing Reabsorption in Luminescent Solar Concentrators with a Self-Assembling Polymer Matrix. *J Lumin* **2021**, *236*. https://doi.org/10.1016/j.jlumin.2021.118095.

(84) Albers, P. T. M.; Bastiaansen, C. W. M.; Debije, M. G. Dual Waveguide Patterned Luminescent Solar Concentrators. *Solar Energy* **2013**, *95*, 216–223. https://doi.org/10.1016/j.solener.2013.06.014.

(85) Li, S.; Liu, H.; Chen, W.; Zhou, Z.; Wu, D.; Lu, R.; Zhao, B.; Hao, J.; Yang, L.; Yang, H.; Cai, R.; Xu, B.; Wang, K.; Sun, X. W. Low Reabsorption and Stability Enhanced Luminescent Solar Concentrators Based on Silica Encapsulated Quantum Rods. *Solar Energy Materials and Solar Cells* **2020**, *206*. https://doi.org/10.1016/j.solmat.2019.110321.

(86) Bronstein, N. D.; Li, L.; Xu, L.; Yao, Y.; Ferry, V. E.; Alivisatos, A. P.; Nuzzo, R. G. Luminescent Solar Concentration with Semiconductor Nanorods and Transfer-Printed Micro-Silicon Solar Cells. *ACS Nano* **2014**, *8* (1), 44–53. https://doi.org/10.1021/nn404418h.

(87) Kutayiah, A. R.; Kumar, S.; Ratnaweera, R.; Easwaran, K.; Sheldon, M. Markov Chains for Modeling Complex Luminescence, Absorption, and Scattering in Nanophotonic Systems. *Opt Express* **2021**, *29* (3), 4249–4269. https://doi.org/10.1364/OE.416670.

(88) Gutmann, J.; Zappe, H.; Goldschmidt, J. C. Predicting the Performance of Photonic Luminescent Solar Concentrators. In *Conference Record of the IEEE Photovoltaic Specialists Conference*; Institute of Electrical and Electronics Engineers Inc., 2013; pp 1864–1868. https://doi.org/10.1109/PVSC.2013.6744506.

(89) Momper, R.; Zhang, H.; Chen, S.; Halim, H.; Johannes, E.; Yordanov, S.; Braga, D.; Blülle, B.; Doblas, D.; Kraus, T.; Kraus, T.; Bonn, M.; Wang, H. I.; Riedinger, A. Kinetic Control over Self-Assembly of Semiconductor Nanoplatelets. *Nano Lett* **2020**, *20* (6), 4102–4110. https://doi.org/10.1021/acs.nanolett.9b05270.

(90) Emmott, C. J. M.; Röhr, J. A.; Campoy-Quiles, M.; Kirchartz, T.; Urbina, A.; Ekins-Daukes, N. J.; Nelson, J. Organic Photovoltaic Greenhouses: A Unique Application for Semi-Transparent PV? *Energy Environ Sci* **2015**, *8* (4), 1317–1328. https://doi.org/10.1039/C4EE03132F.

(91) Shi, H.; Xia, R.; Zhang, G.; Yip, H.-L.; Cao, Y. Spectral Engineering of Semitransparent Polymer Solar Cells for Greenhouse Applications. *Adv Energy Mater* **2019**, *9* (5), 1803438. https://doi.org/10.1002/aenm.201803438.

(92) Allardyce, C. S.; Fankhauser, C.; Zakeeruddin, S. M.; Grätzel, M.; Dyson, P. J. The Influence of Greenhouse-Integrated Photovoltaics on Crop Production. *Solar Energy* **2017**, *155*, 517–522. https://doi.org/10.1016/j.solener.2017.06.044.

(93) Jagadamma, L. K.; Wang, S. Wide-Bandgap Halide Perovskites for Indoor Photovoltaics. *Front Chem* **2021**, *Volume 9-2021*.

(94) Shukla, A. K.; Sudhakar, K.; Baredar, P. A Comprehensive Review on Design of Building Integrated Photovoltaic System. *Energy Build* **2016**, *128*, 99–110. https://doi.org/10.1016/j.enbuild.2016.06.077.

(95) Li, J.; Aierken, A.; Liu, Y.; Zhuang, Y.; Yang, X.; Mo, J. H.; Fan, R. K.; Chen, Q. Y.; Zhang, S. Y.; Huang, Y. M.; Zhang, Q. A Brief Review of High Efficiency III-V Solar Cells for Space Application. *Front Phys* **2021**, *Volume 8-2020*.

(96) Meddeb, H.; Götz-Köhler, M.; Neugebohrn, N.; Banik, U.; Osterthun, N.; Sergeev, O.; Berends, D.; Lattyak, C.; Gehrke, K.; Vehse, M. Tunable Photovoltaics: Adapting Solar Cell Technologies to Versatile Applications. *Adv Energy Mater* **2022**, *12* (28), 2200713. https://doi.org/10.1002/aenm.202200713.

(97) Schygulla, P.; Müller, R.; Höhn, O.; Schachtner, M.; Chojniak, D.; Cordaro, A.; Tabernig, S.; Bläsi, B.; Polman, A.; Siefer, G.; Lackner, D.; Dimroth, F. Wafer-Bonded Two-Terminal III-V//Si Triple-Junction Solar Cell with Power Conversion Efficiency of 36.1% at AM1.5g. *Progress in Photovoltaics: Research and Applications* **2025**, *33* (1), 100–108. https://doi.org/10.1002/pip.3769.

(98) Essig, S.; Allebé, C.; Remo, T.; Geisz, J. F.; Steiner, M. A.; Horowitz, K.; Barraud, L.; Ward, J. S.; Schnabel, M.; Descoeudres, A.; Young, D. L.; Woodhouse, M.; Despeisse, M.; Ballif, C.; Tamboli, A. Raising the One-Sun Conversion Efficiency of III–V/Si Solar Cells to 32.8% for Two Junctions and 35.9% for Three Junctions. *Nat Energy* **2017**, *2* (9), 17144. https://doi.org/10.1038/nenergy.2017.144.

(99) Feifel, M.; Lackner, D.; Schön, J.; Ohlmann, J.; Benick, J.; Siefer, G.; Predan, F.; Hermle, M.; Dimroth, F. Epitaxial GaInP/GaAs/Si Triple-Junction Solar Cell with 25.9% AM1.5g Efficiency Enabled by Transparent Metamorphic AlxGa1−xAsyP1−y Step-Graded Buffer Structures. *Solar RRL* **2021**, *5* (5), 2000763. https://doi.org/10.1002/solr.202000763.

(100) Bauser, H. C.; Bukowsky, C. R.; Phelan, M.; Weigand, W.; Needell, D. R.; Holman, Z. C.; Atwater, H. A. Photonic Crystal Waveguides for >90% Light Trapping Efficiency in Luminescent Solar Concentrators. *ACS Photonics* **2020**, *7* (8), 2122–2131. https://doi.org/10.1021/acsphotonics.0c00593.

(101) Peters, M.; Goldschmidt, J. C.; Löper, P.; Bläsi, B.; Gombert, A. The Effect of Photonic Structures on the Light Guiding Efficiency of Fluorescent Concentrators. *J Appl Phys* **2009**, *105* (1). https://doi.org/10.1063/1.2996081.

(102) Green, M. A.; Dunlop, E. D.; Hohl-Ebinger, J.; Yoshita, M.; Kopidakis, N.; Hao, X. Solar Cell Efficiency Tables (Version 58). *Progress in Photovoltaics: Research and Applications* **2021**, *29* (7), 657–667. https://doi.org/10.1002/pip.3444.

(103) Larouche, S.; Martinu, L. *OpenFilters: Open-Source Software for the Design, Optimization, and Synthesis of Optical Filters*; 2008. http://www.polymtl.ca/larfis.

(104) Olson, R. W.; Loring, R. F.; Fayer, M. D. *Luminescent Solar Concentrators and the Reabsorption Problem*; 1981.

(105) Warmann, E. C. Design Strategies for Ultra-High Efficiency Photovoltaics, California Institute of Technology, Pasadena, CA, 2014.

(106) Warmann, E. C.; Flowers, C.; Lloyd, J.; Eisler, C. N.; Escarra, M. D.; Atwater, H. A. Design of Photovoltaics for Modules with 50% Efficiency. *Energy Sci Eng* **2017**, *5* (2), 69–80. https://doi.org/10.1002/ese3.155.

(107) Lewis, N. S. Research Opportunities to Advance Solar Energy Utilization. *Science* **2016**, *351* (6271), aad1920. https://doi.org/10.1126/science.aad1920.

(108) Wu, K.; Li, H.; Klimov, V. I. Tandem Luminescent Solar Concentrators Based on Engineered Quantum Dots. *Nat Photonics* **2018**, *12* (2), 105–110. https://doi.org/10.1038/s41566-017-0070-7.

(109) MacQueen, R. W.; Cheng, Y. Y.; Clady, R. G. C. R.; Schmidt, T. W. Towards an Aligned Luminophore Solar Concentrator. *Opt Express* **2010**, *18* (S2), A161–A166. https://doi.org/10.1364/OE.18.00A161.

(110) Tsoi, S.; Broer, D. J.; Bastiaansen, C. W. M.; Debije, M. G. Patterned Dye Structures Limit Reabsorption in Luminescent Solar Concentrators. *Opt Express* **2010**, *18* (S4), A536–A543. https://doi.org/10.1364/OE.18.00A536.

(111) Castelletto, S.; Boretti, A. Luminescence Solar Concentrators: A Technology Update. *Nano Energy* **2023**, *109*, 108269. https://doi.org/10.1016/j.nanoen.2023.108269.

(112) Parsons, L.; Russ, B.; Eisler, C. Tunable Angular Light Emission of Lead Halide Perovskite Nanocrystal Thin Films via Solution-Processed Substrate Treatment. *ACS Nanoscience Au* **2025**. https://doi.org/10.1021/acsnanoscienceau.5c00054.

(113) Parsons, L.; Grishchenko, A.; Eisler, C. Oriented Dipoles in Ordered Ensembles of Confined Lead Halide Perovskite Nanocrystals. **2025**, *Submitted*.

(114) Chen, J.; Zhou, Y.; Fu, Y.; Pan, J.; Mohammed, O. F.; Bakr, O. M. Oriented Halide Perovskite Nanostructures and Thin Films for Optoelectronics. *Chem Rev* **2021**, *121* (20), 12112–12180. https://doi.org/10.1021/acs.chemrev.1c00181.

(115) Jurow, M. J.; Mayr, C.; Schmidt, T. D.; Lampe, T.; Djurovich, P. I.; Brütting, W.; Thompson, M. E. Understanding and Predicting the Orientation of Heteroleptic Phosphors in Organic Light-Emitting Materials. *Nat Mater* **2016**, *15* (1), 85–91. https://doi.org/10.1038/nmat4428.

(116) Brütting, W.; Frischeisen, J.; Schmidt, T. D.; Scholz, B. J.; Mayr, C. Device Efficiency of Organic Light-Emitting Diodes: Progress by Improved Light Outcoupling. *physica status solidi (a)* **2013**, *210* (1), 44–65. https://doi.org/10.1002/pssa.201228320.

(117) Cao, Y.; Wang, N.; Tian, H.; Guo, J.; Wei, Y.; Chen, H.; Miao, Y.; Zou, W.; Pan, K.; He, Y.; Cao, H.; Ke, Y.; Xu, M.; Wang, Y.; Yang, M.; Du, K.; Fu, Z.; Kong, D.; Dai, D.; Jin, Y.; Li, G.; Li, H.; Peng, Q.; Wang, J.; Huang, W. Perovskite Light-Emitting Diodes Based on Spontaneously Formed Submicrometre-Scale Structures. *Nature* **2018**, *562* (7726), 249–253. https://doi.org/10.1038/s41586-018-0576-2.

(118) Richter, J. M.; Abdi-Jalebi, M.; Sadhanala, A.; Tabachnyk, M.; Rivett, J. P. H.; Pazos-Outón, L. M.; Gödel, K. C.; Price, M.; Deschler, F.; Friend, R. H. Enhancing Photoluminescence Yields in Lead Halide Perovskites by Photon Recycling and Light Out-Coupling. *Nat Commun* **2016**, *7* (1), 13941. https://doi.org/10.1038/ncomms13941.

(119) Zhao, Y.; Yin, X.; Li, P.; Ren, Z.; Gu, Z.; Zhang, Y.; Song, Y. Multifunctional Perovskite Photodetectors: From Molecular-Scale Crystal Structure Design to Micro/Nano-Scale Morphology Manipulation. *Nanomicro Lett* **2023**, *15* (1), 187. https://doi.org/10.1007/s40820-023-01161-y.

(120) Hao, J.; Kim, Y.-H.; Habisreutinger, S. N.; Harvey, S. P.; Miller, E. M.; Foradori, S. M.; Arnold, M. S.; Song, Z.; Yan, Y.; Luther, J. M.; Blackburn, J. L. Low-Energy Room-Temperature Optical Switching in Mixed-Dimensionality Nanoscale Perovskite Heterojunctions. *Sci Adv* **2025**, *7* (18), eabf1959. https://doi.org/10.1126/sciadv.abf1959.

(121) Wang, H.; Haroldson, R.; Balachandran, B.; Zakhidov, A.; Sohal, S.; Chan, J. Y.; Zakhidov, A.; Hu, W. Nanoimprinted Perovskite Nanograting Photodetector with Improved Efficiency. *ACS Nano* **2016**, *10* (12), 10921–10928. https://doi.org/10.1021/acsnano.6b05535.

(122) Marcato, T.; Shih, C.-J. Molecular Orientation Effects in Organic Light-Emitting Diodes. *Helv Chim Acta* **2019**, *102* (5), e1900048. https://doi.org/10.1002/hlca.201900048.

(123) Kim, J.; Zhao, H.; Hou, S.; Khatoniar, M.; Menon, V.; Forrest, S. R. Using Fourier-Plane Imaging Microscopy for Determining Transition-Dipole-Moment Orientations in Organic Light-Emitting Devices. *Phys Rev Appl* **2020**, *14* (3), 34048. https://doi.org/10.1103/PhysRevApplied.14.034048.

(124) Brown, A. A. M.; Mathews, N.; Vashishtha, P.; Hooper, T. J. N.; Ng, Y. F.; Nutan, G. V.; Fang, Y.; Giovanni, D.; Tey, J. N.; Jiang, L.; Damodaran, B.; Sum, T. C.; Pu, S. H.; Mhaisalkar, S. G. Precise Control of $CsPbBr_3$ Perovskite Nanocrystal Growth at Room Temperature: Size Tunability and Synthetic Insights. *Chemistry of Materials* **2021**, *33* (7), 2387–2397. https://doi.org/10.1021/acs.chemmater.0c04569.

(125) Pan, J.; Huang, H.; Zhao, W.; Lin, D.; Nie, Z.; Zhong, J.; Ma, L.; Zhang, X. Efficient and Stable Self-Assembly Blue-Emitting $CsPbBr_3$ Nanoplatelets with Self-Repaired Surface Defects. *ACS Appl Nano Mater* **2022**, *5* (10), 15062–15069. https://doi.org/10.1021/acsanm.2c03231.

(126) Morrell, M. V.; He, X.; Luo, G.; Thind, A. S.; White, T. A.; Hachtel, J. A.; Borisevich, A. Y.; Idrobo, J. C.; Mishra, R.; Xing, Y. Significantly Enhanced Emission Stability of $CsPbBr_3$ Nanocrystals via Chemically Induced Fusion Growth for Optoelectronic Devices. *ACS Appl Nano Mater* **2018**, *1* (11), 6091–6098. https://doi.org/10.1021/acsanm.8b01298.

(127) Le, T. H.; Lee, S.; Jo, H.; Jeong, G.; Chang, M.; Yoon, H. Morphology-Dependent Ambient-Condition Growth of Perovskite Nanocrystals for Enhanced Stability in Photoconversion Device. *Journal of Physical Chemistry Letters* **2021**, *12* (23), 5631–5638. https://doi.org/10.1021/acs.jpclett.1c01376.

(128) Singldinger, A.; Gramlich, M.; Gruber, C.; Lampe, C.; Urban, A. S. Nonradiative Energy Transfer between Thickness-Controlled Halide Perovskite Nanoplatelets. *ACS Energy Lett* **2020**, *5* (5), 1380–1385. https://doi.org/10.1021/acsenergylett.0c00471.

(129) Liu, S.; Akram, W.; Ye, F.; Jin, J.; Niu, F.; Ahmed, S.; Ouyang, Z.; Dong, S.-C.; Li, G. Förster Resonance Energy Transfer in Metal Halide Perovskite: Current Status and Future Prospects. *ChemistryOpen* **2025**, *14* (3), e202400118. https://doi.org/10.1002/open.202400118.

(130) Akriti; Lin, Z. Y.; Park, J. Y.; Yang, H.; Savoie, B. M.; Dou, L. Anion Diffusion in Two-Dimensional Halide Perovskites. *APL Mater* **2022**, *10* (4), 40903. https://doi.org/10.1063/5.0088538/2834945.

(131) Roiati, V.; Mosconi, E.; Listorti, A.; Colella, S.; Gigli, G.; De Angelis, F. Stark Effect in Perovskite/TiO_2 Solar Cells: Evidence of Local Interfacial Order. *Nano Lett* **2014**, *14* (4), 2168–2174. https://doi.org/10.1021/nl500544c.

(132) Liu, F.; Sidhik, S.; Hoffbauer, M. A.; Lewis, S.; Neukirch, A. J.; Pavlenko, V.; Tsai, H.; Nie, W.; Even, J.; Tretiak, S.; Ajayan, P. M.; Kanatzidis, M. G.; Crochet, J. J.; Moody, N. A.; Blancon, J.-C.; Mohite, A. D. Highly Efficient Photoelectric Effect in Halide Perovskites for Regenerative Electron Sources. *Nat Commun* **2021**, *12* (1), 673. https://doi.org/10.1038/s41467-021-20954-6.

(133) Kambhampati, P. Learning about the Structural Dynamics of Semiconductor Perovskites from Electron Solvation Dynamics. *The Journal of Physical Chemistry C* **2021**, *125* (43), 23571–23586. https://doi.org/10.1021/acs.jpcc.1c07445.

(134) Dapor, M. Role of the Tail of High-Energy Secondary Electrons in the Monte Carlo Evaluation of the Fraction of Electrons Backscattered from Polymethylmethacrylate. *Appl Surf Sci* **2017**, *391*, 3–11. https://doi.org/10.1016/j.apsusc.2015.12.043.

(135) Krajewska, C. J.; Kaplan, A. E. K.; Kick, M.; Berkinsky, D. B.; Zhu, H.; Sverko, T.; Van Voorhis, T.; Bawendi, M. G. Controlled Assembly and Anomalous Thermal Expansion of Ultrathin Cesium Lead Bromide Nanoplatelets. *Nano Lett* **2023**, *23* (6), 2148–2157. https://doi.org/10.1021/acs.nanolett.2c04526.

(136) Wei, M.; de Arquer, F. P. G.; Walters, G.; Yang, Z.; Quan, L. N.; Kim, Y.; Sabatini, R.; Quintero-Bermudez, R.; Gao, L.; Fan, J. Z.; Fan, F.; Gold-Parker, A.; Toney, M. F.; Sargent, E. H. Ultrafast Narrowband Exciton Routing within Layered Perovskite Nanoplatelets Enables Low-Loss Luminescent Solar Concentrators. *Nat Energy* **2019**, *4* (3), 197–205. https://doi.org/10.1038/s41560-018-0313-y.

(137) Russ, B.; Eisler, C. N. The Future of Quantum Technologies: Superfluorescence from Solution-Processed, Tunable Materials. *Nanophotonics* **2024**, 1–9. https://doi.org/10.1515/nanoph-2023-0919.

(138) Pietra, F.; Rabouw, F. T.; Evers, W. H.; Byelov, D. V; Petukhov, A. V; de Mello Donegá, C.; Vanmaekelbergh, D. Semiconductor Nanorod Self-Assembly at the Liquid/Air Interface Studied by in Situ GISAXS and Ex Situ TEM. *Nano Lett* **2012**, *12* (11), 5515–5523. https://doi.org/10.1021/nl302360u.

(139) Marino, E.; Jiang, Z.; Kodger, T. E.; Murray, C. B.; Schall, P. Controlled Assembly of CdSe Nanoplatelet Thin Films and Nanowires. *Langmuir* **2023**, *39* (36), 12533–12540. https://doi.org/10.1021/acs.langmuir.3c00933.

(140) Dong, A.; Chen, J.; Vora, P. M.; Kikkawa, J. M.; Murray, C. B. Binary Nanocrystal Superlattice Membranes Self-Assembled at the Liquid–Air Interface. *Nature* **2010**, *466* (7305), 474–477. https://doi.org/10.1038/nature09188.

(141) Diroll, B. T.; Greybush, N. J.; Kagan, C. R.; Murray, C. B. Smectic Nanorod Superlattices Assembled on Liquid Subphases: Structure, Orientation, Defects, and Optical Polarization. *Chemistry of Materials* **2015**, *27* (8), 2998–3008. https://doi.org/10.1021/acs.chemmater.5b00355.

(142) Boles, M. A.; Engel, M.; Talapin, D. V. Self-Assembly of Colloidal Nanocrystals: From Intricate Structures to Functional Materials. *Chem Rev* **2016**, *116* (18), 11220–11289. https://doi.org/10.1021/acs.chemrev.6b00196.

(143) Ye, X.; Zhu, C.; Ercius, P.; Raja, S. N.; He, B.; Jones, M. R.; Hauwiller, M. R.; Liu, Y.; Xu, T.; Alivisatos, A. P. Structural Diversity in Binary Superlattices Self-Assembled from Polymer-Grafted Nanocrystals. *Nat Commun* **2015**, *6* (1), 10052. https://doi.org/10.1038/ncomms10052.

(144) Cherniukh, I.; Sekh, T. V.; Rainò, G.; Ashton, O. J.; Burian, M.; Travesset, A.; Athanasiou, M.; Manoli, A.; John, R. A.; Svyrydenko, M.; Morad, V.; Shynkarenko, Y.; Montanarella, F.; Naumenko, D.; Amenitsch, H.; Itskos, G.; Mahrt, R. F.; Stöferle, T.; Erni, R.; Kovalenko, M. V.; Bodnarchuk, M. I. Structural Diversity in Multicomponent Nanocrystal Superlattices Comprising

Lead Halide Perovskite Nanocubes. *ACS Nano* **2022**, *16* (5), 7210–7232. https://doi.org/10.1021/acsnano.1c10702.

(145) Davis, V. A.; Ericson, L. M.; Parra-Vasquez, A. N. G.; Fan, H.; Wang, Y.; Prieto, V.; Longoria, J. A.; Ramesh, S.; Saini, R. K.; Kittrell, C.; Billups, W. E.; Adams, W. W.; Hauge, R. H.; Smalley, R. E.; Pasquali, M. Phase Behavior and Rheology of SWNTs in Superacids. *Macromolecules* **2004**, *37* (1), 154–160. https://doi.org/10.1021/ma0352328.

(146) Brandt, R. E.; Stevanović, V.; Ginley, D. S.; Buonassisi, T. Identifying Defect-Tolerant Semiconductors with High Minority-Carrier Lifetimes: Beyond Hybrid Lead Halide Perovskites. *MRS Commun* **2015**, *5* (2), 265–275. https://doi.org/10.1557/mrc.2015.26.

(147) Baranov, D.; Toso, S.; Imran, M.; Manna, L. Investigation into the Photoluminescence Red Shift in Cesium Lead Bromide Nanocrystal Superlattices. *Journal of Physical Chemistry Letters* **2019**, *10* (3), 655–660. https://doi.org/10.1021/acs.jpclett.9b00178.

(148) Marcato, T.; Krumeich, F.; Shih, C. J. Confinement-Tunable Transition Dipole Moment Orientation in Perovskite Nanoplatelet Solids and Binary Blends. *ACS Nano* **2022**, *16* (11), 18459–18471. https://doi.org/10.1021/acsnano.2C06600.

(149) Jayjock, M.; Logan, P.; Mader, B.; Owens, J.; Eldridge, J.; Costello, M.; Morken, M.; Lieder, P. Modeled Comparisons of Health Risks Posed by Fluorinated Solvents in a Workplace Spill Scenario. *Ann Occup Hyg* **2011**, *55* (2), 202–213. https://doi.org/10.1093/annhyg/meq062.

(150) Han, J.; Kiss, L.; Mei, H.; Remete, A. M.; Ponikvar-Svet, M.; Sedgwick, D. M.; Roman, R.; Fustero, S.; Moriwaki, H.; Soloshonok, V. A. Chemical Aspects of Human and Environmental Overload with Fluorine. *Chem Rev* **2021**, *121* (8), 4678–4742. https://doi.org/10.1021/acs.chemrev.0c01263.

(151) Jana, A.; Meena, A.; Patil, S. A.; Jo, Y.; Cho, S.; Park, Y.; Sree, V. G.; Kim, H.; Im, H.; Taylor, R. A. Self-Assembly of Perovskite Nanocrystals. *Prog Mater Sci* **2022**, *129*, 100975. https://doi.org/10.1016/j.pmatsci.2022.100975.

(152) Cui, J.; Liu, Y.; Deng, Y.; Lin, C.; Fang, Z.; Xiang, C.; Bai, P.; Du, K.; Zuo, X.; Wen, K.; Gong, S.; He, H.; Ye, Z.; Gao, Y.; Tian, H.; Zhao, B.; Wang, J.; Jin, Y. Efficient Light-Emitting Diodes Based on Oriented Perovskite Nanoplatelets. *Sci Adv* **2025**, *7* (41), eabg8458. https://doi.org/10.1126/sciadv.abg8458.

(153) Bernardo-Gil, G.; Esquivel, M.; Ribeiro, A. *Densities and Refractive Indices of Pure Organic Acids as a Function of Temperature*; ***1990***; Vol. 35. https://doi.org/10.1021/je00060a032.